



저작자표시-비영리-변경금지 2.0 대한민국

이용자는 아래의 조건을 따르는 경우에 한하여 자유롭게

- 이 저작물을 복제, 배포, 전송, 전시, 공연 및 방송할 수 있습니다.

다음과 같은 조건을 따라야 합니다:



저작자표시. 귀하는 원저작자를 표시하여야 합니다.



비영리. 귀하는 이 저작물을 영리 목적으로 이용할 수 없습니다.



변경금지. 귀하는 이 저작물을 개작, 변형 또는 가공할 수 없습니다.

- 귀하는, 이 저작물의 재이용이나 배포의 경우, 이 저작물에 적용된 이용허락조건을 명확하게 나타내어야 합니다.
- 저작권자로부터 별도의 허가를 받으면 이러한 조건들은 적용되지 않습니다.

저작권법에 따른 이용자의 권리는 위의 내용에 의하여 영향을 받지 않습니다.

이것은 [이용허락규약\(Legal Code\)](#)을 이해하기 쉽게 요약한 것입니다.

[Disclaimer](#)

공학박사 학위논문

**Development of Plasma Information  
Based Virtual Metrology (PI-VM)  
for Plasma-assisted Processes**

플라즈마 정보 기반의 플라즈마 공정용  
가상 계측 방법론(PI-VM) 개발

2015년 2월

서울대학교 대학원

에너지시스템공학부

박 설 혜

# Development of Plasma Information Based Virtual Metrology (PI-VM) for Plasma-assisted Processes

지도 교수 김 곤 호

이 논문을 공학박사 학위논문으로 제출함  
2014 년 10 월

서울대학교 대학원  
에너지시스템공학부  
박 설 혜

박설혜의 박사 학위논문을 인준함  
2014 년 11 월

위 원 장    황    용    석    (인)

부위원장    김    곤    호    (인)

위    원    한    종    훈    (인)

위    원    원    제    형    (인)

위    원    홍    상    진    (인)

## **Abstract**

# **Development of Plasma Information Based Virtual Metrology (PI-VM) for Plasma-assisted Processes**

Park Seolhye

Department of Energy Systems Engineering  
The Graduate School  
Seoul National University

Plasma-assisted processes applied to semiconducting device- and display-manufacturing processes must be monitored by virtual metrology (VM) to maintain the process results and increase the throughput of the process. VM models that are widely used to predict the process results, such as etch rate and deposition rate, are based on statistical methods that analyse the correlation between sensing variables and performance variables. Principal component analysis (PCA) is a frequently used statistical method for VM modelling. The method identifies sensing variables to give highly correlated information for the prediction of

performance variables and compounds them to the principal components (PCs), which are orthogonal to each other. However, in identified sensing variables obtained from the engineering equipment system (EES), and other sensors, such as for I-V signal, impedance data, and optical raw signals, the information about the reacting plasmas in the process reactor is not efficiently included. The inclusion of a 'good' parameter, which efficiently contains information about the state of the process, is important for ensuring the accuracy of the VM; therefore, the performance of a statistical VM, without consideration of the process plasma information, cannot satisfy industrial requirements of prediction accuracy for ultra-fine processes.

In the plasma-assisted process reactor, three kinds of reactions with different reaction mechanisms occur in the plasma volume, sheath, and substrate surface. In the plasma volume, generations of the reactive radical and ion species by inelastic processes of electron impact collision are dominant. This reaction rate is governed by the thermal equilibrium state of the plasma represented by the electron energy distribution function (EEDF) in the low-density low-temperature process plasmas. At the sheath region, transfer of generated reactive species with their own energy occurs. Ion species are accelerated by the electric field of the sheath and bombarded onto the reacting surface of the substrate. The electric field strength of the sheath is a sensitive function of the electronegativity and the EEDF. On the substrate surface, particles that arrived through the sheath experience sticking or diffusion to find the most stable site, and react with the solid material. This surface reaction is a function of the activation energy of the materials and surface temperature. These three types of reactions in process plasma determine the total process rates; thus, information about these reactions in the plasma should be efficiently included in the applied variables to develop a high-performance virtual metrology for plasma-assisted processes.

The core variables include 'good' information for the VM; therefore, plasma information

(PI) parameters representing the reaction properties in the plasma volume, sheath, and surface are introduced in this dissertation. Shape factor  $b$  of the EEDF is introduced to monitor the variation of the volume reaction rate; ion bombarding energy monitoring parameter  $q$  is introduced to include information about the sheath property in the electronegative plasmas. Information about the passivation reaction on the substrate surface is additionally monitored as the optical signals of the passivating species. These PI parameters are monitored by using the optical emission spectroscopy (OES) sensor. OES is non-invasive to the process plasma and is an already widely used sensor for end point detection (EPD); thus, this sensor has practicality to the application.

The ‘good’ information included variables; accordingly, the developed PI parameters are applied to the VM model according to the reaction mechanisms in the process plasma volume, sheath, and surface. The PI parameters are combined as one overall reaction rate representing the parameter defined as the r-factor; moreover, they are utilized as plasma information based on the VM (PI-VM) model for plasma-assisted processes. PI-VM has shown a noticeably enhanced performance ( $R^2 > 90\%$ ) for both  $C_4F_8$ -oxide etching and a-Si thin-film deposition processes compared to the statistical VM results ( $R^2 \sim 50\%$ ). It therefore satisfies the required accuracy for industrial application.

Cumulated variance analysis of the PCs extracted from the PI parameter-applied PCA validated that the performance of PI-VM was enhanced by the dominant inclusion of the PI parameter. In addition, it was implied that the deviation of the process results was due to the variation of the process plasma properties correlated with the condition of the process device. Therefore, PI-VM has the possibility of a process fault or deviation in the cause analysis because this methodology is based on the reaction mechanisms of the process plasma. This implies that, for the development of fault detection and classification (FDC) or advanced process control (APC) algorithms, information about the reaction mechanisms in the process

plasma should be included in the model, and that the adoption of PI-VM can be an efficient method.

**Keywords:** plasma information based virtual metrology (PI-VM), electron energy distribution function (EEDF), b-factor, q-factor, etch, deposition

**Student ID:** 2008-21137

# Contents

<b>Abstract</b> .....	<b>i</b>
<b>Contents</b> .....	<b>v</b>
<b>List of Tables</b> .....	<b>ix</b>
<b>List of Figures</b> .....	<b>x</b>
<b>Chapter 1. Introduction</b> .....	<b>1</b>
1.1 Properties of the statistical VM generally applied for plasma-assisted processes .....	1
1.2 Requirements on the VM models for plasma-assisted processes.....	5
1.3 Process governing plasma property as a key information for the development of VM .....	7
1.4 Selection of the target process to develop VM for plasma-assisted processes .....	12

## **Chapter 2. Main Plasma Information (PI) Parameter:**

### **b-factor ..... 14**

2.1 Introduction to generalized form of EEDF.....	15
2.2 b-factor monitoring model based on OES signal analysis .....	18
2.3 Sensitivity of b-factor to the variation of the process plasma.....	23
2.3.1 Sensitivity to the metastable argon generation and stepwise ionization rate.....	24
2.3.2 Sensitivity to the gas mixing ratio.....	40

## **Chapter 3. Plasma Information Based VM (PI-VM)**

### **Model for Plasma Etching Process ..... 59**

3.1 Experimental setup and access of sensing data .....	59
3.2 Main and sub PI parameters based on the etching process reaction mechanisms .....	62
3.2.1 Volume reactions and the main PI, b-factor .....	65
3.2.2 Sheath properties and the first sub PI, q-factor .....	67
3.2.3 Surface reactions and the second sub PI, passivation sepeices .....	83
3.3 Construction of VM components based on PI parameters.....	85
3.3.1 Chemical etching term.....	91
3.3.2 Physical etching term.....	94
3.3.3 Surface passivation term.....	96

3.4 Performance of PI-VM model for etch rate prediction.....	97
3.4.1 Organization of $r_{\text{etch}}$ -factor .....	97
3.4.2 Performance of PI-VM by using $r_{\text{etch}}$ -factor .....	98

## **Chapter 4. Expansion of PI-VM Model for Plasma**

### **Enhanced a-Si Deposition Process ..... 100**

4.1 Experimental setup and access of sensing data .....	100
4.2 PI parameters based on the a-Si thin film deposition mechanism.....	101
4.2.1 Volume, sheath, surface reactions and PI parameters, $b$ and $q$ ....	104
4.2.2 Film quality determination mechanism and $q$ -factor .....	112
4.3 Evaluation of PI-VM model to the a-Si PECVD.....	115
4.3.1 Organization of $r_{\text{depo}}$ -factor .....	115
4.3.2 Performance of PI-VM by using $r_{\text{depo}}$ -factor .....	116

## **Chapter 5. Characteristics of PI-VM for Plasma-**

### **assisted Etch-Deposition Processes .....118**

5.1 Characterization of the PI-VM consisting variables .....	118
5.1.1 Classification of the monitoring sensing variables.....	118
5.1.2 Characterization of the PCs.....	120
5.2 Application of the PI-VM for chamber to chamber (C2C) matching problem .....	124

<b>Chapter 6. Conclusions.....</b>	<b>137</b>
<b>Bibliography .....</b>	<b>139</b>
<b>초    록 .....</b>	<b>147</b>

## List of Tables

Table 2.1 Selected second order reaction rate constants (based on Maxwellian EEDF) for electron impact collisions in argon discharges .....	50
Table 2.2 Selected second order reaction rate constants (based on Maxwellian EEDF) for electron impact collisions in oxygen discharges .....	51
Table 2.3 Selected second order reaction rate constants (based on Maxwellian EEDF) for neutral reactions in O <sub>2</sub> /Ar discharges .....	54
Table 2.4. Selected second order reaction rate constants (based on Maxwellian EEDF) for electron impact collisions in helium discharges .....	58
Table 2.5. Selected second order reaction rate constants (based on Maxwellian EEDF) for neutral reactions in O <sub>2</sub> /He discharges .....	58
Table 3.1 The list of monitored EES SVs after the sensitivity test. ....	61
Table 4.1 Error of the a-Si PECVD rate prediction by using the VM methodologies of PI-VM, PCR <sub>0</sub> , and PCR <sub>h,q</sub> . ....	117

## List of Figures

Fig.2.1 Operating region of the thermodynamic equilibrium model in terms of $n_e$ and $T_{e,eff}$ ...	22
Fig.2.2 Schematic of the experimental setup with the OES measurement system to monitor the Ar I and the Ar II lines and the Langmuir probe .....	26
Fig.2.3 Variation of the line emission intensity ratio (Ar I (811.5 nm) to Ar I (750.4 nm)) in a 10-mTorr argon plasma with the applied power .....	28
Fig.2.4 Variation of the EEDF shape factor $b$ in a 10-mTorr argon plasma with the applied power obtained from OES measurements (squares), Langmuir probe measurements (circles) and kinetic calculations (triangles).....	29
Fig.2.5 Measured EEDFs as functions of the applied power in a 10-mTorr argon discharge by using (a) Langmuir probe data and (b) OES data .....	31
Fig.2.6 Plasma parameters estimated using the analyzed EEDFs as functions of the applied power: (a) electron density measured by using a Langmuir probe and (b) effective temperature measured by using a Langmuir probe and the OES data .....	32
Fig.2.7 Variation of the plasma parameters obtained by using OES measurements in a 20-mTorr capacitively-coupled argon plasma with the applied power: (a) EEDF shape factor $b$ (squares) and the effective temperature (circles), and (b) the line emission intensity ratio (Ar I (811.5 nm) to Ar I (750.4 nm)) .....	39
Fig.2.8 Measured EEDFs with variation of oxygen molar fraction in O <sub>2</sub> /Ar plasma using by (a) Langmuir probe data and (b) OES data.....	43
Fig.2.9 Measured EEDF describing parameter with variation of oxygen molar fraction in O <sub>2</sub> /Ar plasma : (a) effective electron temperature, $T_{e,eff}$ (b) shape factor, $b$ .....	44

Fig.2.10 Measured plasma parameters with variation of oxygen molar fraction in O2/Ar plasma : (a) electron density measured by Langmuir probe (b) line emission intensity ratio(Ar I(811.5 nm) to Ar I (750.4 nm)) of OES data .....	47
Fig.2.11 Calculated energy relaxation length of the electrons in terms of the electron energy with variation of oxygen molar fraction in O2/Ar plasma.....	49
Fig.2.12 Normalized reaction rates by the molar fraction of the composing gases at $T_{e,eff} = 5$ eV with variation of oxygen molar fraction in O2/Ar plasma.....	54
Fig.2.13 Normalized reaction rates by the molar fraction of the composing gases at $T_{e,eff} = 5$ eV with variation of oxygen molar fraction in O2/He plasma .....	56
Fig.2.14 Measured EEDF describing parameter with variation of oxygen molar fraction in O2/He plasma : (a) effective electron temperature, $T_{e,eff}$ (b) shape factor, $b$ .....	57
Fig.3.1 The schematics of the TF(Triple-Frequency) – CCP etcher .....	60
Fig.3.2 Schematic of electron impact reactions in c-C4F8 . The thickness of arrows represents the value of reaction rates calculated for an ICP at 6 mTorr, 600 W, 13.56 MHz. ....	66
Fig.3.3 Electron impact cross sections for (a) C4F8 and (b) C2F4. A, B, C, D, E, F, and G represent C2F4+, C3F5+, CF+, CF3+, CF2+, F+, and C2F3+ .....	67
Fig.3.4 (a) 3-dimensional plot of the sheath edge potential in the electronegative plasma as a function of the electronegativity and plasma temperature, (b) side view of the 3-dimensional plot which represents the 2-dimensional plot of the electronegativity vs. sheath edge potential .....	75
Fig.3.5 thermodynamical constraint considered solution of the sheath edge potential as a function of the electronegativity and plasma temperature in 3-dimensional space of $\eta - \alpha - \gamma$ . .....	80
Fig.3.6 Example of the solution of the sheath edge potential in the electronegative plasma at $C/n_e n_n = 0.2$ condition for Allen’s and Seolhye’s in the 3-dimensional space of $\eta - \alpha - \gamma$ . ..	81

Fig.3.7 Cumulated variance fraction with increasing number of principal components consisted by the sensing variables without the consideration of the PI parameters.....	86
Fig.3.8 The variation of etch rates for 50 wafers measured by V-SEM images .....	88
Fig.3.9 The variation of the PCs during the process of 50 wafers : (a) the 1st PC, (b) the 2nd PC, and (c) the 3rd PC. ....	89
Fig.3.10 The comparison of the PCR0 based VM result for the prediction of etch rate without the consideration about the PI parameters and the measured etch rate for 50 wafers. ....	91
Fig.3.11 The comparison of the PCRb based VM result with the consideration of the PI parameter b and the measured etch rate for 50 wafers .....	92
Fig.3.12 The comparison of the PCRb,q based VM result with the consideration of the PI parameters b and q, and the measured etch rate for 50 wafers .....	95
Fig.3.13 Correlation diagram of the measured etch rate and predicted etch rate by the PI-VM for 50 wafers .....	99
Fig.3.14 The comparison of the PI-VM result and the measured etch rate for 50 wafers. ....	99
Fig.4.1 The schematics of the a-Si thin film deposition process including the PECVD process. ....	103
Fig.4.2 The structure of SiH <sub>4</sub> molecule widely used for the PECVD processes .....	105
Fig.4.3 Electron impact collisional ionization cross section of H <sub>2</sub> O, O <sub>2</sub> , Al, SiH <sub>4</sub> and fragments of SiH <sub>4</sub> .....	105
Fig.4.4 Hydrogen terminations of the Si surface; Si(111):H, Si(111):SiH <sub>3</sub> ,Si(100) <sub>2x1</sub> :H, and Si(100) <sub>1x1</sub> :2H.....	107
Fig.4.5 Schematics of the surface diffusion model for a-Si deposition.....	110
Fig.4.6 Schematics of the etching model for a-Si deposition.....	111
Fig.4.7 Schematics of the chemical annealing model for a-Si deposition.....	112
Fig.4.8 The comparison of the PI-VM results and the measured deposition rate for a-Si	

PECVD process .....	117
Fig.5.1 Evaluation of the PCs based on the classification of the sensing variables into the plasma parameters, operating parameters, and device parameters for C4F8-oxide etch process analyzed in this thesis.....	122
Fig.5.2 Evaluation of the PCs based on the classification of the sensing variables into the plasma parameters, operating parameters, and device parameters for a-Si PECVD process analyzed in this thesis.....	123
Fig.5.3 RGA intensity ratio of the residual (a) nitrogen and (b) oxygen gas, normalized by the argon intensity, present in the two etchers measured during the argon purging-exhaustion step. The chromium etching process analyzed in this experiment was performed under repeated 100 sec exhaustion and 1 min etching cycles .....	128
Fig.5.4 b-factors of the two etchers during the etching process, measured using the OES signals. Twenty-one wafers were etched in each etcher during the 3-day test period (7 wafers/day). Note that the error bars of the b-factors indicate the standard deviations from the one-day b-factors during the etching process, determined from 7 wafers collected from each of the etchers. ....	130
Fig.5.5 EEDFs of the two etchers during the etching process, obtained from $(b, T_{e,eff})$ , measured by using the OES signals. The values of $(b, T_{e,eff})$ from the EEDFs plotted here were averaged over the values obtained during the 3 days from each etcher .....	131
Fig.5.6 RGA intensity ratio of the dissociated nitrogen, oxygen radicals, CrO <sub>2</sub> Cl <sub>2</sub> species, and CrCl <sub>2</sub> species, normalized by the argon intensity in the two etchers, as measured during the etching process. The plotted intensity ratios were obtained from the average of the signals obtained over 3 days from each etcher .....	132

# Chapter 1 . Introduction

## 1.1 Properties of the statistical VM generally applied for plasma-assisted processes

The necessity of a high-value process strategy for the semiconductor- and display-manufacturing industry, which requires ultra-fine process technology, is ever increasing to achieve an increase of device production throughput. The driving principle of the growing throughput requirements of the semiconductor industry has been Moore's law, which was proposed by Gordon Moore in 1965 [1]. This law states that the number of transistors and resistors on an IC chip doubles every 19 months. This law has been realized by technology innovations aimed at increasing the number of components on a minimized chip [1, 2].

Technology innovation has been achieved by the innovation of plasma-assisted process devices. The density and temperature of process plasmas have increased to raise reaction rates in the process device by the application of high frequency and high power in most plasma-aided etching and deposition processes [3]. Heating of the electrons in plasma with high efficiency leads to an increase of plasma reaction rates; thus, the application of very high frequency (VHF) power has become an unavoidable choice for process devices. VHF power has increased the density of process plasma, as expected; nevertheless, this has caused unexpected problems, such as non-uniformity of process results on the wafer by the standing wave effect [4]. To solve this spatial non-uniformity problem, the process device has evolved into an increasingly complicated design with multiple-frequency power-applied electrodes. This complicated design of the process device has resulted in numerous operating conditions;

moreover, the correlations between the operating parameters and process results are nonlinear. Simple regulation of the operating conditions to control the results of the process has become difficult; thus, efficient use of the developed device is very important for achieving ultra-fine-technology-based processes.

On account of these properties, to control process results in complicated plasma-assisted process devices, an automated control system, such as fault detection and classification (FDC) and advanced process control (APC) logics, is required. Application of these logics can be applied to maximize the performance of existing process devices by advanced efficient operation; furthermore, this application is essential for maintaining high manufacturing yields. To obtain significantly enhanced results of the process by application of the control logics, fast and in-situ detection and control of the process are required rather than batch-to-batch scale control [5, 6]. This implies that, to develop useful in-situ process control algorithms, process-result-monitored data, in the performance variable form, should be provided as information into the logic. Most plasma-assisted processes are performed in a vacuum chamber; thus, direct measurement of the process results is very difficult. It requires the development of a virtual metrology (VM) model, which directs the process control. For the VM, various kinds of sensors are attached to the plasma-assisted process device; the sensor values are periodically read. The real values obtained from each sensor collectively constitute a time series. The VM algorithm is additionally given in the time series of results [5]. The VM was developed from classical chemical processes to predict process results based on the statistical analysis of monitored sensor data. According to Cheng *et al.*, VM is a method for estimating the manufacturing quality of a process tool based on data sensed from the process tool and without physical metrology operations [7]. Owing to the start of the VM concept from this basis, development of the VM for plasma-assisted processes was likewise initiated from statistical approaches.

Development of the statistically established VM began from correlation analysis of the variables with process results. To this end, principal component analysis (PCA) has been widely used to find the variables containing the most information with statistical efficiency. PCA is a well-known automatic dimension-reduction method with a simple algorithm. The principal components (PCs) generated by the combination of the sensing variables are independent of other PCs. This makes property analysis of the PCs possible by analysing the sensing variables that comprise each PC. After regression, using the analysed PCs to predict the process results, normalization and scaling to predict actual process results are performed as a last course of the statistical VM [8, 9]. However, this statistical-method-based VM has shown unsatisfactory prediction accuracy when applied to numerous cases of plasma-aided processes [10].

According to Loh *et al.*, the variable selection method determines the accuracy of the process monitoring algorithm. To improve the algorithm's accuracy, the sensor variables that are most likely to give 'good' information are selected by allowing it to use a smaller number of variables [5]. This implies that the generally used PCA-based statistical VM model for plasma-assisted processes has insufficiently included the 'good' information-representing variables. Actually, variables sensed from sensors attached to the plasma-assisted process device are log data of applied power, power matching conditions, pressure, mass flow controller (MFC) conditions, gas temperature, coolant temperature, surface temperature, residual gas analyser (RGA) signals, I-V signals, impedances, OES raw intensities, etc. The parameters comprising these sensing variables, which represent their own physical parameters, are nonlinearly coupled with each other. The variables relating to the plasma-assisted process are classified into three groups: manipulated variables (MVs), state variables (SVs), and performance variables (PVs). Monitored SVs as variables sensed by the sensors have difficulty directly representing the process plasma properties; moreover, the correlations

among the MVs, SVs, and PVs are additionally nonlinear and complicated. This means that it is difficult to satisfy the requirement of developing a highly accurate monitoring algorithm that secures the ‘good’ information-representing parameter for plasma-assisted processes by using the raw SVs.

Therefore, the provision that processed SVs are representative of the process state as ‘good’ information-including parameters is an important objective in the development of monitoring algorithms such as VMs. Nonlinear statistical methods have been applied to the process of SVs as one approach to monitoring algorithm development. Nonlinear PCA and neural networks are representative methods that have been applied to VM development; they have been proven as successful techniques for monitoring multi-step chemical processes. Performance of these nonlinear statistical techniques is determined by the selection of a computation method. Accuracy of monitoring algorithms based on nonlinear PCA depends on the selection of the kernel function, while that of neural networks depends on the learning logic of the model [11-13]. However, in a study by White *et al.*, the nonlinear PCA-based VM could not achieve high repeatability for the validation set, even though it showed good performance for the training set [4]. Nonlinear statistical methods compute the prediction algorithms through frequent self-feedback of the calculation and reuse of the variables during the computation. These procedures decrease the speed of the computation, and the repeatability in the validation set likewise decreases [6]. As a result, generally used nonlinear statistical techniques have difficulty satisfying the industrial requirements for VM performances for plasma-assisted processes in terms of accuracy and computation time [5].

Statistical methods require at least ten sets of data records per one sensing variable to obtain statistically guaranteed accuracy [14]. Plasma-assisted processes use more sensors than classical processes because of their complicated operating conditions; moreover, they require a minimum of hundreds or thousands of data sets to obtain the statistically guaranteed accuracy

of the statistical VM model. Therefore, acquisition of a sufficient number of data sets that satisfies the statistical requirement necessitates a high-performance computer system. Merging and processing of this huge amount of data for the VM are possible by the construction of enormous storage and computer memory. This property of the statistical models for plasma-assisted processes makes it difficult to adopt in-situ monitoring to the VM system.

## **1.2 Requirements on the VM models for plasma-assisted processes**

Owing to the specificity of plasma-assisted processes, the simple adoption of widely used statistical methodologies makes it difficult to compute the algorithm using the sensed and manipulated variables to predict performance variables. In addition, the obtainment and utilization of ‘good’ information-representing parameters in the VM model are likewise challenging. To develop high-performance VM models, solutions to these limitations of the simple statistical methods are needed. Efficient containment of the ‘good’ information-representing parameters—that is, the parameters representing the process plasma state—may comprise one solution. Furthermore, according to the represented properties of the selected parameters in the process reaction mechanism, a valid variable combination rule can be suggested, which may constitute another solution.

For development of a VM that satisfies these requirements for plasma-assisted processes, a method of efficiently containing ‘good’ information about the process plasma state is important. To apply to the VM model parameters that can efficiently mediate between state variables and performance variables, the specificity of a plasma-assisted process mechanism should be considered. Unlike the homogeneous single-phase medium chemical reactor, the

volume of the plasma reactor can be classified into three regions according to the physical properties of the reactions. Liebermann *et al.* discussed the importance of the reactions in the plasma volume, sheath, and target surface in terms of the progress of the process reactions, such as etching, deposition, sputtering, and ashing [15].

For low-pressure low-temperature process plasmas, the bulk volume of the plasma occupies almost all of the reactor volume. Therefore, most of the reactions contributing to the progress of the process occur in the volume of the plasma. Reactive radical and ion species required for chemical reactions on the substrate surface are generated in this volume. The amount of the generated radical and ion species dominates the overall reaction rates; therefore, information about the plasma volume reaction governing the physical parameters should be included in the VM model.

Generated radicals are transferred onto the surface from the plasma volume by diffusion. Ions are accelerated by the electric field formed in the sheath region and transferred onto the surface with energies determined by the Bohm condition of that plasma. The sheath region is the passage of the material and energy transferred from the plasma volume to the reacting surface. This region has a smaller volume compared to the bulk plasma volume; nevertheless, it governs the energy of transferred ions. In addition, the information about the sheath property becomes an important parameter for the VM model development.

Ions that arrived onto the substrate surface with accelerated bombarding energy activate the reacting surface or sputter the particles, which leads to the physical reaction on the target surface. Particles that arrived onto the surface are diffused to the vacant or weakly bonded site greater than their potential energy, thereby causing a surface reaction. This is a function of the surface temperature and Gibbs free energy of the reaction. For unstable or reactive species, surface sticking is an additionally important reaction path on the substrate. These surface reactions are the final step of the process reaction that occurs in the 2D interface region

between the plasma and substrate. Although the overall process reaction rate is governed by the generation rate of the reacting species in the volume and by the acceleration in the sheath region, the final reaction rate is determined by the surface reaction. The information about the surface reaction is additionally required for developing the VM model.

These overall reactions are strongly correlated with each other and governed by the properties of the process plasma. Therefore, to develop the VM for plasma-assisted processes, the process plasma information, including parameters representing the reaction properties in the plasma based on the volume-sheath-surface reaction mechanism, are required.

To attain this concept of the VM for plasma-assisted processes, an introduction of new parameters that are applicable as powerful variables is required. These parameters should include the information about the reactions in the plasma volume, sheath, and surface; moreover, they should have a high sensitivity to the even smallest variations of the process condition. Development of these new parameters can be a key to VM performance for the plasma-assisted process.

### **1.3 Process governing plasma property as a key information for the development of VM**

As described above, the plasma-assisted process is performed by chemical–physical reactions in the plasma volume, particle and energy transfer through the plasma sheath, and diffusion or sticking reactions on the substrate surface. To include information about these three types of reactions in the process plasma into the VM model, the physical properties correlating with the reaction rates in the three regions are considered.

In general, and in the case of the plasmas, most of the reaction rates are governed by the thermal property of the reacting materials. The thermal property is basically represented by the temperature of that material. However, the thermal property of the fluids, such as liquid, gas, and plasma, are not describable by only one parameter. Based on a kinetic approach, which describes the phenomena in terms of the distribution function of the composing particles and their physical properties, the thermal property of the fluids is described in terms of the thermal equilibrium state. The quantities averaged by the distribution function in the kinetic approach agree with well-known physical quantities such as mass, flux, and temperature. However, to analyse the detailed phenomena and detect even slight variations of the subject, the kinetic approach is better than the averaged parameter-based description. An introduction of the distribution function of the kinetic approach can describe more detailed phenomena not otherwise explained in the simple averaged approaches with the same basic governing equations and physical principals [16]. Consequently, the reaction rates in the process plasma should be handled by using the kinetic approach with a description of the thermal equilibrium state of the plasma. Moreover, by introducing the thermal equilibrium state representing the physical parameter of the plasma, the detailed variation of the process condition in the plasma reactor can be monitored and included in the VM model as the monitored information.

To include the information about the thermal equilibrium state of the process plasma in terms of kinetics, the electron energy distribution function (EEDF) of the plasma is introduced rather than the averaged plasma temperature [17]. Most of the plasma processes are performed in vacuum conditions, and the plasma density ( $\sim 10^{12} - 10^{18} \text{ m}^{-3}$ ) or temperature ( $< \sim 10 \text{ eV}$ ) is very low compared to well-known fusion plasmas ( $\sim 10^{20} \text{ m}^{-3}$ ,  $\sim 10 - 1000 \text{ keV}$ ). In low-density low-temperature plasmas, reactions by inelastic collisions are predominantly caused by the electron impact collision to the heavy particles. Almost all of the heavy particles, such as neutral gas particles and ions, are in ground states because of the low temperature of the

plasma. Furthermore, the energy required for the reactions is transferred by the fast electrons heated by the applied power to the plasma. Therefore, the basis of the reactions in the plasma by the collisional reaction is the energy of the electrons, and the EEDF can be applied to the VM development as core information about the process plasma state [18]. The reaction rate in the plasma is defined as

$$R = \sum_{i,j=\text{species}} n_i n_j \langle \sigma v \rangle_{ij} \quad (1.1)$$

where  $R$  is the reaction rate,  $n_{ij}$  is the density of particle  $i$  and species  $j$ ,  $\sigma$  is the collision cross section of particles  $i$  and  $j$ , and  $v$  is the relative velocity between  $i$  and  $j$ . The brackets on  $\sigma v$  denote the averaged value of their distribution function. With consideration of velocity distribution, Eq. 1.1 can be rewritten as

$$\left. \frac{\partial n(\vec{r}, t)}{\partial t} \right|_{cij} = \sum_{i,j} \int f(\vec{v}, \vec{r}, t) |\vec{v}| \sigma_{ij}(v) n_j n_i d^3v \quad (1.2)$$

where  $r$  is the position of the particle,  $t$  is time, and  $f$  is the velocity distribution function at the six-phase space of velocity and position. For the low-pressure low-temperature process plasma, the relative velocity between inelastically colliding species  $i$  and  $j$  is comparable to the velocity of the electrons. Light electrons are considerably faster than heavy particles; moreover, the effective velocity distribution function can be considered as the electron energy distribution function at that position and moment. This emphasizes the importance of the information about the energy distribution of electrons; thus, the EEDF can become a key aspect of the kinetic approach to describing the overall reaction rates in the process plasma.

The inelastic collisional processes, such as excitation, ionization, and dissociation, require the electron energies above the threshold energy; almost all inelastic collisions require threshold energies near or above 10 eV. This inelastic collision reaction rate can be expressed as

$$R = n_0 n_e \int_{E_{thr}}^{\infty} \sigma(\varepsilon) \sqrt{\varepsilon/2m_e} f_e(\varepsilon) d\varepsilon \quad (1.3)$$

where  $n_0$  is the gas density on the ground state,  $n_e$  is the electron density,  $m_e$  is the electron mass,  $f_e$  is the EEDF, and  $\varepsilon$  is the energy of the electron. When the high energy electrons with energies above the reaction threshold are abundant, the reaction rate in the plasma volume is high. On the other hand, the electrons with high energy above ~10 eV lose their energies by the inelastic collisions; these are counted as low energy electrons. This causes the variation of the EEDF shape, especially the high energy tail of the distribution. According to Godyak *et al.*, the shape of the EEDF tail above the threshold energy of the inelastic process is very sensitive to the inelastic collision property in the plasmas [19-21]. This implies that the EEDF determines the reaction rates in the plasma volume and is additionally influenced by the inelastic collisional reactions. Therefore, monitoring of the EEDF provides information about the reaction rates and the properties of the dominant reactions in the plasma. In particular, beneath the 10 eV bulk region of the EEDF is 99.9% of the total distribution for generally used process plasmas (the average temperature of the plasma being ~ 3-5 eV), whereas the fraction of the tail is only  $10^{-3}$  of the distribution. This means that even a small variation of the distribution shape can significantly change the tail of the distribution, and reaction rates by the electron impact inelastic collision can be noticeably changed. Volume reaction rates, which are the dominant reactions in the process reactions, are determined by the tail shape of the

EEDF. The fraction of the high energy tail of the total EEDF determines the generation rate of the reactive radical and ion species. This property of the volume reactions in the process plasma enables a key approach; that is, the monitoring of the EEDF tail can be an efficient method in the monitoring of process plasma information.

The sheath property of the plasma, which governs the bombarding energy of ions accelerated onto the substrate surface, is additionally influenced by EEDF and the electronegativity of the process plasma volume. The electronegativity is defined as the ratio of negative ion density to positive ion density; it is an index of the abundance of negative ion species in the plasma. This quantity is strongly correlated with the thermal equilibrium state of the process plasma because the generation procedures of the negative ions are also inelastic collisions of the electrons, such as attachments, dissociative attachments, and recombinations. The sheath edge is defined as the break of quasi-neutrality of the plasma volume; thus, the existence of negative ions and the deviated thermal equilibrium state by their generation differentiate the property of the sheath in the electronegative plasma from the general electropositive plasmas [22-24]. Because most of the process plasmas that aid the etching and deposition processes form the electronegative plasmas, the electronegativity and correlated thermal equilibrium property of the plasma must be considered for monitoring the sheath property of the process plasma [25]. Therefore, the EEDF, which represents the thermal equilibrium state of the plasma, additionally becomes important information for sheath property monitoring for the VM development.

The transferred energy and flux of radicals and ions onto the substrate are determined by the reactions in the plasma volume and sheath region. Therefore, the reaction on the substrate surface depends on the EEDF of the process plasma. This implies that the information about the EEDF, especially its shape, can be applied to the mediating parameter, which is appropriate for sensitively describing the correlation between the volume, sheath, and surface

reactions in the process plasma. As a result, the shape of the EEDF is selected as an important parameter for monitoring the information about the reactions in the process plasma. This plasma information (PI) parameter is applied to the development of the VM model for the plasma-assisted process.

The purpose of developing a PI-based VM is to monitor the deviation of process results within the nm-scale order; these results are not easily detected by the existing statistical-method-based VM. Because the allowable prediction error of the ultra-fine processes are very small, less than 0.4 % in the industry [2,3], even small variations in the process reaction governing the plasma property must be detected and included in the VM model as key information. Accordingly, the shape of the EEDF is strategically selected as the core plasma information in this dissertation.

## **1.4 Selection of the target process to develop VM for plasma-assisted processes**

To develop the framework of the VM for plasma-assisted processes, the monitoring of plasma information, which represents the reaction mechanisms in the plasma reactor, is required. In addition, the shape of the EEDF is selected as the key PI parameter in Section 1.3. As shown in Eq. 1.3 of the previous section, the collision cross section and threshold energy of the reaction are likewise essential information to the EEDF in the analysis of the reaction rates in the plasma. The EEDF represents the state of the process plasma; the change of this parameter simultaneously occurs with the variation of the sensing variables. The cross section and threshold energy are determined with respect to the kinds of discharge gases used in the

target process and its operating recipe. Therefore, the estimation of the reaction rates can be achieved by substituting the information about the EEDF in Eq. 1.3 when the target process and its recipe are known.

However, large numbers of the material property data for the process gases, such as cross sections of enormous numbers of the reactions, the threshold energy of the reactions, and collision rate constants among heavy particle species, are unknown. Information about only a small number of widely used process gases is provided and shared in database form. Therefore, to establish a framework of the plasma-assisted process VM, well-known widely used process gas-adopted processes were selected as target processes in this dissertation.

A widely used process gas for etching and cleaning of the deposition processing chambers is fluorocarbon. Therefore, the material property data of fluorocarbon, especially that of  $C_4F_8$ , is relatively abundant.  $C_4F_8$  is generally applied to the etching process of silicon oxide and silicon nitride [26-27]. This  $C_4F_8$  plasma-aided etching process is the base step of various semiconducting device and display manufacturing processes. Therefore, the VM model for the  $C_4F_8$  plasma-applied etching process can become a derivational technology for many plasma-aided etching processes. Moreover,  $C_4F_8$  plasma-aided etching is a high-end technology performed with the high aspect ratio contact (HARC) etching process [28]. Because this etching gas additionally acts as a source of polymer deposition, the  $C_4F_8$  plasma-aided HARC etching process includes various issues of current plasma-assisted processes, such as pattern profile and loading effect. [2].

According to these properties of the  $C_4F_8$  plasma-aided etching process, the target process for VM development is selected as  $C_4F_8$ -oxide etching. Based on the suggested strategies of plasma information parameter application, the PI-based VM model for  $C_4F_8$ -oxide etching is established and extended to the framework of the plasma-assisted process VM.

## Chapter 2 . Main Plasma Information (PI)

### Parameter: b-factor

The reaction rates of the gas molecules or atoms for the generation of reactive radical and ions in the plasma are governed by the inelastic collision cross sections of ionization, excitation, dissociation, etc. and the EEDF of the processing plasma. Analysis of information about these reaction rates in the process plasma is very important to the prediction of the process results. Here the EEDF is assumed as Maxwellian distribution in most of the reaction rate analyzing cases [18]. This ideal condition of the EEDF is often not adopted in the practical plasmas as Godyak reported that a non-Maxwellian EEDF could be observed with the variation of the heating characters in 100 mTorr CCP (Capacitively Coupled Plasma source) and 1 – 10 mTorr ICP (Inductively Coupled Plasma source) argon discharges [29-32]. Boffard *et al.* suggested formation of the non-Maxwellian (shape factor of EEDF  $x=1.2 \pm 0.2$  while  $x=1.0$  represents to Maxwellian distribution) EEDF in argon ICP sources [33]. Here ICP and CCP are frequently used plasma sources to the etching and deposition processes. Dias *et al.* reported that the analysis of surface wave in argon discharge plasma in terms of the plasma potential is more suitable to apply the non-Maxwellian EEDF rather than use of Maxwellian EEDF [34].

Gudmundsson and Haas suggested that the tailoring of the EEDF tail can be achieved by the pressure control in the ICP discharge and the bias voltage in the filament discharge [35-36]. Increase of the pressure causes the depletion of EEDF tail from Maxwellian, and the emission of high energy thermal electrons from the filament generates tail developed distribution. They suggest that the non-Maxwellian EEDF is quite common in the low-

temperature and low-pressure plasma. It intrigues us to investigate how much the additional collision processes induce the divergence of EEDF from Maxwellian, and implies that the degree of depletion from the Maxwellian EEDF can be used as the PI parameter.

According to this, for the investigation of tailoring of EEDF in process plasma, the shape factor of distribution function is introduced. The shape factor can be analyzed from non-invasive sensor data, the optical emission spectra (OES) diagnostics. The analyzed EEDF shape factors from OES measurement with introduced analysis model were evaluated the suitability for the application of PI parameter.

Sensing variables applied to the previous state of statistical VM models were raw OES signals and EES (Equipment Engineering System) data, in general. These variables were acquired data from the in-built sensors, and these raw signals included the coupled and superposed information about the reactions in the process plasma, thus it was difficult to give good information to the VM models. Suggested PI parameter, the shape factor of EEDF achieved by the processing of OES data to represent the thermal equilibrium state of the process plasma, was selected as a main PI parameter to enhance the performance of VM because of the dominance of the volume reactions compare to the overall reactions in the plasma.

## **2.1 Introduction to generalized form of EEDF**

In generally EEDFs of the plasma could be classified as Maxwellian, bi-Maxwellian, and Druyvesteyn types according to the tailoring of the distribution tail and they are often observed in the analysis of the EEDF shape carried out in the low temperature plasmas [35]. The bi-

Maxwellian EEDF is assumed to the coexistence of two temperature electrons in plasma which represent the low and high temperatures and have a concave shape in the logarithm of EEPF (electron energy probability function). The distribution with the curtailed high energy tail of EEDF is Druyvesteyn-like distribution which has a convex logarithm of EEPF, representing fewer high-energy electrons exist in EEDF compared to Maxwellian. All of these cases can be described by using the generalized form of the EEDF with the assumption of the isotropic velocity space [17, 35],

$$f(\varepsilon) = c_1 \varepsilon^{1/2} \exp(-c_2 \varepsilon^b) \quad (2.1)$$

where  $\varepsilon$  is the electron energy,  $b$  is the shape factor of the EEDF, and the coefficients  $c_1$  and  $c_2$  are determined by the normalization of the EEDF and the definition of the average temperature, respectively. The integration of Eq. 2.1 over the energy equals to one as

$$c_1 \int_0^{\infty} \varepsilon^{1/2} \exp(-c_2 \varepsilon^b) d\varepsilon = 1 \quad (2.2)$$

Then we can obtain the average energy of a particle which is known as  $kT/2$  per translational degree of freedom, so the mean energy of the electrons obtains from

$$\langle \varepsilon \rangle = \frac{3}{2} kT_{eff} = c_1 \int_0^{\infty} \varepsilon^{3/2} \exp(-c_2 \varepsilon^b) d\varepsilon \quad (2.3)$$

where  $T_{eff}$  is the effective electron temperature.  $T_{eff}$  is the averaged electron temperature for the arbitral shape of the EEDF while  $T_e$ , electron temperature is averaged by Maxwellian

EEDF, in general. With the definition of the gamma function  $\Gamma(\xi)$ ,

$$\Gamma(\xi) = \int_0^{\infty} t^{\xi-1} \exp(-t) dt \quad \xi > 0 \quad (2.4)$$

the value  $c_1$  and  $c_2$  are described as functions of  $b$

$$c_1 = \frac{b}{\langle \varepsilon \rangle^{3/2}} \frac{[\Gamma(5/2b)]^{3/2}}{[\Gamma(3/2b)]^{5/2}} \quad (2.5)$$

and

$$c_2 = \frac{1}{\langle \varepsilon \rangle^b} \left[ \frac{\Gamma(5/2b)}{\Gamma(3/2b)} \right]^b \quad (2.6)$$

where the shape factor  $b$  of EEDF is sensitive to the property of the EEDF tail part [35]. For a given  $T_{eff}$ , the increase of  $b$  implies the depletion of EEDF tail which corresponds to the transition from a tail-developed Maxwellian distribution ( $b=1$ ) to tail-curtailed Druyvesteyn distribution ( $b=2$ ). EEPF  $g(\varepsilon)$  is expressed as

$$g(\varepsilon) = \varepsilon^{-1/2} f(\varepsilon) = c_1 \exp(-c_2 \varepsilon^b) \quad (2.7)$$

using the parameters defined from the definition of the EEDF.

The expression of the generalized EEDF as defined in Eq. 2.1 can be described in terms of the effective electron temperature and the shape factor of the distribution, so the measure of the

EEDF is performed by the measurement of those two parameters. To classify the type of the EEDF from the curvature observation, EEPF graphs are drawn in log scale using those two parameters. Introduced generalized form of EEDF can describe various types of the non-Maxwellian plasmas sensitively to the variation of distribution tail. As a result,  $b$ -factor in Eq. 2.1 is adopted as a PI parameter which represents the information about the EEDF.

## 2.2 $b$ -factor monitoring model based on OES signal analysis

Corona equilibrium (CE) model is widely adopted in the analysis of the weakly ionized plasma property using the light emission intensity. CE model has the assumption as the most of inelastic processes are occurred by the electron impact collisions and the neutral particles are in the ground state [37]. In addition, the light emission intensity is due to the spontaneous decay process only and it is described as

$$I_{pk} = n_1 n_0 \int_{E_{thr}}^{\infty} \sigma(\varepsilon) (2\varepsilon/m_e)^{1/2} f(\varepsilon) d\varepsilon \quad (2.8)$$

where  $n_1$  is the heavy particle density of ground states,  $n_0$  is the electron density,  $\sigma(\varepsilon)$  is the collisional excitation cross section,  $m_e$  is the mass of the electron, and  $E_{thr}$  is the threshold energy of emissive excitation [37]. The integral product of  $\sigma(\varepsilon)(2\varepsilon/m_e)^{1/2}$  and the EEDF  $f(\varepsilon)$  at the energy above the threshold level determines the light emission intensity. For the convenience of calculation to obtain the EEDF, a new function  $h(\varepsilon)$  is introduced as

$$h(\varepsilon) = \int_0^\varepsilon f(\varepsilon')(2\varepsilon'/m_e)^{1/2} d\varepsilon' \quad (2.9)$$

Using the definition of  $h(\varepsilon)$ , the integration term of Eq. 2.8 is arranged as

$$\begin{aligned} \frac{I}{n_1 n_0} &= \int_{E_{thr}}^\infty \sigma(\varepsilon) h'(\varepsilon) d\varepsilon \\ &= \sigma(\varepsilon) h(\varepsilon) \Big|_{E_{thr}}^\infty - \int_{E_{thr}}^\infty \sigma'(\varepsilon) h(\varepsilon) d\varepsilon \end{aligned} \quad (2.10)$$

where the prime symbol on the functions  $h(\varepsilon)$  and  $\sigma(\varepsilon)$  means the differentiated function with respect to the energy,  $\varepsilon$ . With the definition of the mean energy in Eq. 2.3, Eq. 2.10 becomes

$$\begin{aligned} &\int_{E_{thr}}^\infty \sigma(\varepsilon) h'(\varepsilon) d\varepsilon \\ &= -\sigma(E_{thr}) \left( \frac{2\langle \varepsilon \rangle}{m_e} \right)^{1/2} + \sigma(E_{thr}) \int_{E_{thr}}^\infty f(\varepsilon) (2\varepsilon/m_e)^{1/2} d\varepsilon - \int_{E_{thr}}^\infty \sigma'(\varepsilon) h(\varepsilon) d\varepsilon \end{aligned} \quad (2.11)$$

where  $\sigma(E_{thr})$  is known value for the given gas condition and  $\langle \varepsilon \rangle$  is expressed as the Eq. 2.3. The first term on the right hand side of Eq. 2.11 is only a function of  $\langle \varepsilon \rangle$  and the second term is a function of  $\langle \varepsilon \rangle$  and  $b$ , because the energy,  $\varepsilon$  is calculated as a number by definite integral. To calculate the third term, the differential of the cross section should be given in the form as a function of  $\varepsilon$ . Here the BEB (Binary Encounter Bethe) cross section model is adopted to obtain the slope of the cross sections by direct differentiation [38-41]. Direct

substitution of various cross section data into the Eq. 2.8 is also possible, but the use of BEB cross section model provides the convenience of calculation in the equation Eq. 2.11. The third term has negative quantity because the slope of the excitation cross section,  $\sigma'(\varepsilon)$  decreases at the high energy regime. For  $0 < b \leq 2$ , the absolute value of the third term has at least  $10^4$  times larger quantity than the 1st and 2nd terms, except for the conditions in which  $T_{eff}$  is too high (e.g.,  $T_{eff} > 20$  eV). Therefore, the first and second terms of the right hand side of Eq. 2.11 are negligible and the third term can be applicable to obtain the EEDF for the low-pressure and low-temperature process plasmas.

The light emission intensity is a product of Eq. 2.11, the densities of neutral atom on the ground state ( $n_1$ ), and that of the electron ( $n_0$ ) in this dissertation. Here  $n_1$  and  $n_0$  are common terms defined by pressure and plasma density thus the ratio of selected two lines which have different threshold energies can be written as in the Eq. 2.12. This equation represents the light emission intensity ratio of the two wavelengths emitted via spontaneous decay from state  $i$  to  $j$  and  $k$  to  $l$  which denoted as  $I_{ij}$  and  $I_{kl}$ , respectively.

$$\frac{I_{ij}}{I_{kl}} \simeq \frac{n_1 n_e \int_{E_{thr,i}}^{\infty} \sigma_{1 \rightarrow i}'(\varepsilon) h(\varepsilon) d\varepsilon}{n_1 n_e \int_{E_{thr,k}}^{\infty} \sigma_{1 \rightarrow k}'(\varepsilon) h(\varepsilon) d\varepsilon} \quad (2.12)$$

where  $E_{thr,i}$  and  $E_{thr,k}$  are the excitation threshold energy of states  $i$  and  $k$ , and  $E_{thr,i} \neq E_{thr,k}$ . The subscript  $1 \rightarrow k$  denotes excitation from the ground state to the  $k$  state. This line intensity ratio is a function of the shape factor  $b$ ,

$$\frac{I_{ij}}{I_{kl}} \simeq \frac{\int_{E_{thr,i}}^{\infty} \sigma_{1 \rightarrow i}'(\varepsilon) \left( \int_0^{\varepsilon} c_1 \varepsilon'^{1/2} \exp(-c_2 \varepsilon'^x) d\varepsilon' \right) d\varepsilon}{\int_{E_{thr,k}}^{\infty} \sigma_{1 \rightarrow k}'(\varepsilon) \left( \int_0^{\varepsilon} c_1 \varepsilon'^{1/2} \exp(-c_2 \varepsilon'^x) d\varepsilon' \right) d\varepsilon} \quad (2.13)$$

thus the solution of  $b$  can be obtained through the computational iteration with Eq. 2.3 for the measured OES results, because  $\sigma'(\varepsilon)$  is a given function and  $I_{ij} / I_{kl}$  are obtained from the measured values. Remind that the calculated value of  $b$  denotes the shape of the EEDF, and the EEDF is measured by using the OES as a solution of Eq. 2.13. The shape factor has dependency on the selection of the cross section model, but the change of thermal equilibrium states in the plasma is observable for any cross section adopted calculations [42].

In this dissertation, emission lines of the argon plasma are selected for the monitoring of EEDF. Because argon is an inert gas, chemical reaction effect with the other process gases can be ignored and the only information about the thermal equilibrium property is included in the light emission intensities. And argon is applied to the various etching or deposition processes as dilute gas, ignitor, carrier gas, etc., thus argon line analysis model has high applicability to the PI monitoring of the process plasma. In plasmas to which the CE model is applicable, especially the excitation of ground-state argon atoms requires inelastic collisions with high-energy electrons at energies above 13 eV because the excitation threshold energy levels (2p states) of neutral argon are located near 13 eV. Figure 2.1 shows the operating regions of the thermodynamic equilibrium models for argon plasma in terms of  $n_e$  and  $T_{eff}$  for local thermodynamic equilibrium (LTE), partial thermodynamic equilibrium (pLTE), CRE, and CE.

Boffard *et al.* [33] measured  $b$  as 1.2 in an argon ICP by using the CRE-based OES signal analysis model with many of the argon emission lines. CRE should consider the effects of transitions from metastable states and resonance levels, as well as radiation trapping and cascade effects, which are negligible in plasmas to which the CE model is applicable; thus,

many argon lines were used to measure the EEDF [33, 43]. Most argon neutral emission lines have similar threshold energies near  $\sim 13$  eV, and the energy gaps between those states are less than 0.5 eV, so this method requires highly-resolved OES data for the analysis of EEDF. In addition to the use of many line intensities, emission rate equations and cross-section information for each channel are needed. Then, the solutions, as an infinite number of ordered  $(b, T_{eff})$  pairs, are obtained, and the least-squares method is used to determine one pair. Thus, this method seems to place too much emphasis on a specific energy when fitting the shape of the EEDF. Moreover, the involvement of many uncertain cross-section data causes propagation of the error. In the sense of application, this method should be simplified and modified to adopt it to the plasmas under conditions in which the CE model is applicable.

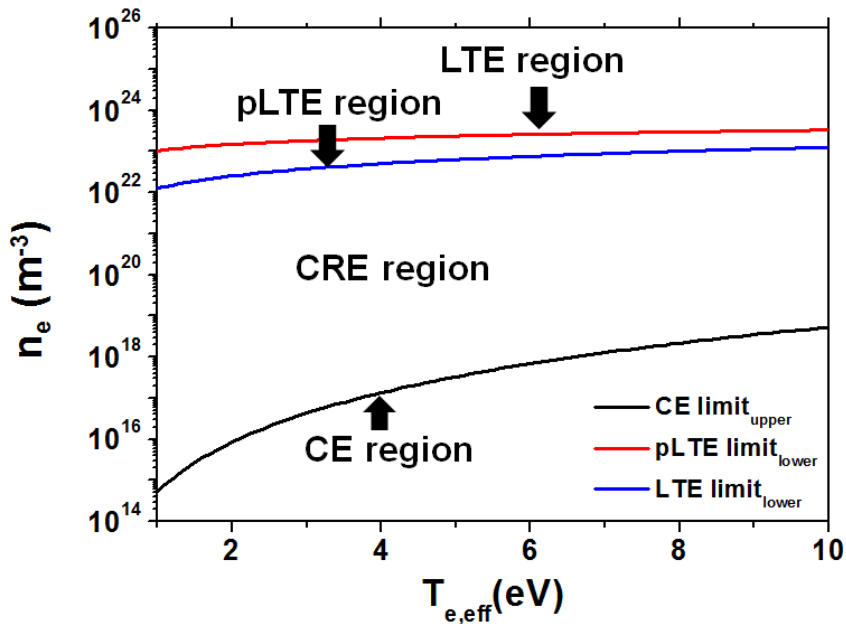


Figure 2.1 Operating region of the thermodynamic equilibrium model in terms of  $n_e$  and  $T_{e,eff}$ .

In this dissertation, only two argon emission lines are used in Eq. 2.13 to obtain  $(b, T_{eff})$ . The chosen lines have a sufficiently wide energy interval between the two threshold levels of line emissions to minimize the fitting error. For an argon plasma, one line is chosen from the lines of the excited argon atom ( $\sim 13$  eV), and the other line is from argon ion's excitation levels ( $\sim 21$  eV), which correspond to energies in the far tail of the EEDF. Because most of the inelastic processes of the ground-state neutrals in low-pressure plasmas to which the CE model can be applied are carried out by electron impact collisions, only direct ionization and excitation of argon are adopted in the calculation of Eq. 2.13. The choice of the Ar II line improves the sensitivity of the measured  $(b, T_{eff})$  compared to the case of using only Ar I lines. Selection of two emission lines requires fewer cross-section data and equations, this reduces propagation of the error. These properties of the b-factor monitoring model make the obtainment of plasma information be convenient.

### **2.3 Sensitivity of b-factor to the variation of the process plasma**

To test the sensitivity of EEDF shape factor  $b$  to the variation of the process plasma, inelastic collision rates correlated with the reaction of the metastable states in the argon plasma were perturbed by the power operating condition and the addition of oxygen to argon plasma. The variation of the EEDF shape is monitored as  $b$ -factor, and the variation mechanism of the EEDF with the plasma properties is analyzed.

### 2.3.1 Sensitivity to the metastable argon generation and stepwise ionization rate

Metastable states are very important species in the plasma-assisted chemical etching and deposition process reactions. Various inelastic collisional processes are strongly correlated with the metastable state particles, because their energy levels are located at near the ionization and the other excitation levels. Generation rates of the process reaction contributing species of reactive radical and ions are influenced by the electron impact collisional reactions of metastable states; thus, the monitoring and analysis of metastable state effects on the thermal equilibrium state of the process plasma are required function to the PI parameter. Especially for the case of pulse power applied HARC etching processes, role of the metastable species to the etch rate and etched pattern are attended [44-46]. Therefore, the detection of generation and higher order reactions of the metastable states is important to the monitoring of the process plasma information.

To test the sensitivity of introduced b-factor to the metastable argon generation and their stepwise ionization effect, experiment in the inductively coupled plasma source is performed. Figure 2.2 shows a schematic of the ICP source investigated in this work. It consists of a stainless-steel cylindrical chamber, which has a diameter of 500 mm and a length of 600 mm, and the two-turn antenna is placed on a ceramic plate. RF (radio-frequency) powers of 0.2 – 2.0 kW at 13.56 MHz (RF-10S, Advanced Energy) in intervals of 0.2 kW were delivered through the antenna. According to Hopwood, the efficiency of power coupling is nearly constant, ~ 90%, with variation in the RF power for low-pressure argon plasmas near 10 mTorr; thus, the power absorbed by the plasma in this experiment (fixed pressure at 10 mTorr) is assumed to be proportional to the applied power [47]. The argon gas flow rate was set to 100 sccm, and the chamber pressure was kept at 10 mTorr. The base pressure of this system was  $10^{-6}$  Torr; thus, the concentration of other gases should be negligible. For the optical

measurements, a CCD spectrometer (Avaspec – 2048, Avantes Inc., wavelength range of 200-1100 nm, resolution of ~0.3 nm) was employed after a relative intensity calibration. The optical fiber was placed towards the center of the plasma to monitor the b-factor. The SNRs (signal-to-noise ratios) of the chosen Ar I and Ar II peaks are about 250 : 1 and 50 : 1, respectively, which can be used for sensing variations within a few percent of the line intensity.

A planar-typed Langmuir probe, which checked the RF fluctuations by the 1st, 2nd, and 3rd band stop filters, was employed to obtain the probe data. This minimizes the interference of the RF effect in the analysis of the EEDF [48-49]. The EEDF can be analyzed according to the Druyvesteyn formula [49-51]

$$f(V) = \frac{2m_e}{e^2 A_{pr}} \left( \frac{2eV}{m_e} \right)^{1/2} \frac{d^2 I_e}{dV^2}, \quad (2.14)$$

where  $V$  is the applied voltage,  $A_{pr}$  is the area of the probe's tip, and  $I_e$  is the electron current. The plasma potential  $V_{pl}$  is the voltage where the second derivative of the electron current  $I_e$  is zero [15, 29, 49-51]. Especially, the number of high-energy electrons at the distribution tail is small, even comparable to the noise level, so the noise filtering method with bi-orthogonal wavelet and continuous wavelet transforms is used to obtain a well-smoothed EEDF without losing important information [49]. Then, the EEPFs obtained from probe data were compared to the b-factor monitored results from the OES data and the performance of b-factor as a PI parameter had evaluated.

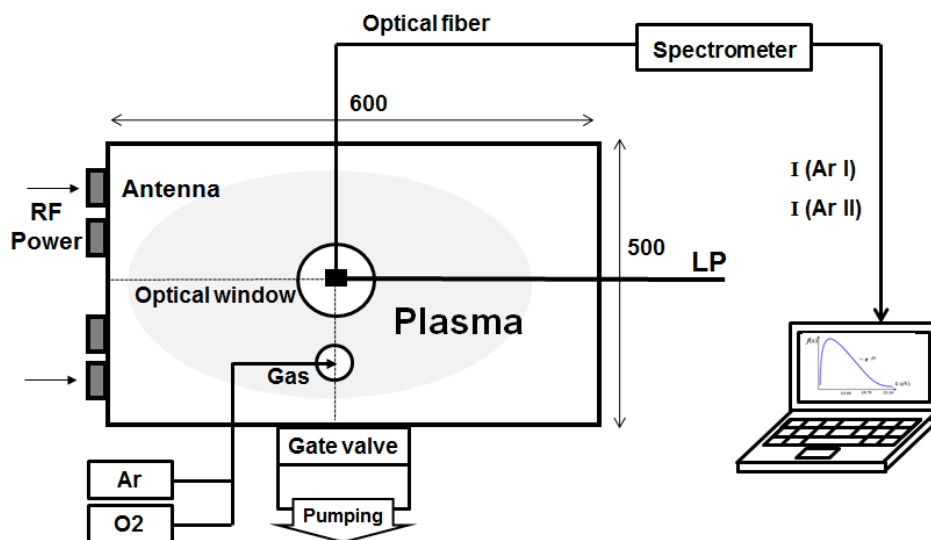
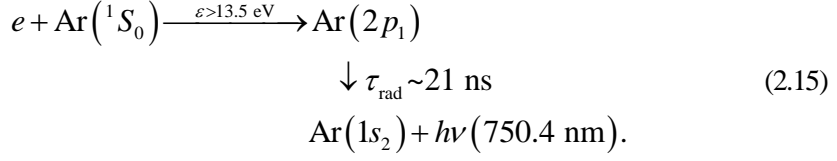


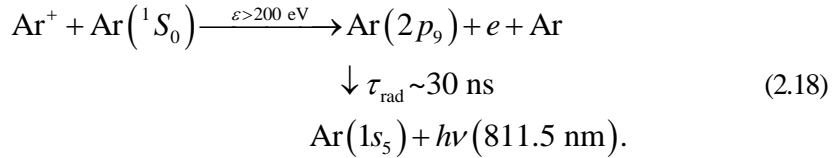
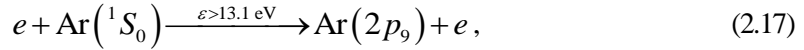
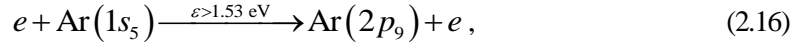
**Figure 2.2** Schematic of the experimental setup with the OES measurement system to monitor the Ar I and the Ar II lines and the Langmuir probe.

To investigate the general applicability of b-factor to the various plasma sources, we chose the second source, which is a capacitively-coupled plasma (CCP) source with 100 MHz and 0.5 kW delivered on the top electrode and 13.56 MHz with various powers (0 – 1.0 kW) delivered on the bottom electrode. The operating pressure was 20 mTorr. The same optical diagnostic system used in the ICP was set on the side window of the CCP.

The intensity ratio of Ar I (811.5 nm) to Ar I (750.4 nm) at various operating powers in the argon ICP described previously is shown in Fig. 2.3. These emission lines are deduced from the following excitation and decay reactions: **1.** Argon atoms are excited to emit the 750.4-nm line only by electron collisions with energies > 13.5 eV and spontaneously decay as [52]



2. For Ar I (811.5 nm) emission, three routes of generating the higher-energy state Ar ( $2p_9$ ) to emit the 811.5 nm line are expected [52]:



Eq. 2.16 represents the route of the collision process for low-energy electrons ( $> 1.53 \text{ eV}$ ) and argon in a metastable state ( $1s_5$ ), and Eq. 2.18 is the route for collisions between ions and neutrals while Eq. 2.17 represents direct excitation by electron impact collisions. In low-temperature plasmas, Eq. 2.18 is negligible for the 811.5-nm emission because an extremely high energy,  $> 200 \text{ eV}$ , is required. Thus, the line intensity ratio of 811.5 nm to 750.4 nm is correlated with the density of metastable argon and is useful for monitoring the variation in the density of metastable argon. This line ratio increases with increasing operating power, and the population of electrons is also increased. This means an enhanced effect for collisions of electrons and metastable argon atoms in low-pressure plasmas. At 0.8 – 1.0 kW region, increasing slope has changed where the used device shows discharge mode transition always.

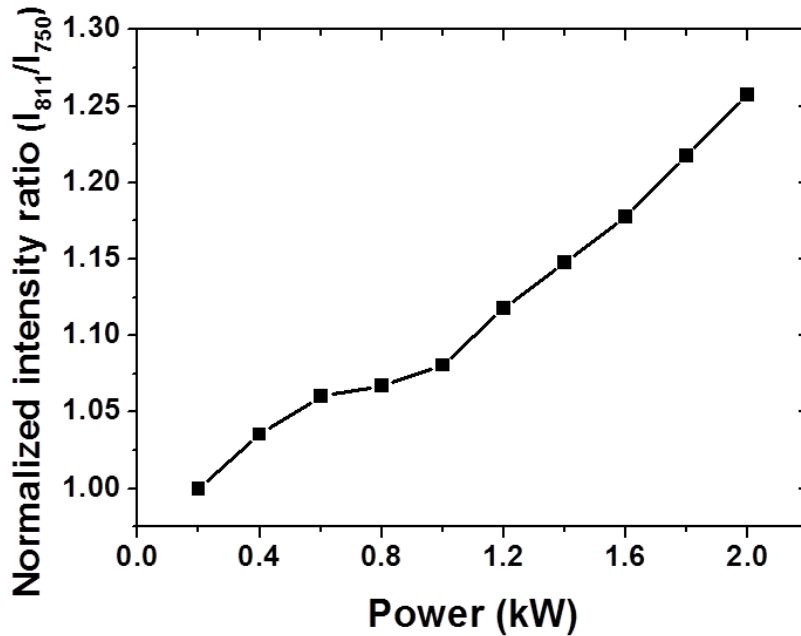


**Figure 2.3** Variation of the line emission intensity ratio (Ar I (811.5 nm) to Ar I (750.4 nm)) in a 10-mTorr argon plasma with the applied power.

Figure 2.4 shows the shape factor  $b$  of the EEDF obtained from the OES and the Langmuir probe data in the RF power range of 0.2 – 2.0 kW in an inductively-coupled argon plasma. The shape factor measured by using OES increases from 1.07 to 1.18 with increasing applied power while the shape factor measured by using the Langmuir probe is less sensitive to increase in the RF power. This is because of the low SNR of the Langmuir probe data to the high energy electrons contributing the distribution tail. Although noise filtering method is applied to the probe diagnostics, smoothed tail could not react sensitively compared to the OES signals. OES signals have high sensitivity to the high energy electron contributing phenomena because of their emission mechanism, while the Langmuir probe data is sensitive to the bulk region electrons of the distribution.

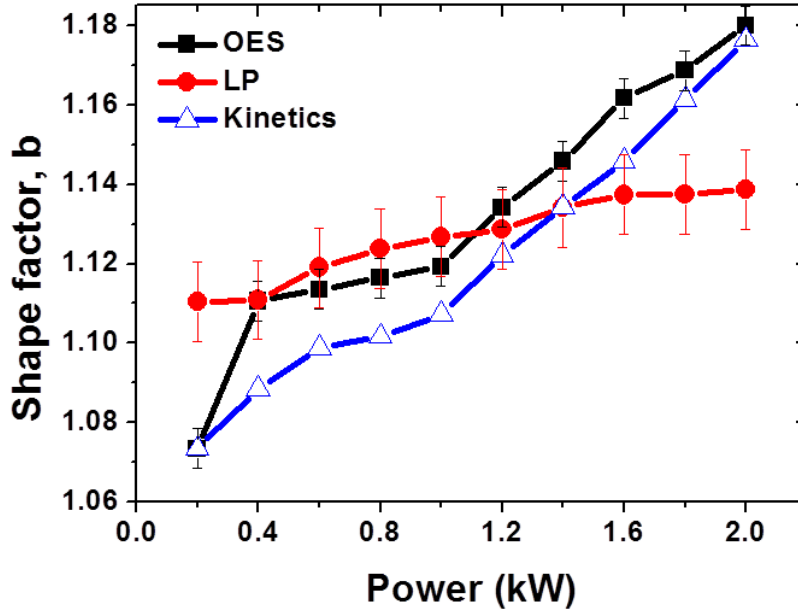


**Figure 2.4** Variation of the EEDF shape factor  $b$  in a 10-mTorr argon plasma with the applied power obtained from OES measurements (squares), Langmuir probe measurements (circles) and kinetic calculations (triangles).

In spite of the difference between the data obtained using those two techniques, both shape factors tend to increase with increasing operating power. The triangles in Fig. 2.4 represent the shape factors analyzed using the kinetic model and show a depletion of the EEDF tail with increasing power, also. The detailed reduction mechanism of the high-energy population will be discussed later. This variation of the distribution shape is visualized as EEPFs in Fig. 2.5(a) for the Langmuir probe data and (b) for the OES data. A smoothing process is performed for the Langmuir probe data, and the curve is not seriously distorted except in the low current-voltage signal SNR region, which is corresponded to the high energy region over 30 eV [49]. Both Figs. 2.5(a) and (b) show that the depletion of the tail of EEDF compare to the Maxwellian distribution with increasing applied power, and the EEPFs become convex due to

the curtailed high-energy part of the distribution. This becomes more serious with increasing applied power, thus resulting in an increase in the shape factor  $b$ , as observed in Fig. 2.4.

Figures 2.6(a) and (b) show the variation of the electron density and the effective temperature with applied power, respectively. Both the electron density and temperature have transitions at the power region of 0.8 – 1.0 kW like as the variation trend of b-factor. The electron density was measured by using the Langmuir probe, and the effective temperatures were measured from the data of the Langmuir probe and OES. The density increases and the temperature decreases with increasing power and the temperatures agree well with each other. These results indicate that the OES diagnostics is better for observing the detailed variation in the EEDF's shape, e.g., the deviation of the tail compared to Maxwellian distribution, while the Langmuir probe is a good diagnostics to measure the averaged plasma parameters, such as the electron density and the effective temperature.

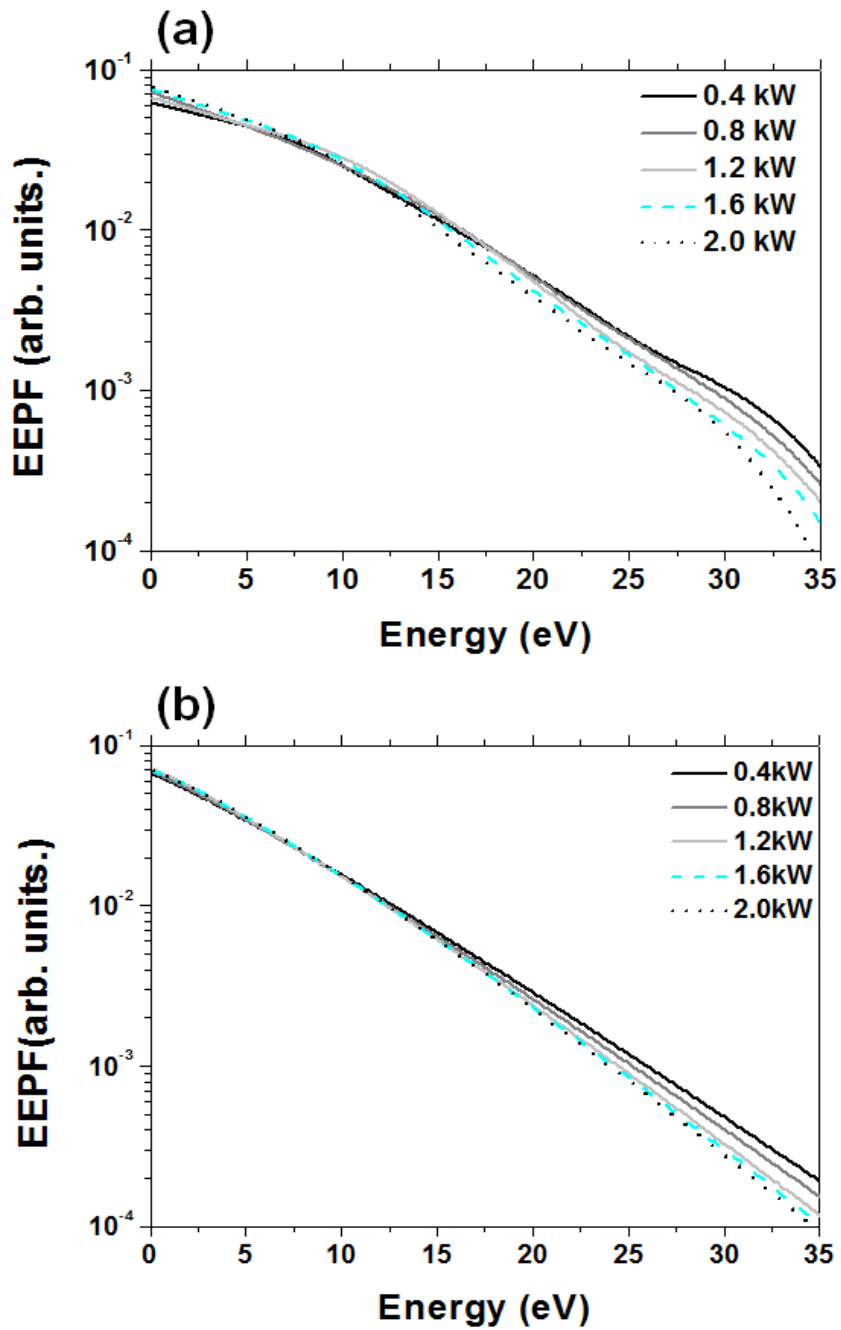
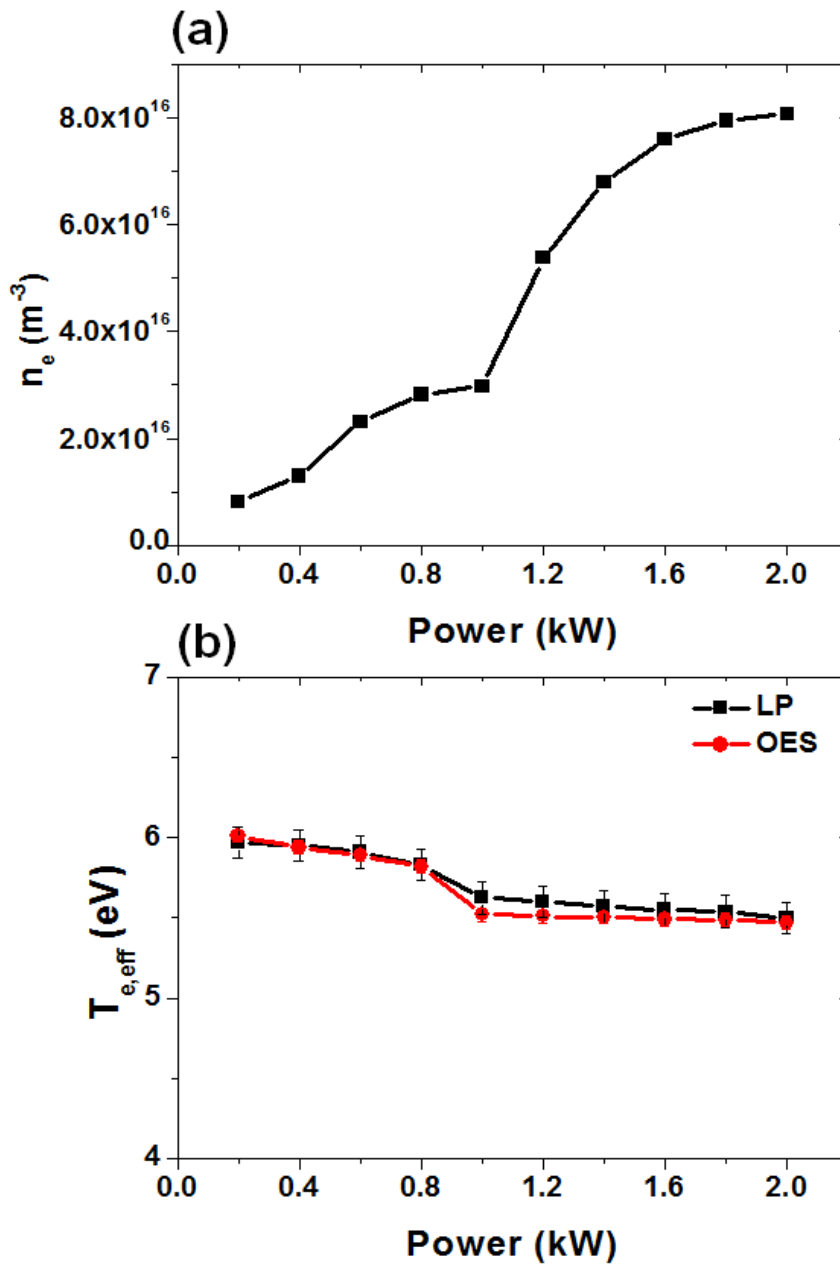


Figure 2.5 Measured EEDFs as functions of the applied power in a 10-mTorr argon discharge by using

(a) Langmuir probe data and (b) OES data.



**Figure 2.6** Plasma parameters estimated using the analyzed EEDFs as functions of the applied power:

(a) electron density measured by using a Langmuir probe and (b) effective temperature measured by using a

Langmuir probe and the OES data.

## Kinetic Analysis of the Effect of Argon Metastables on the Shape of the EEDF

The effect of electron collisions with argon metastable states on the EEDF is analyzed using a kinetic approach. According to Aliev *et al.*, the wave turbulence of the plasma governs the shaping of the particle density distribution function in velocity space [53-54]. The variation of the diffusion character in velocity space is considered as a perturbation and is analyzed in terms of the effective frequency of electron scattering. To clarify the effect of the inelastic collision properties of argon metastables on the equilibrium state of plasma, a change in the collisional diffusion coefficient was demonstrated, which causes a migration of the thermal equilibrium state of the ideal argon plasma compared to the Maxwellian plasma. The kinetic equation for analysis of the electron velocity distribution function with boundless assumptions was arranged into the following equation by Aliev *et al.* [53]:

$$v \sqrt{\frac{\nu^*(v)}{3\nu(v)}} F_0(v) = \frac{1}{2} \frac{1}{v^2} \frac{\partial}{\partial v} \left( v^2 D(v) \frac{\partial F_0}{\partial v} \right), \quad (2.19)$$

with

$$D(v) = \frac{e^2 \pi^2}{m_e^2 v^2} \int_{-\infty}^{+\infty} dk \int_0^\pi \sin \theta d\theta \times \int_0^{2\pi} \frac{d\phi}{4\pi} \left| \vec{v} \vec{E}(k) \right|^2 \delta(\omega - kv_x), \quad (2.20)$$

where  $\nu$  is the elastic collision frequency,  $\nu^*$  is the inelastic collision frequency,  $F_0$  is the spherically-symmetric part of the EEDF,  $D(v)$  is the diffusion coefficient,  $\omega$  is the RF frequency,  $k$  is the wave-number of the RF wave,  $E$  is the electric field, and  $e$  is the electron charge. The solutions to Eq. 2.19 essentially depend on the diffusion coefficient  $D(v)$ . In this dissertation, the generalized distribution function with the shape factor  $b$  is replaced by  $F_0$ . To

obtain the shape factor  $b$  by using this equation, we defined the inelastic collision frequency  $\nu^*$  with the following procedures: When test particle 1 collides with particle 2, the collision frequency is [16]

$$\nu_{12} = n_2 \sigma_{12}(v) \langle v_1 \rangle, \quad (2.21)$$

where  $n_2$  is the density of particle 2,  $\sigma_{12}$  is the collision cross-section of particles 1 and 2, and  $v_1$  is the velocity of particle 1. Using this relation, we arrange the electron-neutral effective collision frequency of the  $j$ -species gas mixture  $\nu_{eff}$  as

$$\nu_{eff} = \sum_{j=Ar, Ar^*} n_j \sigma_{ej}(v) \langle v_e \rangle, \quad (2.22)$$

where  $n_j$  is the density of gas species  $j$ , such as the ground-state argon atom and metastable argon,  $\sigma_{ej}$  is the collision cross-section of the electron and heavy particle  $j$ , and  $v_e$  is the electron velocity. With consideration of multiple inelastic collision processes, such as ionization and excitation,  $\nu^*$  in the Eq. 2.19 is treated as  $\nu_{eff}$  for the metastable state existing in argon plasmas by using the Eq. 2.22. The considered inelastic collisions of argon include the ionization and the excitation of ground-state argon atoms, the stepwise ionization of metastable argon, and the de-excitation of excited argon atoms [55]. Unstable excited states are assumed to decay spontaneously to lower states; thus, only metastable states and the ground state are considered. As described previously, the BEB-model-based total cross-section data are used in this analysis [39-41]. With Eqs. 2.1 and 2.3, Eq. 2.19 is arranged into an equation in  $b$  and the density of metastable argon, the solution to which gives the shape factor of the EEDF if the density of metastable argon is known.

To obtain the density of metastable argon, we used the measured line intensities of the Ar I (811.5 nm) and the Ar I (750.4 nm) lines, as mentioned before. The variation in density of metastable argon ( $1s_5$ ) in low-temperature plasmas can be expressed using the line intensity ratio of Ar I 811.5 nm to Ar I 750.4 nm by considering Eqs. 2.16 and 2.17:

$$\frac{I_{811nm}}{I_{750nm}} = \frac{n_{1s_5} X_{exc,16}(T_{e,eff}, b) + n_1 X_{exc,17}(T_{e,eff}, b)}{n_1 X_{exc,15}(T_{e,eff}, b)}, \quad (2.23)$$

with

$$X_{exc} = \int_{E_{thr}}^{\infty} \sigma(\varepsilon) (2\varepsilon/m_e)^{1/2} f(\varepsilon) d\varepsilon, \quad (2.24)$$

where  $n_{1s_5}$  is the number density of  $\text{Ar}(1s_5)^*$ , and  $X_{exc,N}$  is the excitation rate coefficient of route  $N$  [18]. With the line intensity ratio in Fig. 2.3, the density of metastable argon ( $1s_5$ ) can be expressed as a function of  $n_1$ ,  $T_{eff}$ , and  $b$ . With the assumption that  $n_{1s_5}/n_{1s_3}$  is almost constant in CE plasmas,  $n_1$  can be expressed as

$$n_2 = n_1 + n_{1s_5} + n_{1s_3} = n_1 + \kappa n_{1s_5}, \quad (2.25)$$

where  $\kappa$  is a constant determined by  $n_{1s_5}/n_{1s_3}$ . Here,  $n_2$  is obtained from the gas pressure. If the shape factor and the effective temperature are known, Eqs. 2.19 – 2.22 give the density of argon metastable states, and the fraction of  $n_{1s_5}$  is determined with the Eqs. 2.23 – 2.24. To determine the fraction of  $n_{1s_5}$  in the density of metastable argon, ( $b$ ,  $T_{eff}$ ) measured by using OES at 200 W is used as the reference value as the shape factor  $b$  is 1.07 and the effective

temperature  $T_{e,eff}$  is 6 eV according to Figs. 2.4 and 2.6 (b). Also, the fraction of metastable argon ( $1s_5$ ) is calculated to be about 10% of the plasma density. Then, Eq. 2.19, with the effective inelastic collision frequency of Eq. 2.22, and Eqs. 2.1 and 2.3 give the variation of the shape factor  $b$  due to the effect of the density of metastable argon. The analyzed shape factors  $b$  taken from Eqs. 2.19 – 2.25 are shown in Fig. 2.4 and are indicated by the opened triangles, which show a trend similar to the OES results with varying powers.

The shape factors of the EEDF investigated by using the effect of metastable argon with a kinetic analysis represent non-Maxwellian distribution shapes, and the shape of the EEDF becomes more differentiated from a Maxwellian distribution with increasing metastable argon fraction. Because of the inelastic collisions that are necessary to generate argon metastable states ( $\text{Ar}(1s_5)^*$  has  $E_{th} = 11.56$  eV), high-energy electrons lose their energy first. The generated metastable state particles collide with the electrons inelastically and are ionized ( $E_{th} = 15.75$  eV) or excited to higher energy levels (e.g.,  $E_{th} \sim 21$  eV for  $\text{Ar}^+$  excitation). The stepwise ionization rate coefficient of argon metastable states is about 100 times larger than that of direct ionization; thus, stepwise ionization becomes the main mechanism for electron production [56]. These collision processes reduce the fraction of high-energy electrons while low-energy electrons are generated from stepwise ionization or electron energy loss. The energy diffusion of the distribution in Eq. 2.20 is suppressed by the more frequent inelastic collisions of the electrons, and the EEDF comes to have a curtailed shape compared to that of the ideally-equilibrated states due to electron-electron collisions and electron-neutral elastic collisions. This energy-diffusion-term-based kinetic explanation physically corresponds to the report of Boffard which explains the depletion of the EEDF tail by using the transport of high-energy electrons in CRE plasmas [33]. In low-density plasmas, argon metastables are generated in a certain non-negligible portion; therefore, in argon based plasmas, the non-Maxwellian distribution can be concluded to be the general shape of the EEDF rather than the

ideal Maxwellian distribution. This implies that the shape factor  $b$  has high sensitivity to the deviation of the thermal equilibrium state of general process plasmas from the ideal state, and includes good information for the development of VM sufficiently.

### **Variation of the EEDF Shape with the Density of Metastable Argon in Capacitively-coupled Argon Plasmas**

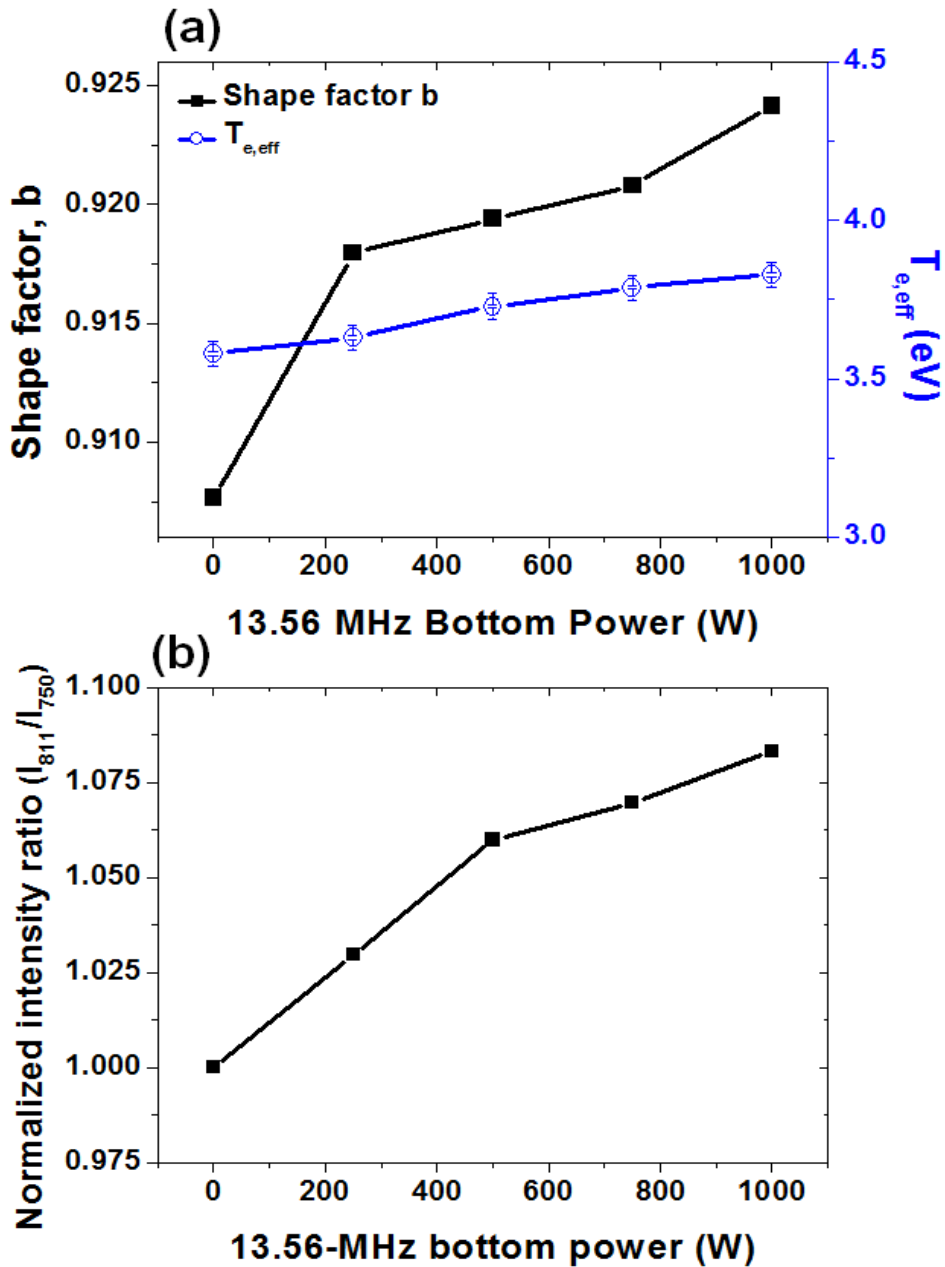
The kinetic analysis explains the effect of metastable argon in the generation of the non-Maxwellian plasmas; however, the thermal equilibrium property might be changed with the heating mechanism of the plasma sources. Thus, the variation of the EEDF was also investigated in a capacitively-coupled argon plasma for RF powers of 0 – 1.0 kW at 13.56 MHz applied to the bottom electrode.

Figure 2.7(a) shows the shape factor  $b$  of the EEDF and the effective temperature analyzed from the OES measurements as in Figs.2.4 and 2.6(b). The shape factor increases from 0.908 to 0.924, and the effective temperature increases from 3.56 to 3.83 eV with increasing bottom electrode power. Note that the shape factor is smaller than 1, which represents a bi-Maxwellian EEDF. The increase in the shape toward 1 with increasing applied power implies that the EEDF approaches a Maxwellian distribution and a single-temperature plasma. For this  $T_{e,eff} \approx 3.5$  eV plasmas, 0.04 variation of  $b$  from the Maxwellian distribution corresponds to the 10 % variation of the high-energy tail area. Here, the tail of distribution is defined as the area above  $\varepsilon > 13$  eV (emissive excitation threshold energy of Ar), and has area of  $\sim 10^{-3}$ . Therefore, 0.01 order variation of  $b$ -factor has mean of several % non-negligible variation of distribution tail.

Figure 2.7(b) shows the variation of the Ar I 811.5 nm to the Ar I 750.4 nm intensity ratio,

which is correlated with the  $\text{Ar}(1s_5)^*$  fraction, as mentioned previously. The increase in the line intensity ratio implies that a 13.56-MHz power enhances the generation of metastable argon particles in this CCP source and that the stepwise ionization rate is increased in the argon plasma. Consequently, high-energy electron impact collisions increase the generation rate of the argon plasma; thus, the population of hot electrons is reduced, and the two-temperature distribution collapses to a one-temperature distribution. Also, the properties of the electron heating can change the effective temperature, as observed in the ICP and the CCP. These information about the observed plasma is included in the monitored b-factor.

The generality of the non-Maxwellian EEDF rather than the Maxwellian EEDF in the low-density CE region of argon plasmas is investigated, and utility of b-factor as a PI parameter is evaluated. With increasing operating power, the generation of metastable argon is increased due to inelastic collisions with high-energy electrons; thus, the stepwise ionization rate is increased. The collisional energy loss rate of the high-energy electrons is enhanced with increasing operating power compared to the electron-electron collision rate or the electron-neutral elastic collision rate; thus, energy diffusion of high-energy electrons is suppressed. This mechanism is observed in the non-Maxwellian EEDF by using OES diagnostics, which is sensitive to high-energy electrons. From an analysis of the argon line intensity ratio, the detailed variation in the EEDF shape is measurable simply based on the corona equilibrium model, and this observation of b-factor gives a physical explanation for the effect of metastable argon on the properties of energy diffusion as a result of inelastic collisions with high-energy electrons.



**Figure 2.7** Variation of the plasma parameters obtained by using OES measurements in a 20-mTorr capacitively-coupled argon plasma with the applied power: (a) EEDF shape factor  $b$  (squares) and the effective temperature (circles), and (b) the line emission intensity ratio (Ar I (811.5 nm) to Ar I (750.4 nm)).

### 2.3.2 Sensitivity to the gas mixing ratio

Oxygen gas is widely used in plasma aided semiconducting device and display manufacturing processes as a gas mixture plasma with the other process gases. Properties of the plasmas are changed with the mixed O<sub>2</sub> molar fraction and the species of mixed gases. Oxygen has > 10 eV of threshold energies for generally occurred inelastic collisional reactions, such as dissociative ionization and detachment reactions. Meanwhile, the reactions with the low energy electrons as the attachment and dissociative attachment are also occurred often in the oxygen added plasma. As a result, the property of the plasma is changed sensitively and the other reaction rates in the plasma are influenced with the O<sub>2</sub> mixing ratio. Therefore, oxygen gas mixed plasma is observed to evaluate the applicability of b-factor as a PI parameter for the gas mixing ratio varying conditions.

Sato *et al.* calculated the electron density in the 100 mTorr inductively coupled O<sub>2</sub>/Ar plasmas for various O<sub>2</sub> molar fractions, and reported that the drastic decrease of electron density near at 2 % of O<sub>2</sub> abundance [57]. Hayashi *et al.* measured the density of argon metastables in O<sub>2</sub>/Ar plasmas with increase of oxygen molar fraction, and observed the transition near at 10% of oxygen addition. They explained this by the change of the O metastable quenching mechanism [58].

Monahan and Turner considered the thermal property of the O<sub>2</sub>/Ar plasmas [59], while Sato and Hayashi concentrated to the density variation of the metastable particles. They calculated the electron temperature and analyzed the effect of O<sub>2</sub> metastables as a reactant of O<sup>-</sup> detachment reactions to the electron. If O<sub>2</sub> metastable is not sufficient in O<sub>2</sub>/Ar plasmas, electron temperature does not drop with increasing oxygen molar fraction, even increases [59]. These studies show that the density of metastable species O, O<sub>2</sub>, and Ar are sensitive to the variation of the gas mixing ratio and are strongly correlated with the thermal property of the

plasma. Additionally, Gudmundsson and Liebermann reported that the importance of the type of EEDF for the property of the electronegative oxygen added plasmas. The electronegativity of O<sub>2</sub>/Ar plasma was different in Maxwellian and Druyvesteyn EEDFs [60-61].

These previous studies about the O<sub>2</sub>/Ar mixed plasma show that the plasma properties observed as the electron density, metastable state density, electron temperature, and the type of EEDF are strongly correlated with each other, but the correlations between them are nonlinear and complicated. An appropriate index applicable to the PI parameter which includes physical information about these properties of the gas mixture plasma is needed for the process state monitoring. In this section, sensitivity of b-factor to the variation of these plasma properties with varying gas mixing ratio is observed. The adequacy of b-factor to an index as a PI parameter is evaluated with physical phenomena analysis in the O<sub>2</sub>/Ar mixed plasma.

In argon plasmas, generation and stepwise ionization reactions of metastable argon by inelastic collisions with the electrons are important to determine the shape of the EEDF as described in the previous section [17]. When oxygen molecular gas is added into the argon plasma, metastables of the oxygen atom and molecules are generated and react with metastable argon; thus, the dominated reactions and the effects on the EEDF are changed with the molar fraction of added oxygen. Threshold energies of the dominated reactions govern the energy relaxation property of the fast electrons, and the kinds of dominated reaction are determined by the gas mixing ratio of the plasma. This is reflected into the EEDF shape of the gas mixture plasma.

To evaluate the performance of b-factor as a PI parameter in the gas mixture plasma, we measured the variation of EEDF in various O<sub>2</sub> concentrations in 10 mTorr inductively coupled O<sub>2</sub>/Ar plasma. And the transition of plasma properties such as the shape factor *b* of EEDF, effective electron temperature, and density of argon metastable are observed near at 10 % of O<sub>2</sub> molar fraction. This phenomenon is explained through the variation of the electron

energy relaxation mechanism with varying gas mixing ratio, and the results of the previous studies about the O<sub>2</sub>/Ar gas mixture plasmas [57-61] are also explained based on this analysis. EEDFs are measured by using an optical emission spectroscopy (OES) and Langmuir probe as used in the previous section, 2.3.1. The analysis on the phenomena in O<sub>2</sub>/Ar plasma is verified by the comparison with O<sub>2</sub>/He plasmas, as another inert gas and oxygen gas mixture plasma. Based on the measured b-factors in both of gas mixture plasmas, the effect of gas mixing ratio on the electron energy relaxation mechanism is discussed in detail.

To observe the variation of the EEDF with varying gas mix ratio in O<sub>2</sub>/Ar plasma, experimental setup shown in Figure 2.2 is reused. The RF (Radio Frequency) power of 1.0 kW at 13.56 MHz (RF-10S, Advanced Energy) is delivered through the antenna. Measurements were performed in pure argon and in O<sub>2</sub>/Ar mixtures, which were controlled by flow meters at a pressure of 10 mTorr and a total flow rate of 100 sccm. The molar fraction of added oxygen gas was varied from 0 % to 67 % in O<sub>2</sub>/Ar plasma. The base pressure of this system was 10<sup>-6</sup> Torr, thus the concentration of the existing impurities could be negligible in the analysis.

The measured EEPFs by using (a) Langmuir probe and (b) OES are shown in Figure 2.8 for various molar fractions of O<sub>2</sub> in O<sub>2</sub>/Ar plasmas. Although EEPF curves obtained by the Langmuir probe data seem to be distorted slightly above 20 eV, because of the low SNR of current-voltage signal at the high energy region, Figure 2.8 (a) and (b) show similar structures of the EEPFs.

Measured EEDF parameters of  $T_{e,eff}$  and  $b$  are shown in figure 2.9. The shape factor of the EEDF measured by the Langmuir probe is calculated by using the integrated area of EEDF tail at 13 eV (excitation threshold energy of Ar atom)  $< \varepsilon < 21$  eV (excitation threshold energy of Ar ion), and the measured EEDF parameters by two diagnostics are well agreed with each other as shown in Figure 2.9.

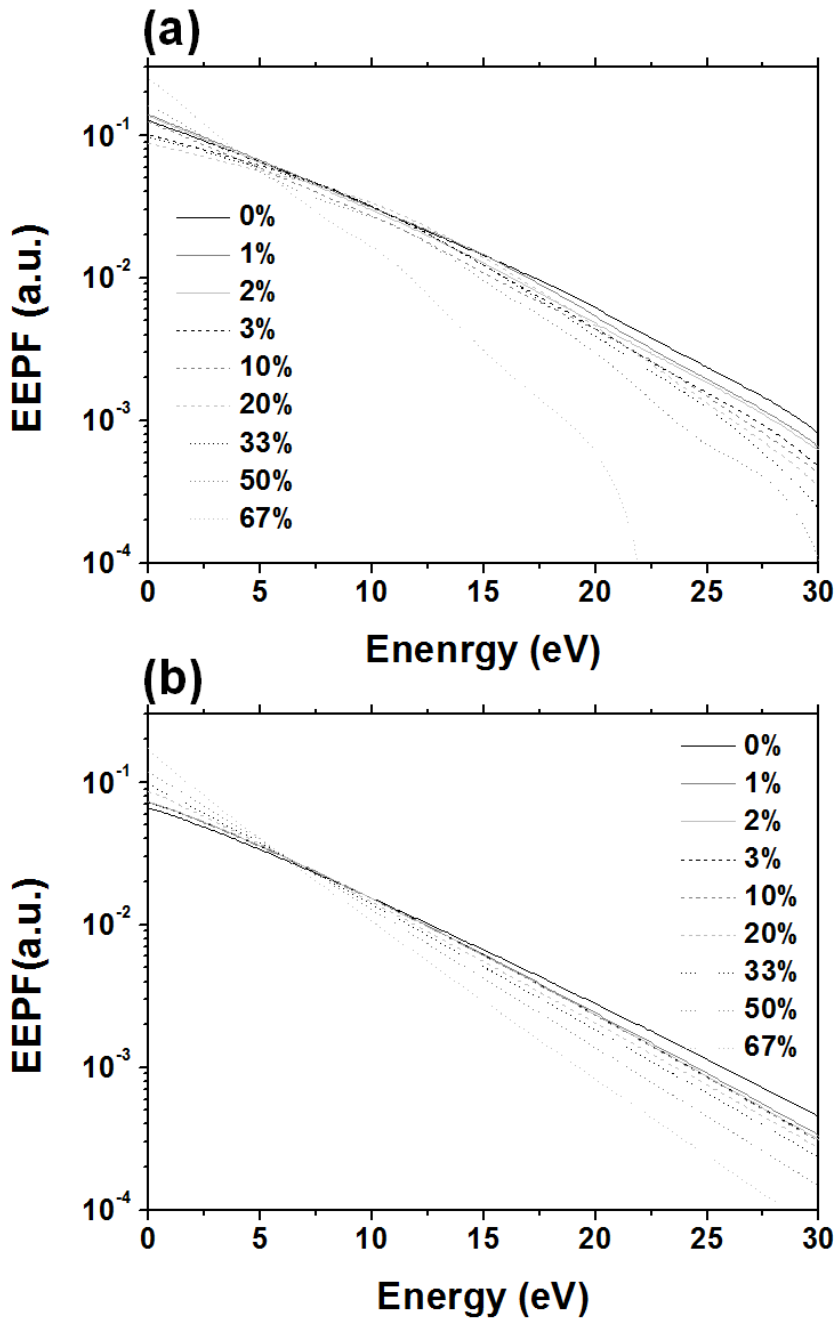


**Figure 2.8** Measured EEDFs with variation of oxygen molar fraction in O<sub>2</sub>/Ar plasma using by (a) Langmuir probe data and (b) OES data.

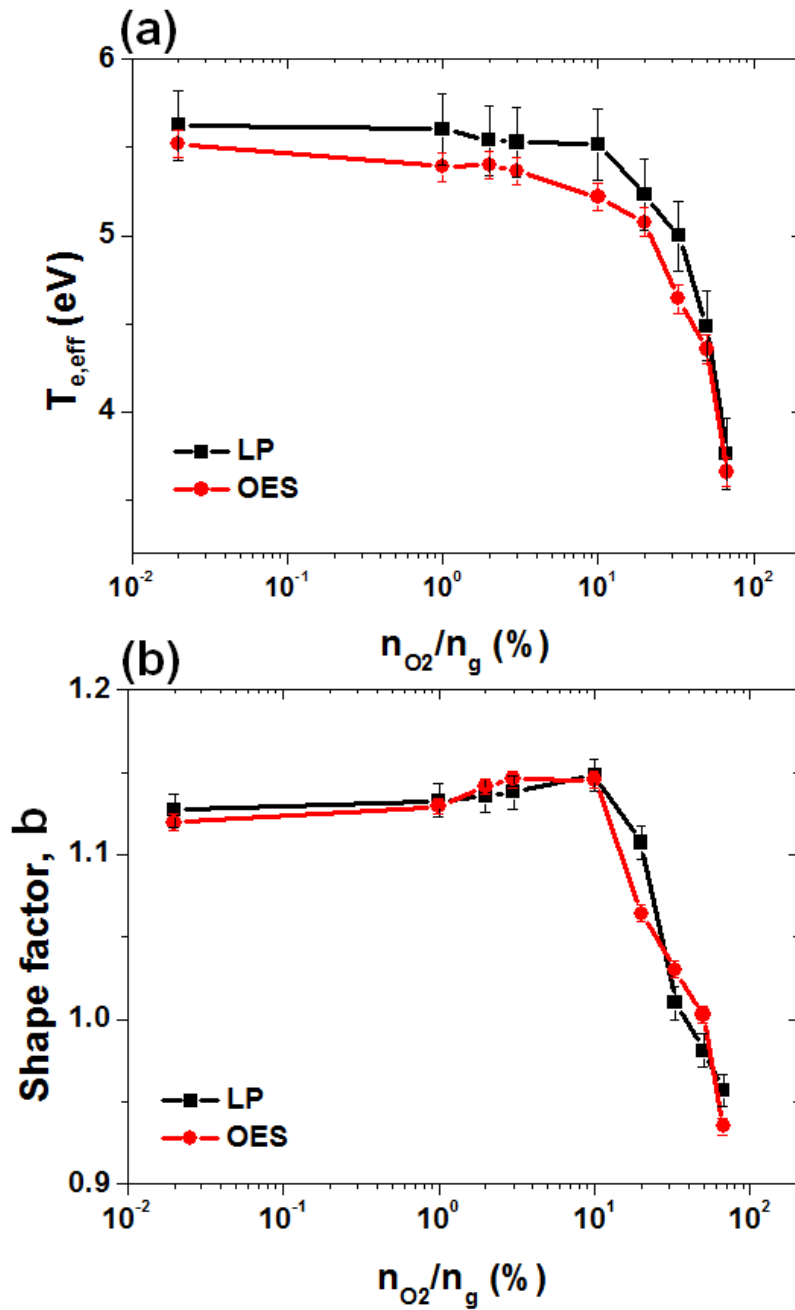


Figure 2.9 Measured EEDF describing parameter with variation of oxygen molar fraction in O<sub>2</sub>/Ar plasma : (a) effective electron temperature,  $T_{e,eff}$  (b) shape factor,  $b$ .

In the pure argon inductively-coupled plasma, the log of EEPF has a convex, negative curvature with curtailed tail part of the distribution compared to the zero-curvature Maxwellian distribution. Therefore, the b-factor of pure argon plasma has value of 1.2 larger than 1. For the generation of the metastable argon by the electron impact collisional excitation, high energy electrons with  $> 11.56$  eV lost their energies. Substantial numbers of the excited metastable argon atoms collide again with  $> 4$  eV electrons and experience stepwise ionization. This is an important density maintenance process of argon plasma, and causes high energy region curtailed non-Maxwellian distribution as reported in previous study [17, 62]. However, by the addition of oxygen molecular gas into the argon plasma, additional reactions are occurred by appearance of the various species such as  $O(^1D)$ ,  $O(^3P)$ ,  $O_2(a^1\Delta_g)^*$ ,  $O_2(b_1\Sigma_g^+)^*$ ,  $O_3$ ,  $O$ ,  $O^+$ ,  $O_2^-$ ,  $O_2^+$ ,  $O_3^-$ ,  $O_3^+$ , etc. while the only  $Ar$ ,  $Ar^*$ , and  $Ar^+$  are dominated species in the pure argon plasmas.

As shown in Fig. 2.8 and 2.9, with increase of oxygen abundance up to 10 %, the curvature of log EEPF is increased and the effective temperature is slightly decreased. Electron impact inelastic process cross section of oxygen is max 10 times larger than that of argon atom, and dissociation or dissociative ionization of oxygen molecules requires at least 10 eV of electron energy. Therefore, addition of oxygen molecule to the argon plasma causes loss of electron energies especially at the tail of EEDF. As a result, EEDF is curtailed and it is observed as the decrease of  $T_{e,eff}$  and increase of the shape factor,  $b$ .

Above 10 % abundance of oxygen molar fraction, oxygen molecules collide frequently also with the other atoms and molecules in addition to the electron impact collisions [57-58]. Inelastic processes are caused by these molecular induced collisions dominantly as Hayashi *et al.* reported [58], and increase of oxygen atom and molecule densities causes the increase of low energy electron attachment rate. The fraction of low energy electrons is decreased by the attachment reactions and the curvature of log EEPF is flattened toward near linear shape.

Figure 2.10 (a) shows the drastic decrease of the electron density measured by Langmuir probe at  $n_{O_2}/n_{Ar} > 10\%$  region where the attachment rate becomes considerable by the abundant oxygen atoms and molecules. By this low energy electron attachment effect, the shape factor  $b$  shown in Fig.2.9 (b) also drastically decreased from 1.15 to 0.94.

The slope of  $\log$  EEPF becomes steep at  $n_{O_2}/n_{Ar} > 10\%$  region as shown in Figure 2.8, because the average electron temperature of the plasma is decreased with increase of number of the electron energy loss channels by the addition of molecular oxygen. Effective temperature of the plasma shown in Fig.2.9 (a) drastically drops from 5.2 eV to 3.6 eV above  $n_{O_2}/n_{Ar} > 10\%$  with increasing oxygen molar fraction.

Figure 2.10 (b) shows the fast decrease of line intensity ratio of Ar I 811 nm to Ar I 750 nm near at  $n_{O_2}/n_{Ar} = 10\%$ . This line intensity ratio represents the quantity of  $1s_5$  metastable state argon atoms [17, 52]. By the increased number of inelastic reaction channels, reaction probabilities by the finite number of electrons are shared by the various reaction channels; thus, the generation rate of the metastable argon is relatively decreased.

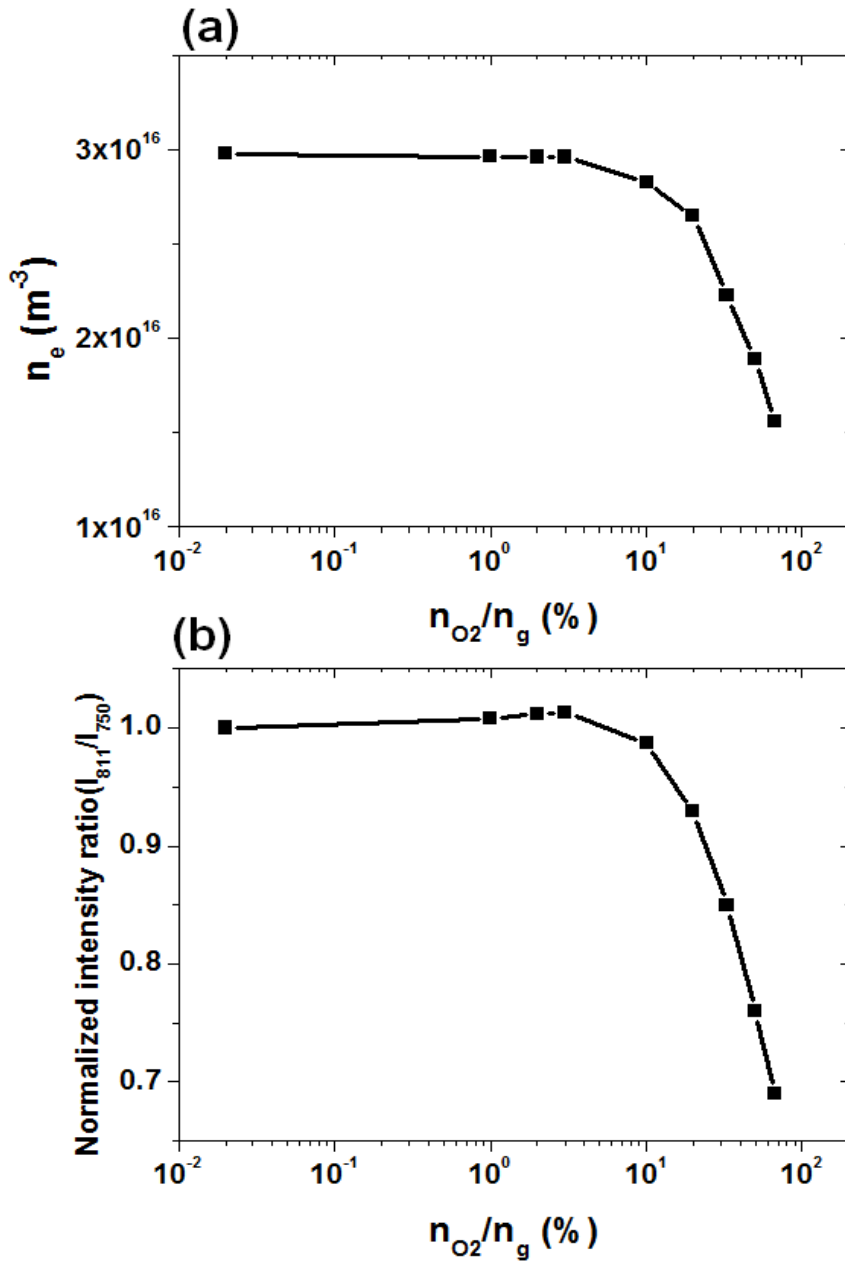


**Figure 2.10** Measured plasma parameters with variation of oxygen molar fraction in O<sub>2</sub>/Ar plasma : (a) electron density measured by Langmuir probe (b) line emission intensity ratio(Ar I(811.5 nm) to Ar I (750.4 nm)) of OES data.

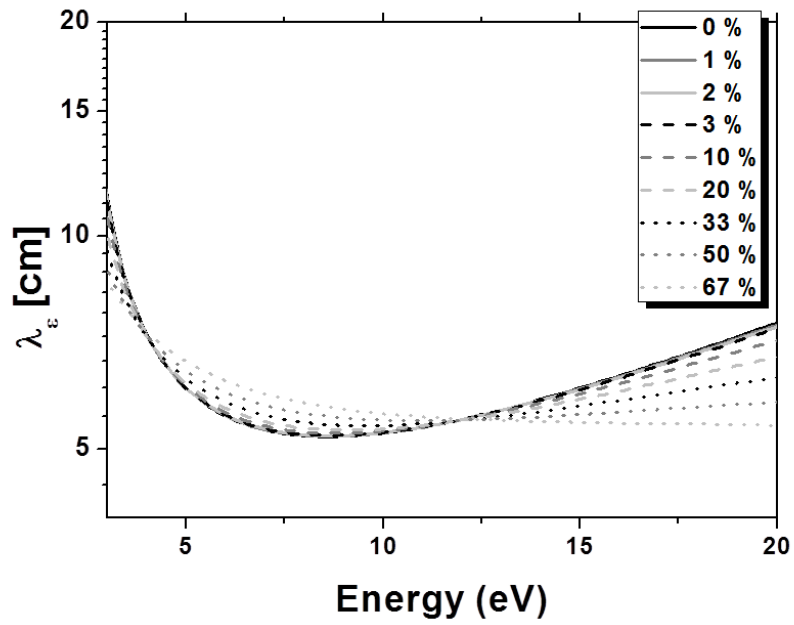
As shown in the figure 2.8, 2.9, and 2.10, the plasma properties have transition with increasing oxygen molar fraction in the O2/Ar plasma at  $n_{O_2}/n_{Ar} \sim 10\%$  region. The thermal equilibrium state of the plasma governs the electron impact ionization, excitation, and dissociation rates of the gas particles. Electrons collide elastically or inelastically with argon and oxygen gas particles and release their energies to generate dissociated, excited, and ionized species. Therefore, the transition of the argon and oxygen metastable densities at a certain gas mixing ratio (especially,  $n_{O_2}/n_{Ar} \sim 10\%$  in the O2/Ar plasmas) reported by Hayashi *et al.* [58] is strongly correlated with the variation of EEDFs shown in the Figure 2.8 and 2.9, especially the energy release properties of the electrons caused by the inelastic processes in the gas mixture plasmas. To clarify the correlation between the transition of the EEDFs and the density of the metastable states, energy relaxation mechanism of the electrons is analyzed quantitatively by using the measured b-factor.

Table 2.1 and 2.2 show the considerable electron impact collisional reaction rate constants for argon and oxygen gases, respectively. Using the listed reaction rate constants and measured EEDFs in Fig. 2.9, energy relaxation length  $\lambda_\epsilon$  of the electrons could be calculated into [15]

$$\lambda_\epsilon(\epsilon) = \frac{\sqrt{2\epsilon/m_e}}{\sqrt{3v_m(\epsilon)v_{inel}(\epsilon)}} \quad (2.26)$$

where  $m_e$  is mass of electron,  $v_m$  and  $v_{inel}$  are elastic and total inelastic collision frequencies as a function of electron energy. Because of the difference of collision cross section and reaction channels between argon and oxygen, energy relaxation length is varied with  $n_{O_2}/n_{Ar}$  as calculated in Fig. 2.11. Variation trend of the electron energy relaxation length is different according to its energy range. From this variation trend, the energy region can be classified into 3-region as  $\epsilon < 4$  eV,  $4$  eV  $< \epsilon < 11.5$  eV, and  $\epsilon > 11.5$  eV which are designated low, high,

and very high energies in this analysis, respectively.



**Figure 2.11** Calculated energy relaxation length of the electrons in terms of the electron energy with variation of oxygen molar fraction in O<sub>2</sub>/Ar plasma.

**Table 2.1.** Selected second order reaction rate constants (based on Maxwellian EEDF) for electron impact collisions in argon discharges

Reaction	Rate Constant (m <sup>3</sup> /s)	Reference
e + Ar elastic scattering	$2.336 \times 10^{-8} T_e^{1.609} e^{0.0618(\ln T_e)^2 - 0.1171(\ln T_e)^3}$	[15]
e + Ar → Ar <sup>+</sup> + 2e	$2.34 \times 10^{-8} T_e^{0.59} e^{-17.44/T_e}$	[15]
e + Ar → Ar* + e	$2.48 \times 10^{-8} T_e^{0.33} e^{-12.78/T_e}$	[15]
e + Ar → Ar (4s) + e	$5.0 \times 10^{-9} T_e^{0.74} e^{-11.56/T_e}$	[15]
e + Ar → Ar (4p) + e	$1.4 \times 10^{-8} T_e^{0.71} e^{-13.2/T_e}$	[15]
e + Ar (4s) → Ar + e	$4.3 \times 10^{-10} T_e^{0.74}$	[15]
e + Ar (4p) → Ar + e	$3.9 \times 10^{-10} T_e^{0.71}$	[15]
e + Ar (4s) → Ar <sup>+</sup> + 2e	$6.8 \times 10^{-9} T_e^{0.67} e^{-4.20/T_e}$	[15]
e + Ar (4p) → Ar <sup>+</sup> + 2e	$1.8 \times 10^{-7} T_e^{0.61} e^{-2.61/T_e}$	[15]
e + Ar* → Ar <sub>r</sub> + e	$2.0 \times 10^{-7}$	[15]
e + Ar* → Ar + e	$2.0 \times 10^{-7}$	[57]
e + Ar* → Ar <sup>+</sup> + e	Linear spline of figure 2 of [62]	[62]

**Table 2.2.** Selected second order reaction rate constants (based on Maxwellian EEDF) for electron impact collisions in oxygen discharges

Reaction	Rate Constant (cm <sup>3</sup> /s)	Reference
e + O <sub>2</sub> momentum transfer	$4.7 \times 10^{-8} T_e^{0.5}$	[15]
e + O <sub>2</sub> → O <sup>-</sup> + O	$1.07 \times 10^{-9} T_e^{-1.391} e^{-6.26/T_e}$	[15]
e + O <sub>2</sub> → 2O + e	$6.86 \times 10^{-9} e^{-6.29/T_e}$	[15]
e + O <sub>2</sub> → O <sub>2</sub> <sup>+</sup> + 2e	$2.34 \times 10^{-9} T_e^{1.03} e^{-12.29/T_e}$	[15]
e + O <sub>2</sub> → O + O <sup>+</sup> + e	$7.1 \times 10^{-11} T_e^{0.5} e^{-17/T_e}$	[15]
e + O <sub>2</sub> → O + O <sup>+</sup> + 2e	$1.88 \times 10^{-10} T_e^{1.699} e^{-16.81/T_e}$	[15]
e + O <sub>2</sub> → O <sub>2</sub> <sup>*</sup> ( <sup>1</sup> Δ <sub>g</sub> ) + 2e	$1.37 \times 10^{-9} e^{-2.14/T_e}$	[15]
e + O <sub>2</sub> → O + O( <sup>1</sup> D) + 2e	$3.49 \times 10^{-8} e^{-5.92/T_e}$	[15]
e + O <sub>2</sub> → O + O( <sup>1</sup> D) + 2e	$3.49 \times 10^{-8} e^{-5.92/T_e}$	[15]

The electrons at the high energy region from 4 eV to 11.5 eV are possible to ionize the metastable argon atoms by the stepwise ionization ( $E_{iz} = 15.75$  eV) or to excite ground state argon atoms to the metastable state ( $E_{meta} = 11.56$  eV). The energy relaxation length of this region is increased with abundance of molecular oxygen as shown in Fig. 2.11. This is the reversed result with the other energy regions. 4 eV and 11.5 eV are the threshold energies of the stepwise ionization of argon metastable and the generation of metastable state argon, respectively [62]. Abruptly increased number of reaction channels by the increase of oxygen molar fraction decreases the generation and stepwise ionization rates of argon metastables; thus, energy relaxation probability of 4 – 11.5 eV electrons falls and energy relaxation length of this region is increased.

On the contrary to this, at the low (< 4 eV) and very high (> 11.5 eV) energy regions, energy

relaxation length is decreased with increasing molar fraction of oxygen as shown in Fig. 2.11. Oxygen molecules are excited by the collision with the low energy electrons (~1-2 eV) because of the low threshold energies for excitation ( $E_{exc} = 1.2$  eV), while the dissociative ionization or ionization of molecular oxygen has high threshold energies (> about 12 eV) [41]. Abundance of the molecular oxygen causes the decrease of electron energy relaxation length at these regions by the frequent inelastic collisions of these region electrons and resulted in the Fig. 2.11.

By the variation of the electron energy relaxation length at each of the energy region with increase of the oxygen molar fraction, the change of the thermal equilibrium state of the electrons could be explained. As Godyak *et al.* analyzed, the shorter energy relaxation length of the electron, the more frequent energy loss is occurred [21]. Therefore, if the electron energy relaxation length of a certain energy region is decreased, the fraction of that energy region in the EEDF becomes smaller by the energy loss of the electrons. According to this, results in Fig.2.9 can be explained using the Fig. 2.11. The increase of energy relaxation length at 4 - 11.5 eV high energy region can be resulted in the development of the EEDF tail, and this is observed as the small shape factor  $b$  for the oxygen abundant O<sub>2</sub>/Ar plasmas. This transition of collision property causes the overall variation of the coupled plasma parameters which are measured as the metastable species densities, electron density, and EEDF parameters. In addition to the electron energy relaxation mechanism, overall collisional reactions are considered to explain the drastic variations of the plasma parameters at a certain mixing ratio,  $n_{O_2}/n_{Ar} \sim 10\%$ , in the O<sub>2</sub>/Ar plasmas.

Figure 2.12 shows the total reaction rates per argon or oxygen particle. Total reaction rates are normalized by the molar fraction considered density of the gas particles and the electron density for the given discharge condition. The black solid line and dashed gray line represent the total reaction rate of argon atoms and oxygen molecules by the electron impact collisions,

respectively. The cross point of these lines is located near at  $n_{O_2}/n_g \sim 10\%$ , which means that the energy loss rate of the electrons caused by oxygen molecules overcomes that caused by argon atoms. Although the molar fraction of oxygen is about 1/10 of argon at this point, the total electron impact collision rates of oxygen molecules are higher than that of argon atoms because of the various reaction channels of oxygen molecules. Thus, the overall energy loss of the electrons become about twice of the pure argon plasma, in this point. As a result, the effective electron temperature drops rapidly in this mixing ratio point and this explains the measured results of the Figure 2.9 (a).

The gray line in Fig. 2.12 represents the total neutral particle impact collision reaction rate of oxygen molecules. The detailed reactions with argon metastable state included in the calculation of the reaction rates are shown in Table 2.3. The dashed gray line and gray solid line is crossed at  $n_{O_2}/n_g \sim 10\%$  also. This shows that the dominated oxygen reaction mechanism is changed from the electron impact collision to the neutral particle impact collision with increase of the molar fraction of oxygen at  $n_{O_2}/n_g \sim 10\%$ .

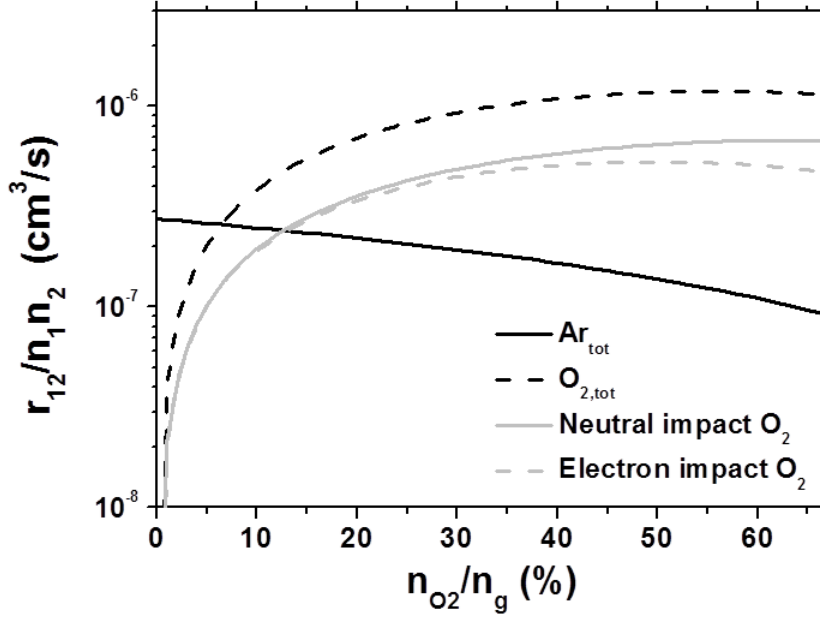


**Figure 2.12** Normalized reaction rates by the molar fraction of the composing gases at  $T_{e,eff} = 5$  eV with variation of oxygen molar fraction in O<sub>2</sub>/Ar plasma.

**Table 2.3.** Selected second order reaction rate constants (based on Maxwellian EEDF) for neutral reactions in O<sub>2</sub>/Ar discharges

Reaction	Rate Constant (cm <sup>3</sup> /s)	Reference
$\text{Ar}^* + \text{Ar}^* \rightarrow \text{Ar}^+ + \text{Ar} + e$	$5.0 \times 10^{-10}$	[57]
$\text{Ar}^* + \text{Ar} \rightarrow 2\text{Ar}$	$3.0 \times 10^{-15}$	[57]
$\text{Ar}^* + \text{O}_2 \rightarrow \text{Ar} + \text{O} (^3\text{P}) + \text{O} (^3\text{P})$	$9.7 \times 10^{-11}$	[57]
$\text{Ar}^* + \text{O}_2 \rightarrow \text{Ar} + \text{O} (^3\text{P}) + \text{O} (^1\text{D})$	$1.1 \times 10^{-10}$	[57]
$\text{Ar}^* + \text{O}_2 \rightarrow \text{Ar} + \text{O} (^3\text{P}) + \text{O} (^1\text{S})$	$4.2 \times 10^{-12}$	[57]

As explained by using Fig. 2.12, the dominated oxygen collisional reaction is converted from the electron impact to the neutral impact collisions at  $n_{O_2}/n_g \sim 10\%$ . Especially, collision rate of Ar metastable with molecular oxygen to generate O ( $^1D$ ) is also highly increased; thus, the stepwise ionization rate of Ar metastable is relatively dropped and promotes the decrease of the electron density. In addition, the de-excitation mechanism of O ( $^1D$ ) is changed from the electron impact quenching to the molecule impact quenching for high oxygen abundance as suggested by Hayashi *et al* [58]. These phenomena are caused by the own properties of argon and oxygen. Most of the metastable generation reaction threshold energies of the argon atom and oxygen molecules are located at about 10 eV; thus, the electron impact collision with each of species is competitive. If their reaction thresholds were far away apart, increased number of the reaction channels by the addition of the oxygen molecules would not change the energy relaxation property of the electrons.

To verify this explanation, change of the EEDFs in O<sub>2</sub>/He plasma was observed in terms of the b-factor and  $T_{e,eff}$ , and the reaction rates per particles are analyzed as performed for O<sub>2</sub>/Ar plasma. To monitor the PI parameter  $b$ , 1 % partial pressure of argon gas is added into the O<sub>2</sub>/He plasma like as an actinometry and the effect of metastable argon is neglected in the analysis. Helium is inert gas like as argon, thus O<sub>2</sub>/Ar and O<sub>2</sub>/He plasmas have similarity as inert gas + molecular oxygen combination. But, helium has very high threshold energies for the reactions such as ionization ( $E_{iz} = 24.58$  eV) and excitation ( $E_{exc} = 21.2$  eV); thus, the reaction energy region of helium atom is not shared with molecular oxygen otherwise the argon atom [40-41]. The inelastic collision rates between helium and oxygen particles are negligible compared to the electron impact collisional reaction rates as shown in Table 2.4 and Table 2.5 because of very high threshold level of the helium atoms (min. over  $\sim 20$  eV). Fig. 2.13 shows the reaction rates per particle for O<sub>2</sub>/He plasmas like as Figure 2.12 of O<sub>2</sub>/Ar plasmas, and Fig. 2.14 shows the measured EEDF parameters of the effective electron

temperature in (a) and the b-factor in (b). The gray solid and black solid lines in Fig. 2.13 are not crossed at any mixing ratios, thus the energy relaxation property of the electrons which governs the shape of EEDF is not changed and this information about the plasma property is monitored by the b-factor as shown in Fig. 2.14 (b). On the other hand, the total electron impact collisional reaction rate of the O<sub>2</sub>/He plasma is increased with increasing oxygen molar fraction. This is caused by the increase of total numbers of the electron energy loss channels, and Fig. 2.14 (a) shows coincident results with this analysis. These results support the analysis on the electron energy relaxation mechanism in gas mixture plasmas, and show the representability of the thermal equilibrium property to these kinds of reaction mechanisms.

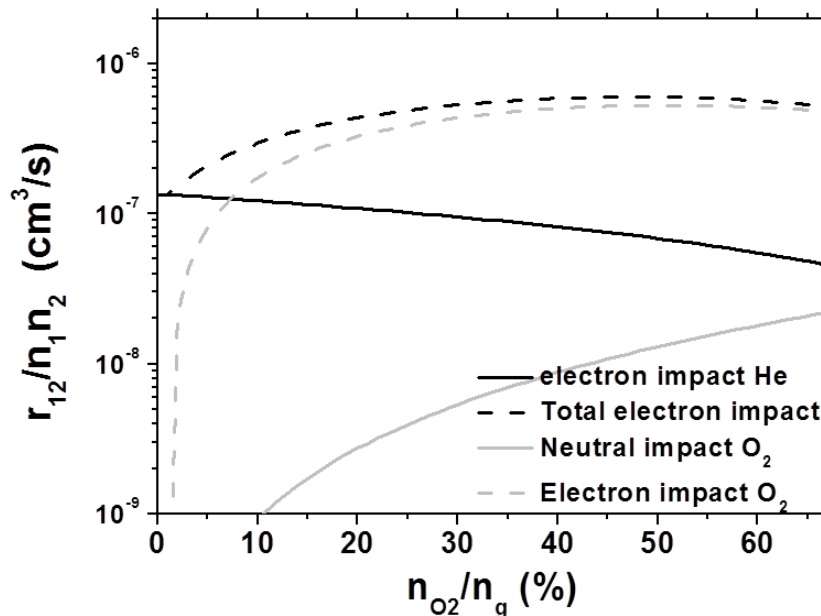


**Figure 2.13** Normalized reaction rates by the molar fraction of the composing gases at  $T_{e,eff} = 5$  eV with variation of oxygen molar fraction in O<sub>2</sub>/He plasma

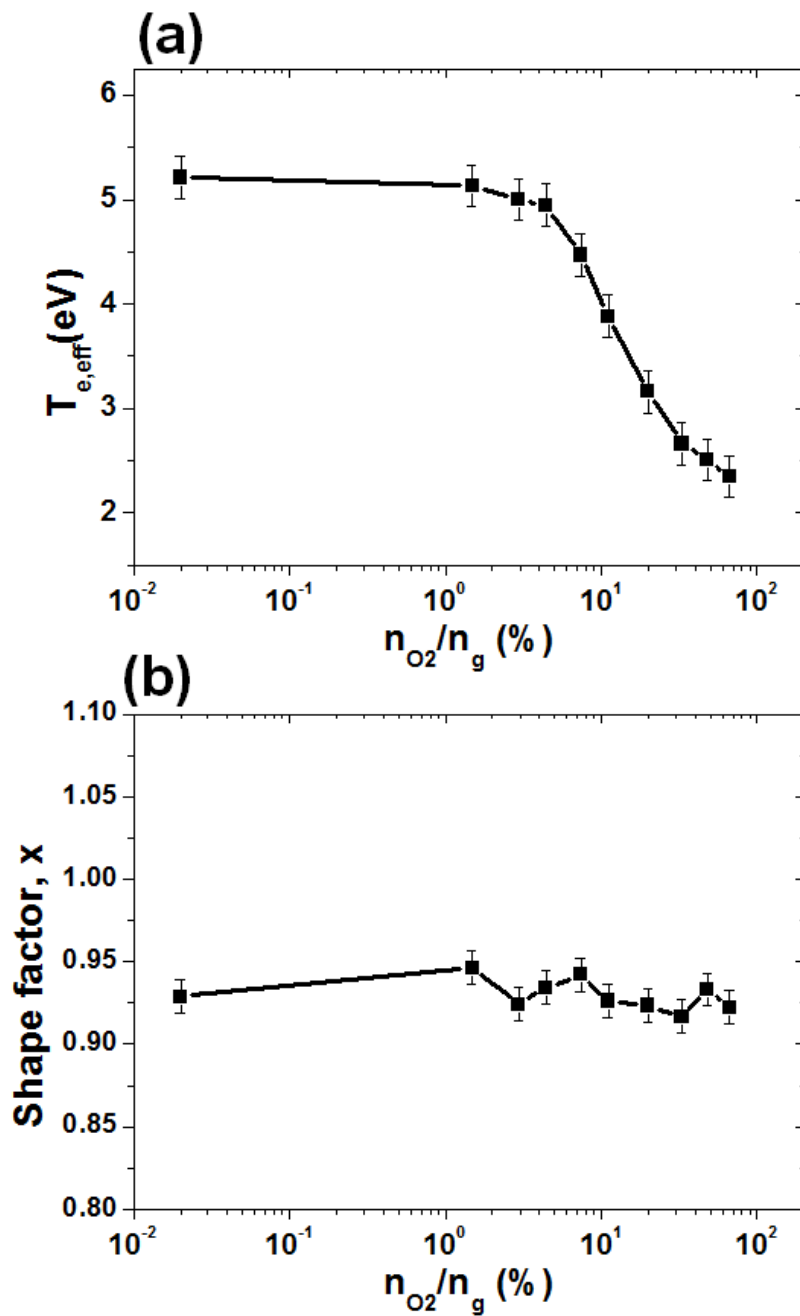


**Figure 2.14** Measured EEDF describing parameter with variation of oxygen molar fraction in O<sub>2</sub>/He plasma : (a) effective electron temperature,  $T_{e,eff}$  (b) shape factor,  $x$ .

**Table 2.4.** Selected second order reaction rate constants (based on Maxwellian EEDF) for electron impact collisions in helium discharges

<b>Reaction</b>	<b>Rate Constant (cm<sup>3</sup>/s)</b>	<b>Reference</b>
e + He elastic scattering	$8.37 \times 10^{-10}$	[41]
e + He $\rightarrow$ He* + e	$2.308 \times 10^{-10} T_e^{0.31} e^{-19.79/T_e}$	[63]
e + He $\rightarrow$ He <sup>+</sup> + 2e	$2.584 \times 10^{-12} T_e^{0.68} e^{-24.6/T_e}$	[63]

**Table 2.5.** Selected second order reaction rate constants (based on Maxwellian EEDF) for neutral reactions in O<sub>2</sub>/He discharges

<b>Reaction</b>	<b>Rate Constant (cm<sup>3</sup>/s)</b>	<b>Reference</b>
He* + O <sub>2</sub> $\rightarrow$ He + O <sub>2</sub> <sup>+</sup> + e	$2.4 \times 10^{-10}$	[64]

The thermal equilibrium properties of the plasmas in gas mixture plasmas are determined by the own property of consisting gas species which is the reaction threshold energies of the dominated inelastic collisional reactions in the given discharge condition. Correlated phenomena with this property of gas mixture plasma could be analyzed by using the monitored b-factor of the plasma, because the information about electron energy relaxation mechanism can be represented by the shape factor of the EEDF. This infers that the variation of the plasma properties caused by the variation of the gas mixing ratio can be monitored using the b-factor as a PI parameter. For the gas mixing ratio varying cases in the process plasmas, e.g., vacuum leakage inflow, wall contamination, adsorption of residual gas, variation of the pumping condition, etc., b-factor monitoring would give information about the state of process plasma sensitively.

## **Chapter 3 . Plasma Information Based VM(PI-VM) Model for Plasma Etching Process**

### **3.1 Experimental setup and access of sensing data**

To develop the VM model of selected target process of C4F8-oxide etch in section 1.4 for the prediction of etch rate, various sensor and EES data as state variable are obtained in the triple-frequency power applied narrow gap capacitively-coupled plasma (TF-CCP) etcher. Figure 3.1 shows the schematics of the experimental apparatus. TF-CCP reactor used in this dissertation has typical dimensions of parallel plate electrode for 300 mm wafer processing. The RF powers were introduced into the chamber through the top electrode with 100 MHz RF power supply and the bottom electrode with 13.56 MHz and 2 MHz RF power supply. Gas inlets in the showerhead delivered the reactant gases of Ar, C4F8, and O2 through the GFS (Gas Flow Split) into the chamber volume. The chamber was pumped out with a turbo molecular pump to a base pressure of 0.2 mTorr. Chamber wall and electrodes were maintained at a constant temperature by heater and chiller. ESC (Electro-static Chuck) of bottom electrode grabbed a wafer through DC power supply and performed cooling of wafer through helium flow. The etching was performed using patterned wafer coupons made from metal contact (MC) etch process in DRAM (Dynamic Random Access Memory). The variables related to plasma etching process are classified into 3 groups; manipulated variables (MVs), state variables (SVs) and performance variables (PVs). MVs are independent variables to be controlled for a particular effect. SVs such as temperature, pressure, gas flows, and power are collected from etch reactors using in-built sensors and EES data.

PVs and output variables are desired to be applied for prediction of etch rate in the context. Actual etch rate was measured by using V-SEM. The standard process condition for oxide etching in this experiment was set to 20 mTorr with the gas flow rate of 400 sccm, 50 sccm, and 30 sccm for Ar, C4F8, and O2, respectively, 100 MHz, 13.56 MHz, and 2 MHz power supply delivered 300 W, 1000 W, and 300 W to TF-CCP, respectively. The etch process for building VM system was repeated 50 times in reference process fixed condition.

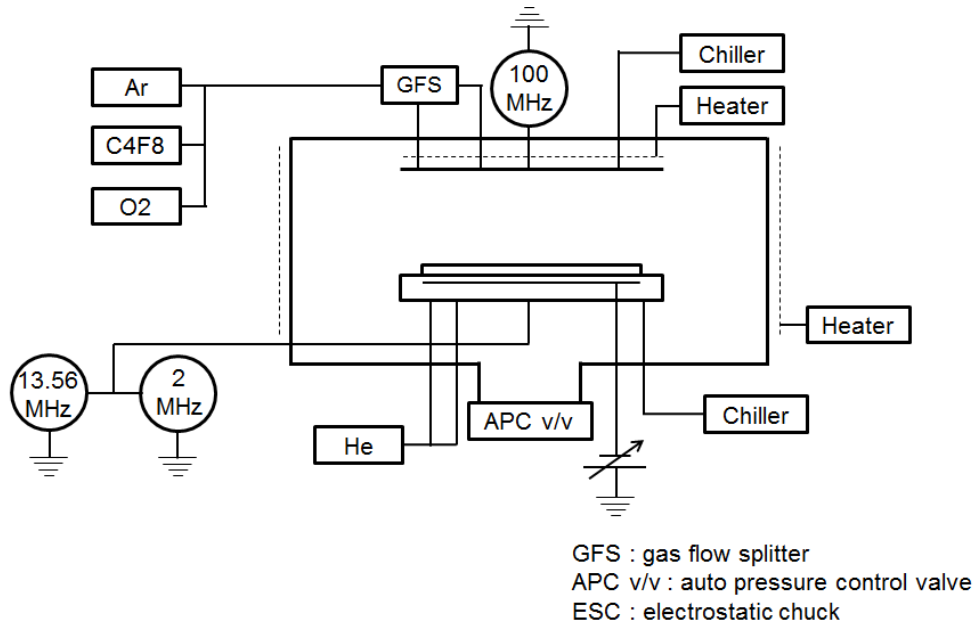


**Figure 3.1** The schematics of the TF(Triple-Frequency) – CCP etcher.

The optical measurements were conducted using a CCD spectrometer (SD1024DL, Verity Instruments, Inc., wavelength range of 200-800 nm, resolution < 2.0 nm). The optical fiber was placed toward the center of the plasma and signals of total 1600 wavelengths were measured with 0.5 sec of time resolution.

At first, the 70 kinds of EES parameters were monitored with 0.5 sec of time resolution. EES data represent the conditions of applied power, power matching conditions, pressure gauge, temperatures of the electrodes, heater, and chiller, and gas flow conditions monitored at MFC (Mass Flow Controller), etc. 24 EES SVs selected by the sensitivity ranking test to the MVs are monitored as EES data and listed in Table 3.1 [65].

Total 1670 parameters from the OES and EES signals are reduced into 79 parameters according to the sensitivity test of the parameters to the operating conditions [65-66]. Using these reduced optical and EES signals, development of the VM of the etch rate was performed.

**Table 3.1** The list of monitored EES SVs after the sensitivity test.

No.	EES SV	unit	SV
1	1000mT_Gauge	mTorr	High vacuum gauge
2	Top_Temp	K	Top electrode temperature
3	Bottom_Temp	K	Bottom electrode temperature
4	TRF_FwdPwr	W	Top electrode applied power
5	TRF_RefPwr	W	Top electrode reflected power
6	HRF_PwrStpt	W	Bottom electrode applied high-frequency power set value
7	HRF_FwdPwr	W	Bottom electrode applied high-frequency power
8	HRF_RefPwr	W	Bottom electrode reflected high-frequency power
9	LRF_PwrStpt	W	Bottom electrode applied low-frequency power set value
10	LRF_FwdPwr	W	Bottom electrode applied low-frequency power
11	LRF_RefPwr	W	Bottom electrode reflected low-frequency power
12	TRM_LoadPos	a.u.	Position of top electrode matcher load cap

13	TRM_TunePos	a.u.	Position of top electrode matcher tune cap
14	HRM_LoadPos	a.u.	Position of bottom electrode high-frequency matcher load cap
15	HRM_TunePos	a.u.	Position of bottom electrode high-frequency matcher tune cap
16	LRM_LoadPos	a.u.	Position of bottom electrode low-frequency matcher load cap
17	LRM_TunePos	a.u.	Position of bottom electrode low-frequency matcher tune cap
18	Ar_Flow	Sccm	Ar flow
19	C4F8_Flow	Sccm	C4F8 flow
20	O2_Flow	Sccm	O2 flow
21	CHL1_Temp.	K	Chiller 1 temperature
22	CHL2_Temp.	K	Chiller 2 temperature
23	eTVP_Press	mTorr	Turbo molecular pump pressure
24	eTVP_Posit	a.u.	Position of the gate valve

### 3.2 Main and sub PI parameters based on the etching process reaction mechanisms

C4F8 plasma-assisted silicon oxide etching is a typical reaction of the halogen-silicon reaction based processes. The most basic etching reaction mechanism of the silicon is the chemical reaction by the halogen species, representatively fluorine is [15]:



According to this, etch rate is proportional to the flux of reactive radical on to the substrate surface, simply. In this case, flux of fluorine is the determinant of etch rate. However, there are 4 basic low-density plasma processes commonly used to remove material from the surfaces: (1) sputtering, (2) pure chemical etching, (3) ion energy-driven etching, and (4) ion-enhanced inhibitor etching [15].

**1.** Sputtering is the ejection of atoms from surfaces due to energetic ion bombardment. The discharge supplies energetic ions to the surface, with the ions typically having energies above a few hundred volts. Sputtering is an unselective process since, the sputtering yield at a given ion energy depends on the surface binding energy and weakly on the masses of the targets and projectiles. Typically, these do not vary by more than factor of 2-3 among different materials. Hence the sputtering rates are generally low because the yield is typically of order one atom per incident ion, and ion fluxes incident on surfaces in discharges are often small compared to commercially significant rates for materials removal.

**2.** The second etch process is pure chemical etching, in which the discharge supplies gas-phase etchant atoms or molecules that chemically react with the surface to form gas-phase products. This process can be highly chemically selective. The chemical etching is almost invariably isotropic, since the gas-phase etchants arrive at the substrate with a near uniform angular distribution. Therefore, unless the reaction is with a crystal having a rate depending on crystallographic orientation, one may expect a relatively isotropic etch rate. The etch products must be volatile. The etch rate can be quite large because the flux of etchants to the substrate can be high in processing discharges.

**3.** The third etch process is ion-enhanced energy-driven etching, in which the discharge supplies both etchants and energetic ions to the surface. The combined effect of both etchant atoms and energetic ions in producing etch products can be much larger than that produced by either pure chemical etching or by sputtering alone. Previous studies suggest that the etching is

chemical reaction in nature, but the energetic ion bombardment is also an important etch rate determinant [67-70]. The etch rate generally increases with increasing ion energy above a threshold energy of a few volts. The etch product must be volatile, as for pure chemical etching [15]. Because the energetic ions have a highly directional angular distribution when they strike the substrate, the etching can be highly anisotropic. However, ion energy-driven etching may have poor selectivity compared to pure chemical etching. The trade-off between anisotropy and selectivity is important in designing etch processes [71].

**4.** The fourth type of etch process, ion-enhanced inhibitor etching, which involves the use of an inhibitor species. The discharge supplies etchants, energetic ions, and inhibitor precursor molecules that adsorb or deposit on the substrate to form a protective layer or polymer film [15]. The etchant is chosen to produce a high chemical etch rate of the substrate in the absence of either ion bombardment or the inhibitor. The ion-bombarding flux prevents the inhibitor layer from forming or clears it as it forms, exposing the surface to the chemical etchant [15, 72]. Inhibitor precursor molecules include  $CF_2$ , and  $CF_3$  molecules for fluorocarbon plasma-aided etching process, which can deposit on the substrate to form fluorocarbon polymer films [73]. Ion bombardment clears the film from the trench bottom, allowing the etch process to proceed there. Contamination of the substrate and final removal of the protective inhibitor film are other issues that must be addressed for these etching processes.

These 4 etching mechanisms commonly emphasize that the cooperation of the chemical etch effects by the reactive radical species and physical etch effects by the ion bombarding energy. The generation of reactive radical and ion species contribute to the chemical etch effect is occurred in the plasma volume, and the ions accelerated through the sheath of the plasma onto the surface contributes to the physical etch effects. Transferred ions and their energies determine the reaction properties on the surface. To analyze these reactions for the target process,  $C_4F_8$  based plasma-assisted oxide etch, reaction mechanisms in the volume, sheath,

and surface of this plasma are reviewed and PI parameters representing these reactions are introduced.

### 3.2.1 Volume reactions and the main PI, b-factor

In the C<sub>4</sub>F<sub>8</sub> plasma, various fragment species of fluorocarbon are generated by the electron impact collision and collisions between heavy particles [75]. To obtain high etch rate, generation of specific species are preferred while the generation of the other species which are correlated with polymer formation are not preferred. Preferred species for the high etch rate are (1) F radical and F<sup>+</sup> ion, and (2) Light ions of the fluorocarbon fragments (CF<sup>+</sup>, CF<sub>2</sub><sup>+</sup>,...) [75-77]. Therefore, to obtain high etch rate, generation rate of these light species should be kept high. On the other hand, the generation of heavy fluorocarbon ions such as C<sub>2</sub>F<sub>4</sub><sup>+</sup>, C<sub>3</sub>F<sub>5</sub><sup>+</sup>, ..., etc., and heavy fragments radicals is required to be suppressed to prevent the polymer deposition. Fig. 3.2 shows the schematic of reaction roots by the electron impact collision for C<sub>4</sub>F<sub>8</sub> [75]. The thickness of arrow represents the reaction rate constants for the general temperature of process plasmas. By the electron impact collisions, most of C<sub>4</sub>F<sub>8</sub> is cracked into the C<sub>2</sub>F<sub>4</sub> by the dissociation, and C<sub>2</sub>F<sub>4</sub><sup>+</sup> and C<sub>3</sub>F<sub>5</sub><sup>+</sup> ions are also generated by the dissociative ionization. These heavy ions are not preferred to the etch reaction. Dominated fragment, C<sub>2</sub>F<sub>4</sub> reacts again with the electrons and generates lighter ion and radicals. Dashed lines with on the arrow denote that the preferred reaction roots to obtain high etch rate.

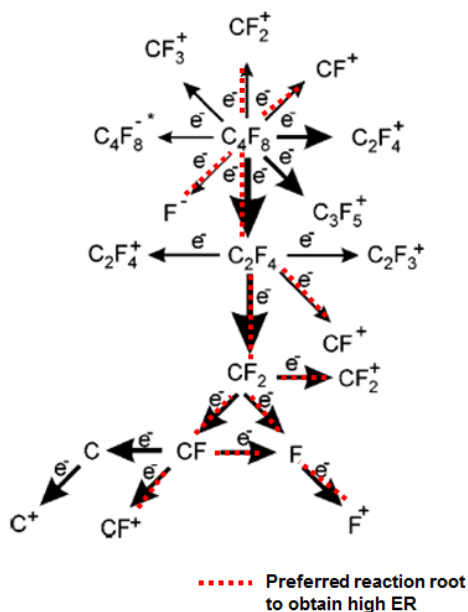


**Figure 3.2** Schematic of electron impact reactions of C<sub>4</sub>F<sub>8</sub>. The thickness of arrows represent the value of reaction rates calculated for an ICP at 6 mTorr, 600 W, 13.56 MHz [75].

The light positive ion species of fluorocarbon is generated by the dissociative ionization of C<sub>4</sub>F<sub>8</sub> and C<sub>2</sub>F<sub>4</sub>. This means that the required threshold energies and cross sections for the dissociative ionization reactions of these fluorocarbon species have crucial role to the properties of the fluorocarbon plasma like as the previously described O<sub>2</sub>/Ar plasmas in section 2.3.2.

Fig. 3.3 shows the electron impact collision cross sections for (a) C<sub>4</sub>F<sub>8</sub> and (b) C<sub>2</sub>F<sub>4</sub>. This figure denotes most of the light ion generations by the dissociative ionization have high threshold energies above 10 eV, while the neutral dissociations and attachments which generate relatively heavy fragments of the fluorocarbon have low threshold energies under 7-8 eV [75]. This sensitiveness of decomposition reaction of the fluorocarbon plasma to the colliding energy of the electrons implies that the species of decomposed fragments from the

fluorocarbon molecule plasma is a sensitive function of the EEDF tail. Therefore, the monitoring of b-factor can give information about the reactions in the fluorocarbon plasma volume, and operation as a volume reaction representing PI parameter would be possible. Because the generation rates of reacting radical and ion species in the plasma volume dominantly determines the overall process reaction rates, volume reaction property representing b-factor is the main PI parameter for the development of VM model for C<sub>4</sub>F<sub>8</sub>-oxide etching.

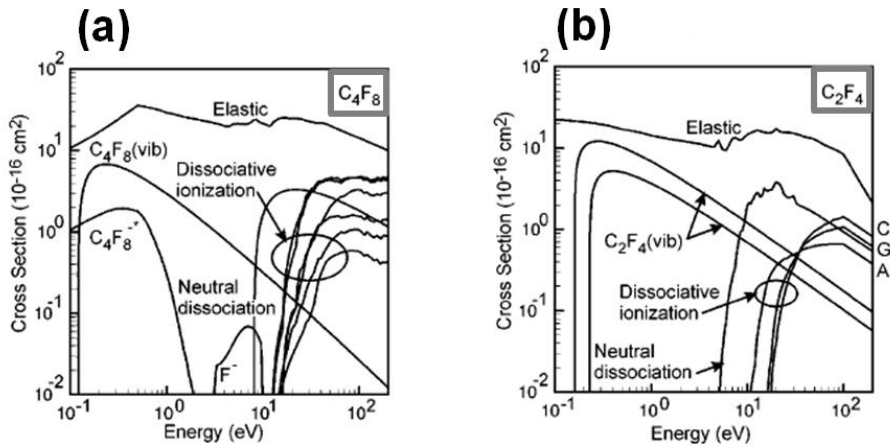


**Figure 3.3** Electron impact cross sections for (a) C<sub>4</sub>F<sub>8</sub> and (b) C<sub>2</sub>F<sub>4</sub>. A, B, C, D, E, F, and G represent C<sub>2</sub>F<sub>4</sub><sup>+</sup>, C<sub>3</sub>F<sub>5</sub><sup>+</sup>, CF<sup>+</sup>, CF<sub>3</sub><sup>+</sup>, CF<sub>2</sub><sup>+</sup>, F<sup>+</sup>, and C<sub>2</sub>F<sub>3</sub><sup>+</sup>, respectively [75].

### 3.2.2 Sheath properties and the first sub PI, q-factor

Sheath is a path that the generated species in the plasma volume are transferred to the surface of the target surface. Simultaneously, sheath is an accelerator of the passing ions by the

electric field of the sheath. Therefore, sheath governs the energy of the ion species transferred on to the reacting surface. This ion bombarding energy is strongly correlated with the physical etch effect as described in the 3.2 [15]. By the continuity of the flux, transferred species onto the substrate surface is proportional to the generation rate of a certain species in the plasma volume. Therefore, volume reaction rate is main component which governs the etch rate dominantly. However, transferred energies onto the surface by the ions also contributes to the physical etching and activation of the reacting surface; thus, enhances the overall etch process reactions. Therefore, the information about the sheath property as a sub PI parameter which represents ion bombarding energy is needed for the development of VM, also. In this section, ion bombarding energy representing q-factor is introduced as a sub PI parameter based on the sheath properties in the electronegative process plasmas.

### **Bohm Criterion and Sheath Property in the Electronegative Plasmas**

Most of the process plasmas applied to the etching or deposition processes include electronegative species as process gases. Halogen atom containing molecules such as fluorocarbon gases ( $C_xF_y$ ), fluorosulfuric gases ( $S_xF_y$ ), and nitron fluorine gases ( $N_xF_y$ ) generate abundant fluorine negative ions, because of high electron affinity of the fluorine atom and low threshold energy of electron attachment reaction of fluorine-series gases in the plasma [15, 78-79]. These fluorine-series gases are widely used as etchants and cleaning gases [75]. Moreover, hydrogen including molecular gases applied to the thin film deposition process, such as  $SiH_4$  and TEOS are also has high electronegativity [25]. To consider this property of the process plasmas, sheath property in the electronegative plasma is analyzed and used as the basis of q-factor introduction.

Electronegativity of these process plasmas is function of the thermal equilibrium state of the

plasma and the partial pressure of electronegative gas species [80]. In the process plasma, perturbation of electronegativity can be occurred even the operating condition fixed cases, by the not perfectly exhausted electronegative cleaning gas molecules, wall contamination effect of the residual electronegative species, the variation of the electron attachment reaction rate, etc. The variation of electronegativity causes the change of Bohm condition, which defines the criterion of the sheath formation condition. To analysis the effect of electronegativity variation to the sheath property, generalized sheath criterion for the electronegative plasma is reviewed according to Amemiya's approach [80].

Well-known ion acoustic speed for Maxwellian EEDF is

$$v_i = (kT_e / M)^{1/2} \quad (3.2)$$

where  $v_i$  is ion acoustic speed,  $k$  is the Boltzmann constant, and  $M$  is ion mass. This is an ion velocity required for the stable sheath formation, and so-called Bohm criterion [80-81]. This can be rewritten with consideration of ion velocity distribution as

$$\langle v_i^{-2} \rangle = \int_{-\infty}^{\infty} \frac{f_i(v)}{v^2} dv = \frac{M}{kT_e} \quad (3.3)$$

where  $f_i(v)$  is the ion velocity distribution and  $\langle \rangle$  means ensemble average of the argument [80]. This can be also derived from the dispersion relation with consideration of electrons, negative ions, and positive ions with the velocity distributions of  $f(v)$ ,  $f_n(v)$ , and  $f_i(v)$ . The generalized dispersion relation in front of the sheath edge is arranged as

$$\omega_{pe}^2 \int_{-\infty}^{\infty} \frac{f(v)}{(\omega - kv)^2} dv + \omega_{pn}^2 \int_{-\infty}^{\infty} \frac{f_n(v)}{(\omega - kv)^2} dv + \omega_{pi}^2 \int_{-\infty}^{\infty} \frac{f_i(v)}{(\omega - kv)^2} dv = 1 \quad (3.4)$$

where  $\omega_{pe}$ ,  $\omega_{pn}$ , and  $\omega_{pi}$  are plasma frequencies of electron, negative ion, and positive ion, respectively. The integral is performed along the Landau's contour avoiding the singularity at  $v = \omega/k$ .  $f(v)$ ,  $f_n(v)$ , and  $f_i(v)$  are calibrated such that the integration from  $-\infty$  to  $+\infty$  is unity.

For steady state ( $\omega=0$ ), Eq. 3.4 is arranged by using  $\langle v_e^2 \rangle$  as

$$\frac{(1-\alpha)}{m} \int_{-\infty}^{\infty} \frac{f_e(v)}{v^2} dv + \frac{\alpha}{M_n} \int_{-\infty}^{\infty} \frac{f_n(v)}{v^2} dv + \frac{1}{M} \int_{-\infty}^{\infty} \frac{f_i(v)}{v^2} dv = \frac{(k\lambda_D)^2}{\{m\langle v_e^2 \rangle/2\}} \quad (3.5)$$

where  $m$ ,  $M$ , and  $M_n$  are masses of electron, positive ion, and negative ion, respectively.  $N_e$ ,  $N_n$ , and  $N_i$  are the density of electron, negative ion, and positive ions.

With the charge neutrality  $N_e + N_n = N_i$ , and the definition of electronegativity  $\alpha = N_n/N_i$ , Eq. 3.5 is arranged into Eq. 3.6 when imaginary part is neglected :

$$\frac{1}{M} \langle v_i^{-2} \rangle = -\frac{(1-\alpha)}{m} \int_{-\infty}^{\infty} \frac{f_e(v)}{v^2} dv - \frac{\alpha}{M_n} \int_{-\infty}^{\infty} \frac{f_n(v)}{v^2} dv + \frac{(k\lambda_D)^2}{\{m\langle v_e^2 \rangle/2\}}. \quad (3.6)$$

Here,  $1/k$  corresponds to the characteristic length, and the characteristic length is given by the sheath thickness much longer than the Debye length  $\lambda_D$ .

Using the simple definition  $\frac{\partial f_e(v)}{\partial v} = -\frac{m}{2} F(E)$  and  $E = \frac{mv^2}{2}$  into the Eq. 3.5,

dispersion relation in Eq. 3.6 is arranged into

$$\frac{1}{M} \langle v_i^{-2} \rangle = (1-\alpha) \int_{-\infty}^{\infty} \frac{F(E)}{2E} dE + \alpha \int_{-\infty}^{\infty} \frac{F_n(E)}{2E} dE \quad . \quad (3.7)$$

where a similar expression is used for negative ion's velocity distribution  $f_n(v)$  and energy distribution  $F_n(E)$ .

In front of the sheath, positive ions at the sheath edge have a velocity distribution with a narrow velocity width [82], thus this approximation is possible :

$$\langle v_i^{-2} \rangle^{-1} = \langle v_i^2 \rangle \quad (3.8)$$

According to this relation, potential at the sheath edge with electronegativity  $\alpha$  in Eq. 3.7 can be expressed into :

$$eV_s = \frac{1}{2} \left[ (1-\alpha) \int_{-\infty}^{\infty} \frac{F(E)}{2E} dE + \alpha \int_{-\infty}^{\infty} \frac{F_n(E)}{2E} dE \right]^{-1} \quad (3.9)$$

where  $V_s$  is the sheath edge potential and  $e$  is charge of one electron. With adoption of arbitrary form of the EEDF into the Eq. 3.9, the sheath edge potential as a Bohm criterion in the electronegative plasma can be generalized as

$$eV_s = \frac{1}{2} \left[ (1-\alpha) \frac{\Gamma(1/2b)\Gamma(5/2b)}{2\langle E \rangle [\Gamma(3/2b)]^2} + \frac{\alpha}{kT_n} \right]^{-1} \quad (3.10)$$

where

$$\alpha = \frac{\alpha_0 \delta_n}{\delta_e (1 - \alpha_0) + \alpha_0 \delta_n}, \quad (3.11)$$

$$\delta_e = \frac{N_e}{N_{e0}} = 2 \int_{v_s}^{\infty} \frac{vf(v)dv}{\sqrt{v^2 - 2eV/m}} = \int_{eV_s}^{\infty} \sqrt{1 - \frac{eV_s}{E}} F(E) dE, \quad (3.12)$$

and

$$\delta_n = \frac{N_n}{N_{n0}} = \exp(-eV_s / kT_n). \quad (3.13)$$

The Eqs. 3.10 - 3.13 are nonlinearly coupled to the each other; thus, calculation of the direct solution of the  $V_s$  is impossible [80]. Eq. 3.10 shows that the Bohm condition of the electronegative plasma is coupled function of the electronegativity and the thermal equilibrium property of the plasma. Electronegativity of the plasma is also a function of the electron attachment and dissociative attachment reaction rate, which is governed by the EEDF of the plasma. At the same time, the thermal equilibrium state of the plasma is also changed by the electron loss and energy loss of the high energy electrons by the attachment and dissociative attachment, respectively. Therefore, the sheath formation condition in the electronegative plasma is influenced by the volume reaction properties of the bulk plasma represented by the main PI parameter  $b$ . The ion bombarding energy of the electronegative process plasma depends on the main PI parameter, and this implies that the developing sheath

property representing parameter  $q$  is subordinate to the volume reactions in the plasma.

Because the described nonlinearly coupled correlations of Eqs. 3.10 - 3.13, Allen *et al.* approached with one parameter fixed assumption to calculate the  $V_s$  for a certain condition of the plasma [83-88]. They analyzed the correlation between the sheath edge potential and electronegativity for the thermal equilibrium property fixed conditions. At the given plasma temperature and type of EEDF, the  $eV_s$  is arranged into the only function of the electronegativity. However, this approach is confronted with “multi-solution paradox” of the electronegative sheath edge potential for one value of electronegativity at the thermal equilibrium property  $kT_e/kT_n > 5 + \sqrt{24}$  condition [84]. At the multi solution occurred region, this multi-solution paradox causes about 50 % of uncertainty of the sheath edge potential.

For the generally applied process plasmas, 50 % of potential error is quantity about 1 – 3 eV. Because the bonding energy between the atoms composing the reacting solid substrate is about 2 – 3 eV, this 1 – 3 eV uncertainty of the ion bombarding energy is considerable to apply for the sheath property monitoring of the process plasma. Especially, this becomes more serious for the processes performed without the bias power.

To adopt the information about the sheath properties in the electronegative plasma into the VM model, solution to this uncertainty of sheath edge potential caused by the multi-solution paradox is needed. This problem is caused by the separated consideration of the thermal equilibrium property and the electronegativity of the plasma for the evaluation of the sheath edge potential. That is to say, the  $eV_s$  is described on the 2-D space of  $eV_s - \alpha$  or  $eV_s - kT_e$ , while the  $eV_s$  is a function of  $\alpha$  and  $kT_e$  lie on 3-D space. Visualization of this  $eV_s$  on the 3-D space is shown in Fig. 3.4. According to the sheath edge potential expressed in Eq. 3.10, correlation between electronegativity, thermal property, and sheath edge potential are described in the 3-

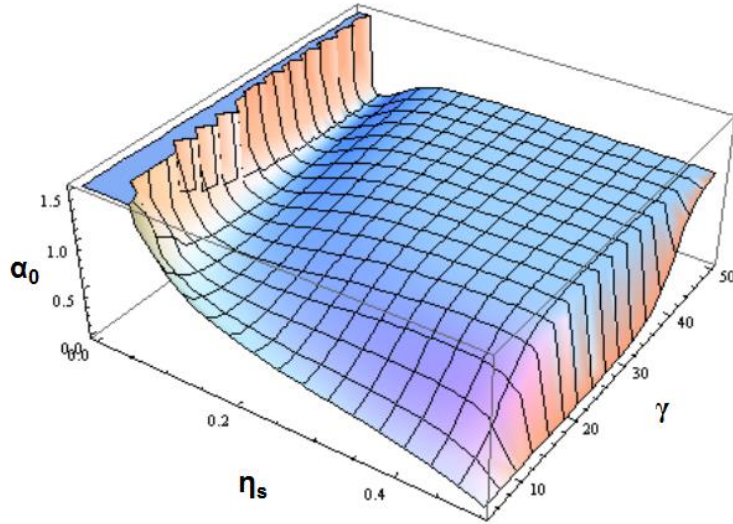
dimensional space of electronegativity( $\alpha_0$ ), normalized presheath potential ( $\eta_s = \frac{eV_s}{kT_{e,eff}}$ ),

and normalized electron temperature ( $\gamma = \frac{kT_{e,eff}}{kT_n}$ ) axes. For the visualization of their

correlation as one curved surface, type of EEDF is considered as Maxwellian distribution as an example. To describe the case of arbitrary shaped EEDF, 4-D space description is required. The curved lines in 2-D space of  $eV_s - \alpha$  analyzed by the Amemiya and Allen [80, 84] are unrolled as curved surface in 3-D space of  $\eta - \alpha - \gamma$  as shown in Fig. 3.4.

Result described in Fig. 3.4 do not give any constraint to the analysis of the sheath property in the electronegative plasma, and the preferred variation trend of the sheath edge potential with varying thermal equilibrium property and the electronegativity. Most probable path of the sheath edge potential variation would exist on the curved surface, and this is governed by the thermodynamic stability of the state. To apply this idea onto the Bohm criterion of the electronegative plasma, molecular chaos is introduced onto the Boltzmann function [89-93].

(a)



(b)

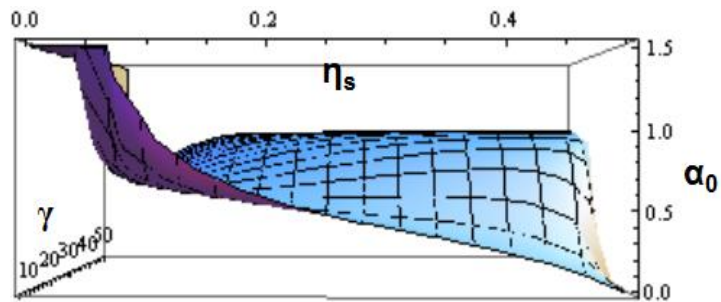


**Figure 3.4** (a) 3-dimensional plot of the sheath edge potential in the electronegative plasma as a function of the electronegativity and plasma temperature, (b) side view of the 3-dimensional plot which represents the 2-dimensional plot of the electronegativity vs. sheath edge potential.

For macroscopic system, Boltzmann entropy is generally expressed into [94]

$$S(W) = S(e) \ln W \quad (3.14)$$

where  $S$  is the entropy,  $W$  is the degree of disorder, and  $e$  is a natural constant. With introduction of the probability  $P(A)$  for microscopic system analysis with  $A$  is observational state, and  $A_n$  which is nothing but the total number of microscopic complexions compatible with the observation state  $A_n$  in the definition of Boltzmann entropy, by Randon-Nikodym theorem, we may write [94]

$$P(A) = \sum \rho(A_n) W(A_n). \quad (3.15)$$

where

$$\rho(A_n) = \frac{P(A_n)}{W(A_n)}, \quad n = 0, 1, 2, \dots \quad (3.16)$$

This is analogous to the coarse-grained density of microstates defined over the phase - space of the usual definition of Gibbs entropy. Then, we can define Boltzmann-Gibbs entropy for the microscopic system as:

$$\bar{S} = - \sum P(A_n) \ln \frac{P(A_n)}{W(A_n)}. \quad (3.17)$$

On the other hand, with assumption of  $S(t) = -kH(t)$ , Boltzmann function  $H(t)$  can be written

as [16]

$$H(t) = \iiint_V d^3\vec{r} \iiint_{\infty} d^3\vec{v} F(t, \vec{r}, \vec{v}) \ln F(t, \vec{r}, \vec{v}). \quad (3.18)$$

Then, the 3<sup>rd</sup> law of thermodynamics can be expressed into

$$\frac{dS(t)}{dt} \geq 0 \quad \Rightarrow \quad \frac{dH(t)}{dt} \leq 0. \quad (3.19)$$

By the substitution of Eq. 3.18 into the Eq. 3.19, one equation known as the H-theorem is obtained [16].

$$\frac{dH(t)}{dt} = \frac{1}{4} \iiint_V d^3\vec{r} \iiint_{\infty} d^3\vec{v}_2 \int_0^{2\pi} d\varepsilon \int_0^{\pi} d\chi \sin \chi S g \ln \left( \frac{FF_2}{F'F'_2} \right) [F'F'_2 - FF_2] \quad (3.20)$$

Here the  $\varepsilon$ ,  $\chi$ ,  $S$ , and  $g$  are the geometric parameters at the moment of collision described by Gombosi [16]. Definition of  $F$  is same with the description in section 2.3.1. To obtain the thermodynamically most probable Bohm criterion formation condition on the curved surface of Fig. 3.4,  $F'F'_2 - FF_2$  should be zero. Here,  $F$  is dealt as the EEDF,  $F_2$  is neutral energy distribution function, and primes on the distribution functions denote the state after collision. For example, if one assumes Maxwellian EEDF before the collision,  $F$  and  $F_2$  can be written as

$$F = \frac{2\sqrt{E}n_e}{\sqrt{\pi}(kT_e)^{3/2}} \exp(-E/kT_e) \quad (3.21)$$

and

$$F_2 = \frac{2\sqrt{E}n_n}{\sqrt{\pi}(kT_n)^{3/2}} \exp(-E/kT_n). \quad (3.22)$$

After the collision,  $F$  and  $F_2$  become

$$F' = \frac{2\sqrt{E}n'_e}{\sqrt{\pi}(kT'_e)^{3/2}} \exp(-E/kT'_e) \quad (3.23)$$

and

$$F'_2 = \frac{2\sqrt{E}n'_n}{\sqrt{\pi}(kT'_n)^{3/2}} \exp(-E/kT'_n), \quad (3.24)$$

respectively.

By the definition of quasi-neutrality in the electronegative plasma, the density of the negative ion can be written as

$$n_n = \frac{\alpha_0}{1 - \alpha_0} n_e. \quad (3.25)$$

Eqs. 3.21-3.25 are combined with the Eq. 3.20, and arranged as

$$\begin{aligned} & \frac{n_e^2}{(kT_e kT_n)^{3/2}} \frac{\alpha_0}{1-\alpha_0} \exp(-E/kT_e) \exp(-E/kT_n) \\ &= \frac{n_e'^2}{(kT_e' kT_n')^{3/2}} \frac{\alpha_0'}{1-\alpha_0'} \exp(-E/kT_e') \exp(-E/kT_n') = \text{const} \end{aligned} \quad (3.26)$$

with the assumption that the temperature of the neutral gas species is constant, the Eq. (3.26) is simplified as

$$\frac{1}{\alpha_0} = 1 + \frac{n_e^2}{C (kT_n)^3 \gamma^{3/2}} \exp\left(-\gamma \left(1 + \frac{1}{\gamma}\right)\right) \quad (3.27)$$

where  $C$  is coefficient determined by the electron temperature before the collision is occurred. For the convenience of the calculation,  $C$  is defined as

$$\frac{n_e^2 \left(\frac{\alpha_0}{1-\alpha_0}\right)}{\gamma^{3/2} (kT_n)^{3/2}} \int_0^\infty \exp\left(-\frac{E}{kT_n} \left(1 + \frac{1}{\gamma}\right)\right) dE = C. \quad (3.28)$$

This correlation becomes the constraint on the 3-D curved surface of the  $\eta - \alpha - \gamma$  to determine the solution. By the setting of the initial temperature, the value of  $C/n_e n_n$  is determined and curved surface representing Eq. 3.27 can be drawn in the 3-D space. This curve is crossed with the curve shown in Fig.3.4, and the cross curved line of two curved surfaces becomes the solution as shown in Fig. 3.5. This result is an example for  $C/n_e n_n = 0.40$

case, corresponds to the initial  $T_{e,eff} = 5$  eV plasma. For thermal equilibrium property and the electronegativity of the plasma varying cases, the variation of sheath edge potential can be analyzed using the Fig. 3.5, and the multi-solution problem in the 2-D space analysis is solved.

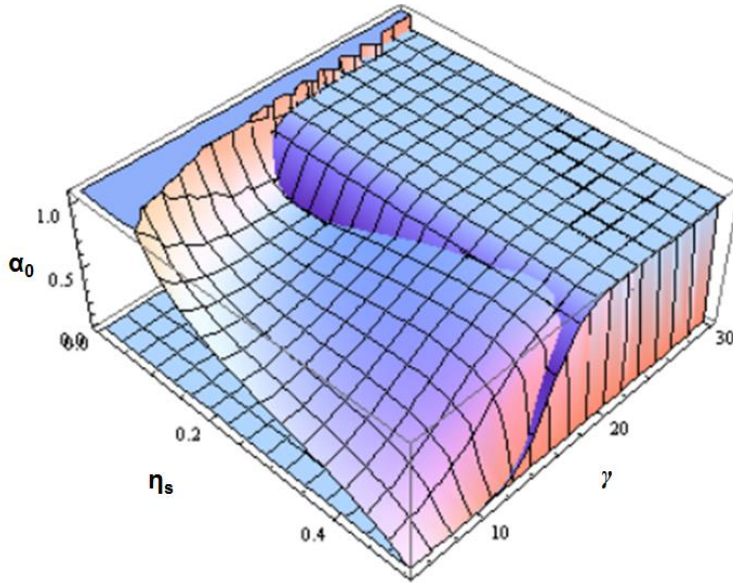


**Figure 3.5** thermodynamical constraint considered solution of the sheath edge potential as a function of the electronegativity and plasma temperature in 3-dimensional space of  $\eta - \alpha - \gamma$ .

Figure 3.6 shows an example of the solution of Allen's and Seolhye Park's for  $C/n_e n_i = 0.2$  case. Allen's solution lies on the flat surface with  $\gamma$ - fixed condition, while the suggested solution by the result of Fig. 3.5 passes through that plane. Therefore, suggested solution of the Bohm criterion in the electronegative plasma in this section implies that the property of the sheath is strongly correlated with the volume reaction property of the plasma, especially on the thermal equilibrium state. To use the information about the sheath property efficiently onto the VM model development, main PI parameter  $b$ , the information about the EEDF in the bulk volume of the plasma should be considered, also.

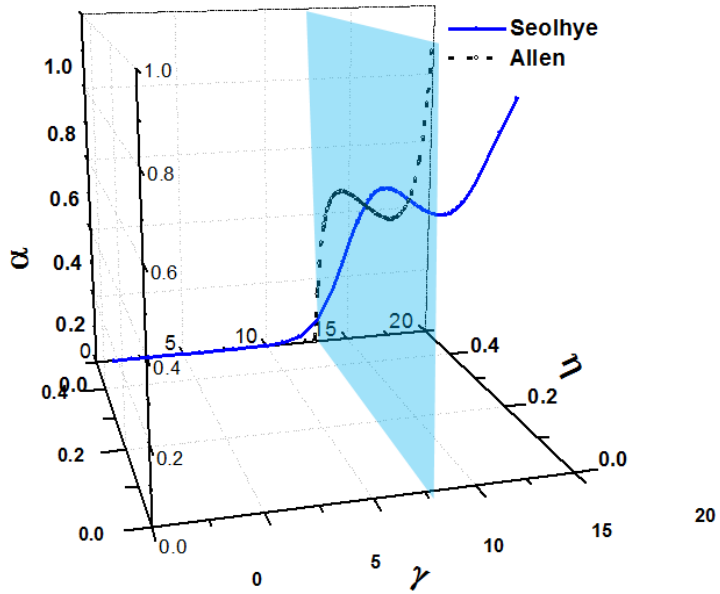


**Figure 3.6** Example of the solution of the sheath edge potential in the electronegative plasma at  $C/n_e n_n = 0.2$  condition for Allen's and Seolhye's in the 3-dimensional space of  $\eta - \alpha - \gamma$ .

### Ion Bombarding Energy Representing PI parameter $q$ in the Fluorocarbon Plasmas

According to the analysis on the sheath edge potential for electronegative plasma, ion bombarding energy monitoring PI parameter  $q$  is introduced to monitor the fluorocarbon plasma sheath property. Eqs. 3.10 and 3.27 give the simplified correlation of

$$\frac{1}{eV_s} \sim \frac{\alpha_0 \gamma}{b} \tag{3.29}$$

for  $0.01 < C/n_e n_n < 0.8$  region. This corresponds to the range of  $0.1 \text{ eV} < T_{e,eff} < 20 \text{ eV}$ , thus application to the generally used process plasmas has no problem. PI parameter  $q$  is defined as

$$q = \frac{\alpha_0 \gamma}{b} \quad (3.30)$$

and monitored by using the selected sensor, OES signals. To monitor the  $q$ , electronegativity  $\alpha_0$  representing sensing variable and the thermal property  $\gamma$  representing signals are required. For fluorine-series gas aided plasmas like as the fluorocarbon, generation of the negative ion is occurred after dissociation of the molecules except the direct attachment on to the feeding gas [79]. Therefore, the electronegativity of the F-series plasma is a function of the F radical density [75, 79]. Most of the process plasmas facing the Si substrate, and F radicals are react with Si and generates  $\text{SiF}^*$  with high probability [95]. Therefore, to represent the  $\alpha_0$ , emission line of  $\text{SiF}^*$  - 439 nm is selected. And to represent  $\gamma$ , reciprocal intensity of Ar I – 811 nm is selected. The b-factor is used the monitored value as the main PI parameter. Then, the correlation with  $q$  is arranged into

$$\begin{aligned} q &= \frac{(I_{\text{SiF}^*-439\text{nm}})}{(b - \text{factor})(I_{\text{ArI}-811\text{nm}})} \\ &= \frac{1}{(b - \text{factor})} \frac{n_{\text{SiF}}}{n_e} \frac{n_e}{n_{\text{Ar},0}} \frac{X_{\text{SiF}^*}^{\text{exc}}(T_{e,eff}, b)}{X_{\text{Ar},2p}^{\text{exc}}(T_{e,eff}, b)} \end{aligned} \quad (3.31)$$

where  $X^{\text{exc}}$  follows the definition of Eq. 2.24. By the substitution of excitation and ionization rate coefficient into the Eq. 3.31, q-factor composed by the measured OES sensing variables are arranged into

$$q \sim \frac{1}{(b-factor)} \frac{n_{SiF}}{n_e} \frac{n_{Ar,0} X_{Ar}^{iz} (\varepsilon_{th} = 15.75 \text{ eV})}{n_{Ar,0}} \frac{X_{SiF^*}^{exc} (\varepsilon_{th} \sim 1 \text{ eV})}{X_{Ar,2p}^{exc} (\varepsilon_{th} = 13 \text{ eV})} \quad (3.32)$$

$$\sim \frac{\alpha T_{e,eff}}{(b-factor)}$$

Eq. 3.32 shows selected signals to monitor the sheath edge potential as a function of the thermal equilibrium property and the electronegativity is well-agreed with the initial definition of the q-factor, Eq. 3.30. Therefore, the introduced q-factor contains the information about the sheath property of the electronegative plasma efficiently, and applicable to the development of VM as a sub PI parameter which depends on the main PI parameter.

### 3.2.3 Surface reactions and the second sub PI, passivation species

Reactive radical or ion species delivered on the substrate surface react with the solid materials. At first, when the particle is arrived on to the surface of the solid, this particle stuck on the surface with probability of the sticking coefficient between the particle and surface material. Arrived particle looks for the site with the lowest Gibbs free energy by the diffusion on the surface [96]. Therefore, increase of the surface diffusion coefficient causes the faster reaction rate on the site of the solid surface. These implies that the increase of surface diffusion coefficient and sticking coefficient lead the higher etch rate by the increase of chemical reaction rate. The surface diffusion coefficient is defined as [16, 26]

$$D_s = \exp\left(-E_s / kT_{surf}\right) \quad (3.33)$$

where  $E_s$  is the surface binding energy of the solid material, and the  $T_{surf}$  is the surface temperature. And the surface sticking coefficient is also a function of  $T_{surf}$  as [97-98]:

$$s \propto \exp\left(-E_b / kT_{surf}\right) \quad (3.34)$$

where  $E_b$  is surface activation energy for the sticking. Both diffusion and sticking coefficients are increased with the increase of surface temperature; thus, the monitoring of the surface temperature and the species of arrived radical species is very important to consider the reaction properties on the surface. The variation trends of the surface diffusion coefficient and sticking coefficient can be monitored by using the EES data,  $T_{surf}$ .

In addition, charge exchange reactions of  $\text{Ar}^+$  and  $\text{CO}^+$  with heavy fluorocarbon radicals are important reactions for the surface reaction properties [75]. This is the largest loss channel of  $\text{Ar}^+$  and  $\text{CO}^+$ , which generates heavy radicals by the charge exchange reaction. Therefore, the density of  $\text{Ar}^+$  and  $\text{CO}^+$  in the fluorocarbon plasma volume determines is proportional to the generation rate of polymer composing heavy radicals [75, 99]. Heavy fluorocarbon radicals contribute to the generation of the polymer deposition on the reacting surface, thus this charge exchange reaction acts as the passivation effect on the etching reaction. This implies that the passivation effect of the etching reaction in the fluorocarbon plasma can be monitored by using the Ar II intensity, CO intensity, and CF<sub>2</sub> intensity of the OES signals. Therefore, these 3 emission lines coupled with Eqs. 3.33 and 3.34 are defined as the 2<sup>nd</sup> sub PI parameter, which contains the information about the etch pattern passivating effect on the surface.

### 3.3 Construction of VM components based on the PI parameters

To apply the information about the reaction rates in the process plasma into the VM model development efficiently, volume, sheath, and surface reaction mechanism representing PI parameters are introduced and monitoring signals are selected. The utility of these selected parameters as the sensing variables are tested by adoption onto the PCR based VM model, and combined based on the reaction mechanism.

To analyze the role of the PC (Principal Component)s of the VM model, PCA as a typical statistical method is used to compose the variable set. PCA is a well-known automatic dimension reduction method with simple algorithm and widely used in statistical approaches for development of VM [8]. Reduced optical and EES signals introduced in section 3.1 are used to the statistical analysis, and PCA was accompanied to construct near-optimum variable set.

From the PCA, new independent variables are generated by the linear combination of 79 variables into 3 variables. These 3 PCs contains 91 % of total variance as shown in Fig. 3.7. Cumulated variance fraction is increased with the number of PCs, but saturated above the 3<sup>rd</sup> PC. 3 PCs contain the enough amount of the statistical information according to the Fig. 3.7, thus we applied the only 3 PCs to the analysis of the PC properties and regression for the VM.

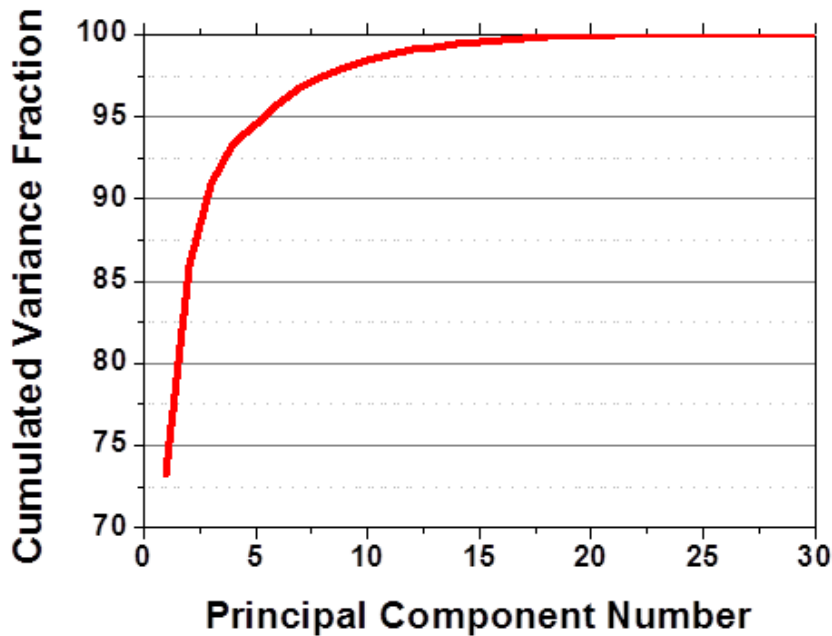
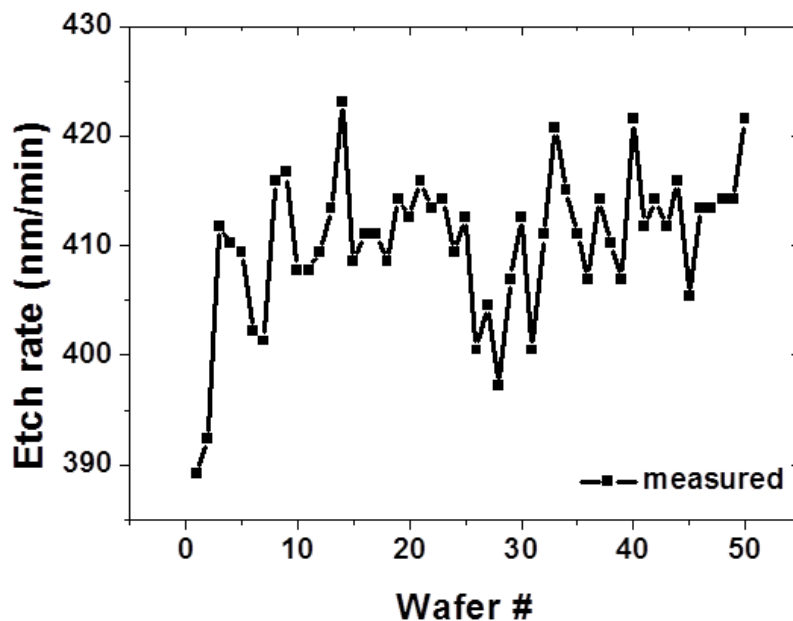


**Figure 3.7** Cumulated variance fraction with increasing number of principal components consisted by the sensing variables without the consideration of the PI parameters.

Because one PC is linearly independent to the other PC, key properties can be understood by analyzing the SVs which makes up each of PCs : (1) The 1<sup>st</sup> PC was highly correlated with Ar I, Ar II, CF<sub>2</sub>, C<sub>2</sub>, and F I intensities of OES signal. Here the Ar I and Ar II lines are strongly correlated with the thermal equilibrium property of the plasma. These lines can be used to monitor the main PI parameter, b-factor. CF<sub>2</sub>, C<sub>2</sub>, and F signals denote the dissociated species from the C<sub>4</sub>F<sub>8</sub> process gas which are governed by the EEDF. Therefore, the 1<sup>st</sup> PC represents the chemical etching reactions in the plasma volume. (2) The 2<sup>nd</sup> PC is composed by power matching condition, bias V<sub>pp</sub>, Ar I, CF<sub>2</sub>, CN, and T<sub>bm</sub>. Power matching condition is directly correlated with the absorbed power of the plasma, which determines the density and temperature of the plasma. Ar I intensity represents the density of electrons energies above

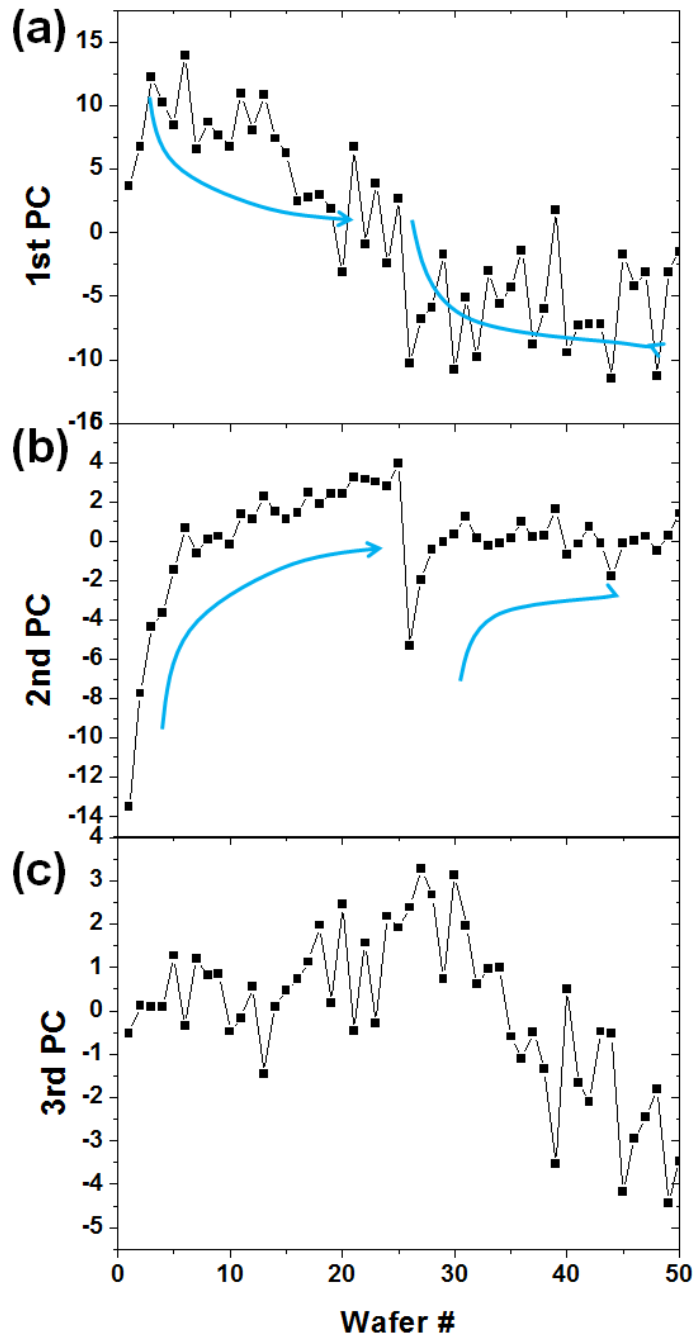
near 13 eV, thus strongly correlated with the heating property of the plasma. The 2<sup>nd</sup> PC can be classified as the physical properties representing term of the reactions in the plasma volume which varies according to the heating and power matching condition. (3) The last 3<sup>rd</sup> PC is composed by the power matching condition, CF<sub>2</sub>, CO, Ar II, F I, T<sub>top</sub>, biasV<sub>pp</sub>, O I, and pressure. BiasV<sub>pp</sub> is correlated with the sheath potential and ion acceleration, and F I, and O I signals are the emission intensities from the electronegative species which influence to the sheath properties in the electronegative plasmas. Moreover, Ar II and CO intensities are correlated with the charge exchange reactions contribute to the passivation of the etching reaction. Therefore, the 3<sup>rd</sup> PC is correlated with electronegative sheath – surface reactions. Based on this analysis of the PCs, contribution of the each of reaction mechanisms on the determination of the etch rate is evaluated.

Fig. 3.8 shows the variation of etch rates for 50 wafers processed in the experimental system described in section 3.1. Average of the etch rate for 50 wafers is 410.36 nm/min and their standard deviation is 6.74 nm/min.



**Figure 3.8** The variation of etch rates for 50 wafers measured by V-SEM images.

Variation of each of the PCs which represents chemical volume reaction, physical volume reaction, and sheath-surface reactions during the etching process of 50 wafers is shown in Fig. 3.9. As shown in Fig. 3.9 (a), the 1<sup>st</sup> PC which represents chemical reaction effect is inversely correlated with the etch rate variation trend. The 2<sup>nd</sup> PC of Fig. 3.9 (b) varies with small range oscillations of the etch rates, but the overall variation trend is strongly correlated with the measured etch rate expressed in Fig. 3.8. The 3<sup>rd</sup> PC in Fig. 3.9 (c) oscillates and describes the detailed variation trend of the etch rate.



**Figure 3.9** The variation of the PCs during the process of 50 wafers : (a) the 1<sup>st</sup> PC, (b) the 2<sup>nd</sup> PC, and (c) the 3<sup>rd</sup> PC.

Using these 3 PCs obtained by the PCA, linear regression is performed to predict etch rate. Weightings of the 1<sup>st</sup>, 2<sup>nd</sup>, and 3<sup>rd</sup> PCs are determined as -0.1231, +1.3470, and -0.7204, respectively. These weightings imply that the physical property of the plasma volume reaction and the electronegative sheath property are important factors to the oxide etching process mechanism. The regression result can be used as a statistical VM results after normalization and scaling, and the VM results are shown in Fig. 3.10. The correlation coefficient between the measured etch rate and VM result was  $R^2 = 38.8 \%$ , and the prediction error was 0.94 %. Generally required number of data set is about 800 to obtain statistically guaranteed accuracy in this case [11], which is difficult to satisfy in mass production system. The number of delivered data set in this analysis were the only 50 sets, therefore the VM results show quite low accuracy, caused by the fundamental limitation of the PCR based VM performance for insufficient number of data set provided cases [11-13]. Because of large number of sensing variables, this can be a common and practical problem to development of the plasma-assisted process VM. This result implies that good information containing parameter should be additionally applied to the VM model to achieve better performance for the insufficient data set provided case.

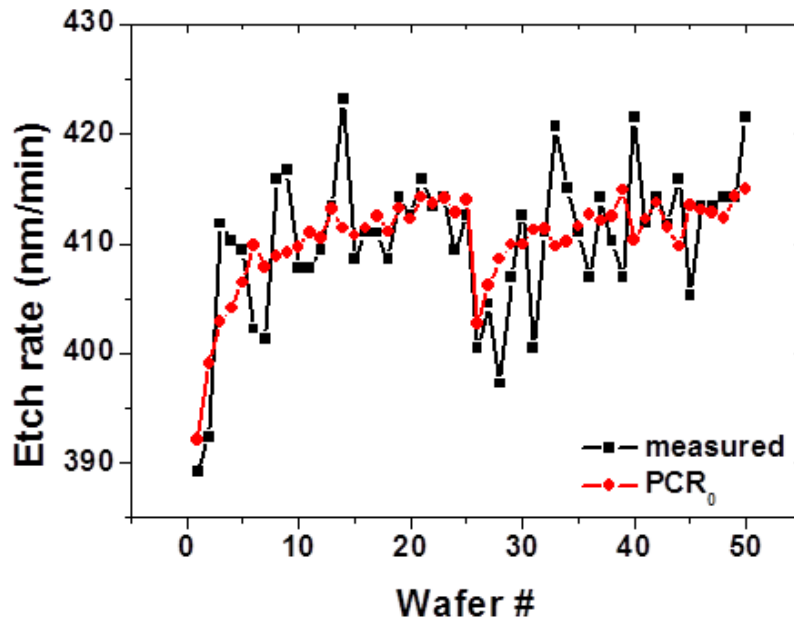


**Figure 3.10** The comparison of the PCR<sub>0</sub> based VM result for the prediction of etch rate without the consideration about the PI parameters and the measured etch rate for 50 wafers.

### 3.3.1 Chemical etching term

As described in the previously, the 1<sup>st</sup> PC represents the chemical reactions in the plasma volume. Chemical reaction representing parameter was composed by the OES signals of the argon and dissociated species from the C4F8. Volume reaction mechanism analysis performed in section 3.2.1 infers that this chemical reaction property in the plasma volume would have strong correlation with the thermal equilibrium state of the plasma. Actually, Ar I and Ar II lines applicable to the b-factor monitoring were the variables composing the 1<sup>st</sup> PC. And the signals of the other fragments of fluorocarbon were also the variables governed by the EEEDF.

To contain the information about this chemical reaction efficiently to the VM, the main PI parameter  $b$  is included into the composition of the 1<sup>st</sup> PC. The advanced PCR result with addition of b-factor designated as  $PCR_b$  is shown in Fig. 3.11. The correlation coefficient between the measured etch rate and VM result was  $R^2 = 57.2\%$ , and the prediction error was  $0.82\%$ . By the application of main PI parameter, about  $20\%$  of correlation coefficient is progressed compared to the basic  $PCR_0$ .

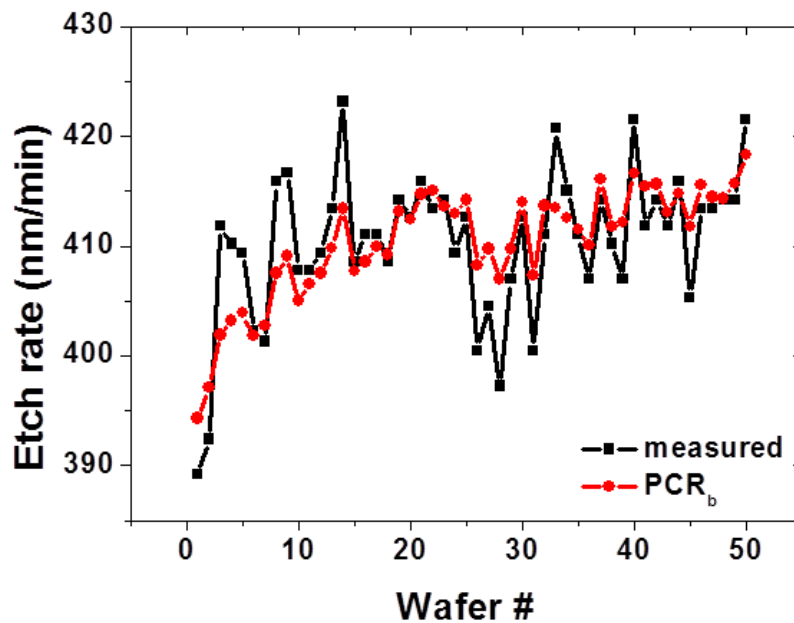


**Figure 3.11** The comparison of the  $PCR_b$  based VM result with the consideration of the PI parameter  $b$  and the measured etch rate for 50 wafers.

Nevertheless main PI parameter has adopted, the performance of the  $PCR_b$  could not satisfy the required accuracy of the industry (error  $< 0.4\%$ ) [3]. Reaction rate in the plasma can be written generally as [15]

$$\frac{\partial N(\vec{r}, t)}{\partial t} = \int f(\vec{v}, \vec{r}, t) |\vec{v}| \sigma_{ij}(v) N_j N_i d^3v. \quad (3.35)$$

For the chemical reactions in the plasma, the reaction rate of Eq. 3.35 can be classified into the chemical etch contributing species generation reaction and chemical etch disturbing species generation rate. These reactions are caused by the generation of the light ion and radicals for etch contributing term, and the generation of heavy polymer for etch disturbing term, respectively. Each of the reaction rates can be written as

$$R_{\text{Chem.etch}} = \sum_{\text{CxFy}} \int f(\vec{v}, \vec{r}, t) |\vec{v}| \sigma_{\substack{\text{diss-iz to} \\ \text{light species}}}(v) N_{\text{CxFy}} N_e d^3v \quad (3.36)$$

and

$$R_{\text{passiv.polymer}} = \sum_{\text{CxFy}} \int f(\vec{v}, \vec{r}, t) |\vec{v}| \sigma_{\substack{\text{diss to} \\ \text{heavy species}}}(v) N_{\text{CxFy}} N_e d^3v. \quad (3.37)$$

According to Matsuda *et al.*, etching process reaction rate can be expressed as similarly with the deposition process reaction rate [100]:

$$ER = \sum_{j,l} h_{j,l} n_{\text{target}} s_{j,l} D_{j,l} \nabla N_{j,l} = n_{\text{target}} \left( \pm \sum_j k_j s_j D_j \nabla N_j + \sum_l \kappa_l \Gamma_l \right). \quad (3.38)$$

where  $h$  is the effective bond length between target Si atoms in the film,  $k_j$  is the effective bond length to the new chemical bonding,  $\kappa_l$  is the effective bond length to the physical damage,

$n_{target}$  is the number of target Si atoms,  $s_{j,l}$  is the sticking coefficient,  $D_{j,l}$  is the diffusion coefficient,  $N_{j,l}$  is number density of the incident radical or ion, and  $\Gamma_j$  is flux of the incident ion. Chemical etching effect denotes the sufficient supply of the  $N_{j,p}$  where  $N_{j,l}$  is

$$N_j \propto R_j = n_j n_e \int_{E_{thr}}^{\infty} f(\varepsilon) \sigma_{ej}(\varepsilon) \sqrt{\varepsilon/2m_e} d\varepsilon . \quad (3.39)$$

The value of  $N_j$  is determined by the sum of Eqs. 3.36 and 3.37. Therefore, the information about the other parameters at the front of  $N_j$  in the first term and second term of the right hand side in Eq. 3.38 are not contained in the PCR<sub>b</sub>. To apply the overall influential information to the process result into the VM, the information about the reaction mechanisms induced from the 2<sup>nd</sup> and 3<sup>rd</sup> PCs should be included.

### 3.3.2 Physical etching term

Generated radical and ion species in the process plasma volume are transported onto the target substrate, and this surface reaction is etching process. The 3<sup>rd</sup> PC composing sensing parameters are correlated with the transport of the reacting species from the plasma volume to the substrate surface as described. Particles and energies are transferred through the sheath of the plasma, therefore the surface etching reaction rates are sensitive to the physical properties of the sheath as discussed in section 3.2.2. To include the information about process plasma sheath property into the VM model, the 1<sup>st</sup> sub PI parameter,  $q$  is applied onto the PCR to replace the 3<sup>rd</sup> PC. The effect of the  $q$ -factor into the VM corresponds to the addition of Eq. 3.40 to the Eq. 3.35.

$$R_{\text{phys.etch}} = (\text{physical etch by ion bombarding}) = C(q) \quad (3.40)$$

where  $C$  is the surface activating coefficient as a function of  $q$ .

Figure 3.12 is the VM result with adoption of  $q$  on the previous version of PCR. We denote that the  $\text{PCR}_{b,q}$  means the PCR based VM result with adoption of  $b$  and  $q$  instead of 1<sup>st</sup> and 3<sup>rd</sup> PCs, respectively. The performance of VM was enhanced as the correlation coefficient of  $R^2 = 70.0\%$  between the measured and predicted etch rates. The prediction error was 0.72 %. By the application of the monitored physical properties of the process plasmas, performance of the PCR based VM is noticeably enhanced eventhough statistically insufficient number of data set was provided. However, with adoption of 2 PI parameters onto the VM model, industrial requirements of the accuracy (error < 0.4 %) could not be satisfied.

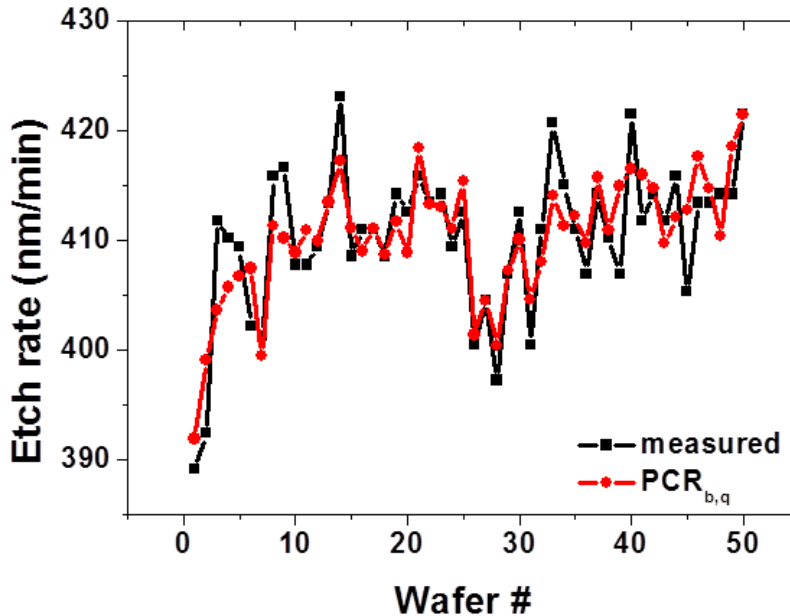


**Figure 3.12** The comparison of the  $\text{PCR}_{b,q}$  based VM result with the consideration of the PI parameters  $b$  and  $q$ , and the measured etch rate for 50 wafers.

### 3.3.3 Surface passivation term

As shown in Figure 3.12, the fluctuation range of the predicted etch rates is narrower than measured etch rates. Etch rate prediction of 12 wafers of total 50 wafers are failed to satisfy the requirement of industry (error < 0.4 %). 92 % of these prediction failed wafers also had abnormal etching patterns of bowing CD (Critical Dimension), top CD, etc. PI parameters of  $b$  and  $q$  were based on the assumption of homogeneous plasma and uniform flux; thus, the information about nonuniform-realistic phenomena were not included in the  $PCR_{b,q}$ .

According to Kushner *et al.*, heavy particle collision reactions of  $Ar^+$ ,  $CF_2^+$ ,  $O$ ,  $F$ , and  $CO^+$  are strongly correlated with the passivation of the etching reaction as discussed in section 3.2.3 [75]. Etched pattern profile is deformed by the passivation, and deposition of the polymer is enhanced when the surface temperature is low. This effect is not included in the  $q$  which replaced the 3<sup>rd</sup> PC. To consider the information about the passivation reaction on the surface,  $Ar^+$ ,  $CF_2$ ,  $O$ ,  $F$ , and  $CO$  emission intensities which are corresponded to the 2<sup>nd</sup> sub PI parameter should be included into the VM model according to the structure of Eq.3.38 to represent the  $s_{j,l}$  and  $D_{j,l}$ . This reaction mechanism of surface passivation can be considered as

$$R_{\text{passiv.CX}} = -C(T_{\text{surf}}) \sum_{Ar^+, CO^+} \int f(\vec{v}, \vec{r}, t) |\vec{v}| \sigma_{CX}(v) N_{CxFy} N_{Ar^+, CO^+} d^3v. \quad (3.41)$$

where  $C(T_{\text{surf}})$  represents the effect of the  $s_{j,l}$  and  $D_{j,l}$ . This result implies that the reaction mechanism based PI combination model is needed to obtain high-performance VM.

### 3.4 Performance of PI-VM model for etch rate prediction

#### 3.4.1 Organization of $r_{\text{etch}}$ -factor

To combine the monitored PI parameters according to the reaction mechanism described as Eq. 3.38,  $r_{\text{etch}}$ -factor which represents the reaction rates in the process plasma is introduced. According to Kushner *et al.*, each of the terms composing the chemical etching reaction and physical etching reaction with the forms of Eq. 3.35 can be combined into

$$\left. \frac{\partial N(\vec{r}, t)}{\partial t} \right|_{Cij} = \sum_{i,j} (\pm) \int f(\vec{v}, \vec{r}, t) |\vec{v}| \sigma_{ij}(v) N_j N_i d^3v. \quad (3.42)$$

Overall reactions occurred in the process reactor can be classified into the “etch contributing reactions” and “etch disturbing reactions”. Chemical and physical etch reactions are etch contributing reactions, and the passivation effects by the charge exchange reaction and the generation of heavy fluorocarbon materials and deposition onto the low temperature surface are the etch disturbing reactions. Each of the reactions was described as the Eqs. 3.36, 3.37, 3.40, and 3.41, and these are combined into the Eq. 3.42 as the terms of

$$R_{\text{Chem.etch}} = +C_1 \sum_{\text{CxFy}} \int f(\vec{v}, \vec{r}, t) |\vec{v}| \sigma_{\text{diss-iz to light species}}(v) N_{\text{CxFy}} N_e d^3v \quad (3.43)$$

$$R_{\text{phys.etch}} = +C_2 (\text{physical etch by ion bombarding}) = +C_2 (q) \quad (3.44)$$

$$R_{\text{passiv.CX}} = -C_3 \sum_{\text{Ar}^+, \text{CO}^+} \int f(\vec{v}, \vec{r}, t) |\vec{v}| \sigma_{\text{CX}}(v) N_{\text{CxFy}} N_{\text{Ar}^+, \text{CO}^+} d^3v \quad (3.45)$$

$$R_{\text{passiv.polymer}} = -C_4 \sum_{\text{CxFy}} \int f(\vec{v}, \vec{r}, t) |\vec{v}| \sigma_{\text{diss to heavy species}}(v) N_{\text{C4F8}} N_e d^3v \quad (3.46)$$

where  $C_j$  ( $j=1, 2, 3, \text{ and } 4$ ) are the function of the surface temperature which denotes the sticking coefficients and diffusion coefficients of Eq. 3.33 and 3.34, and their weighting are determined by the regression. Monitored PI parameters of  $b$  and  $q$  are adopted as representing parameter of  $f(\vec{v}, \vec{r}, t)$  and  $R_{\text{phys.etch}}$ , respectively. Detailed cross section are not included, and density of gas species are represented by the normalized OES signals to the Ar I 750 nm intensity. Although terms in the Eqs. 3.43 – 3.46 are simplified to the monitored sensor signals, nonlinear coupling and combination logic between PI parameters and the other EES variables was established based on the reaction mechanism in the process plasmas. Summation of Eq. 3.43 – 3.46 is defined as  $r_{\text{etch}}$ -factor which represents the overall etching reaction rate.

### 3.4.2 Evaluation of PI-VM performance by using $r_{\text{etch}}$ -factor

The  $r_{\text{etch}}$ -factor is normalized to follow the statistically standard distribution, and re-distributed according to the distribution property of the actual etch rates. From this data process, VM result is obtained as shown in Figure 3.13 and 3.14. Correlation coefficient between measured etch rate and predicted etch rate was  $R^2=96.9\%$ , and as expressed in Figure 3.13, etch rate prediction failed wafers by the previous  $\text{PCR}_0$  models also well aligned with the prediction succeeded wafers in the correlation diagram. Prediction error is noticeably decreased as 0.32 % as shown in Figure 3.14. Therefore, enhancement of the VM performance based on the 3 kinds of PI parameters is achieved for the plasma-assisted oxide etching process. This plasma information parameter based VM is named as PI-VM.

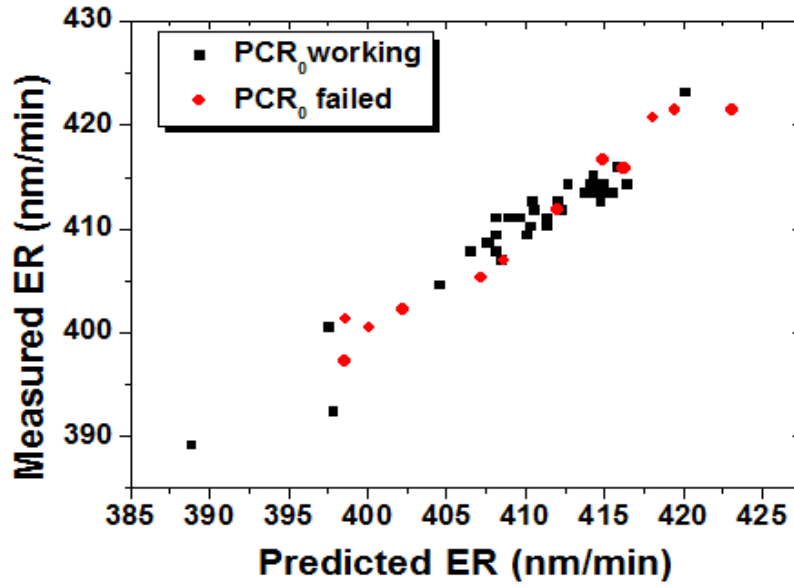


Figure 3.13 Correlation diagram of the measured etch rate and predicted etch rate by the PI-VM for 50 wafers.

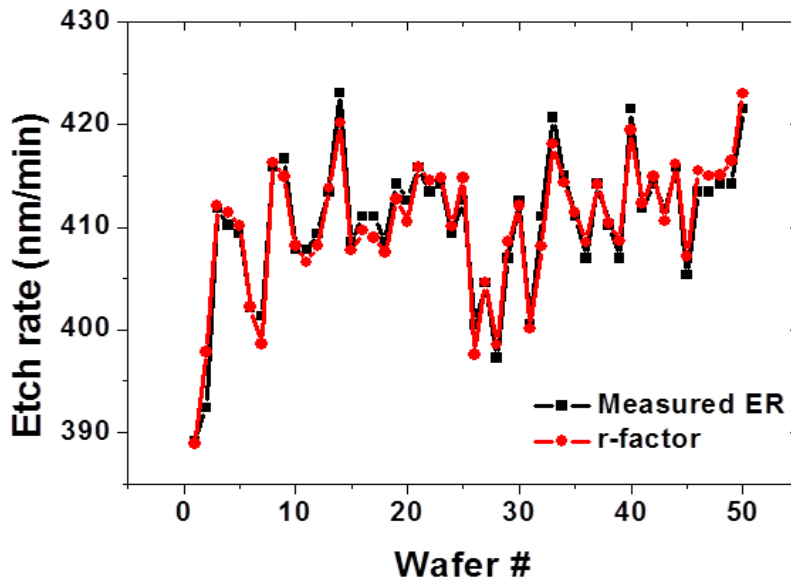


Figure 3.14 The comparison of the PI-VM result and the measured etch rate for 50 wafers.

## **Chapter 4 . Expansion of PI-VM Model for Plasma Enhanced a-Si Deposition Process**

To verify the versatile applicability of the developed PI-VM model to the plasma-assisted processes introduced in the previous chapter, PI parameters for a-Si deposition plasmas are drawn and thin film deposition rate of PECVD (Plasma Enhanced Chemical Vapor Deposition) process is predicted based on the developed framework of the PI-VM for etching process.

### **4.1 Experimental setup and access of sensing data**

To test the performance of PI-VM model for the prediction of a-Si thin film deposition rate, various sensor data as state variable are obtained in the narrow gap capacitively-coupled plasma (CCP) device. The RF power was introduced into the chamber through the top electrode with 13.56 MHz RF power supply, and the bottom electrode is grounded. The gap between top and bottom electrode was 18 mm during the a-Si thin film deposition. Gas inlets in the showerhead delivered the reactant gases of SiH<sub>4</sub>, and Ar into the chamber volume. Chamber wall and electrodes were maintained at a constant temperature by heater and chiller. a-Si thin film deposition was performed on the SiN - SiO<sub>2</sub> deposited glass, and source cleaning process is performed by using NF<sub>3</sub> plasma for every 6 glasses. The variables related to PECVD process are classified into 3 groups like as performed for etching process; manipulated variables (MVs), state variables (SVs) and performance variables (PVs). PVs and

output variables are desired to be applied for prediction of deposition rate in the context. Actual deposition rate was measured by using the ellipsometry. The standard process condition for a-Si thin film deposition in this experiment was set to 145 Pa during 45 sec per 1 glass. The PECVD process was repeated 500 times in reference process fixed condition.

The optical measurements were conducted using a CCD spectrometer (SD1024DL, Verity Instruments, Inc., wavelength range of 200-800 nm, resolution < 2.0 nm). The optical fiber was placed toward the center of the plasma and signals of total 1600 wavelengths were measured with 0.5 sec of time resolution.

The 18 kinds of EES variables were monitored with 0.5 sec of time resolution. EES data represent the conditions of applied power, power matching conditions, pressure gauge, temperatures of the electrodes, heater, and chiller, and gas flow conditions monitored at MFC (Mass Flow Controller), etc. Using these optical and EES signals, PI-VM for a-Si PECVD rate was performed.

## **4.2 PI parameters based on the a-Si thin film deposition mechanism**

Silicon thin film is produced by three representative methods [101-102]. The first one is growth of single crystalline silicon on the wafer which has mobility above 600 cm<sup>2</sup>/Vs. Because of the high mobility and defect-free quality, c-Si is applied to the system-LSI, memory, etc. The second one is the CVD (Chemical Vapor Deposition) of micro/poly-crystal Si on the glass. They have 50 – 100 cm<sup>2</sup>/Vs of mobility, and applied to the driver circuit, current driving TFT, OLED backplane, and so on. The last one is the PECVD (Plasma

Enhanced Chemical Vapor Deposition) of amorphous silicon (a-Si). The mobility of a-Si is 0.5-1 cm<sup>2</sup>/Vs, and applied to the pixel switching TFT (LCD backplane), etc. To obtain the high mobility of Si thin film, sufficiently crystallized silicon layer is needed. However, process time of the silicon layer production becomes longer to obtain the higher mobility, and this leads the decrease of process throughput. Although the physical properties of the deposited film are not proper to the industrial applications, film deposition rate of a-Si by the PECVD is overwhelmingly higher than the other kinds of the silicon layer production [102]. Therefore, to increase the economic efficiency of the process and to overcome the weak point of the a-Si, re-crystalline process of a-Si layer by the laser annealing is used in industry. As shown in Fig. 4.1, a-Si layer is deposited with high deposition rate by PECVD on the glass as a first step. This plasma-assisted deposition process causes undesired dangling bonds and hydrogen atoms in the silicon layer. To remove the dangling bonds and hydrogen atoms in the hydrogenated Si, annealing step is followed by heating. Finally, crystallization of the melted a-Si layer using the laser is performed and deposited a-Si layer is changed into poly-Si layer in ELA step. Final film thickness and quality of film are determined in the first PECVD step; thus, the management of plasma-assisted step process quality is the key of this process.

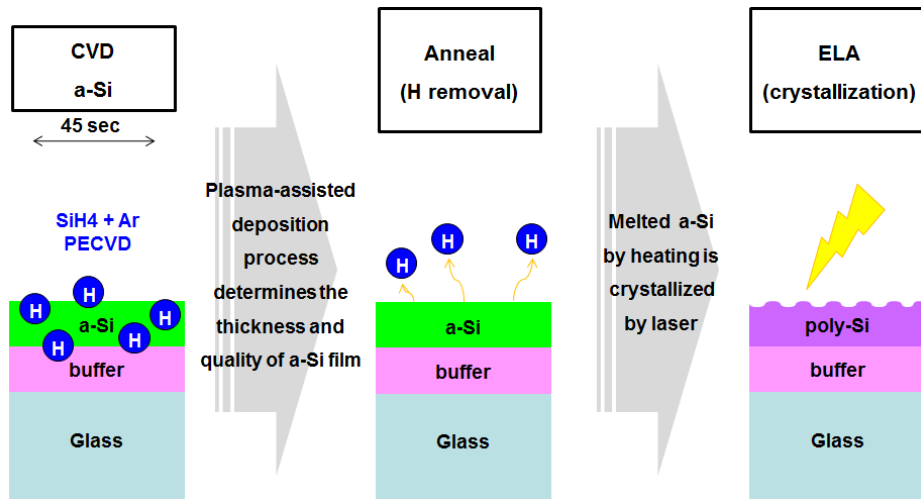


**Figure 4.1** The schematics of the a-Si thin film deposition process including the PECVD process.

To manage the deposited a-Si film thickness and quality constantly, understand about the deposition reaction mechanism in the a-Si deposition plasma is required. As considered in the oxide etching process case previously, reaction mechanisms in volume, sheath, and substrate surface are core components of the PI parameters. Especially, generation rate of the reactive radicals or ions and their transport onto the surface are dominated determinant of the film deposition rate [100]. Sticking or the surface diffusion properties also affect to the deposition rate [97-98]. To deduce the PI parameters appropriate to apply to the a-Si PECVD rate prediction, reaction mechanisms in the deposition process plasma volume, sheath, and the target surface are studied and PI parameters introduced in the PI-VM development for the etching process are modified in this chapter.

#### 4.2.1 Volume, sheath, surface reactions and PI parameters, $b$ and $q$

Most widely used gas for a-Si PECVD process is SiH<sub>4</sub>, silane gas [103-104]. Therefore, generation rate of deposition contributing or disturbing species, their transport property, and surface reaction property on the substrate of silane are crucial components for a-Si deposition reaction. Information to establish the deposition rate predicting VM should include these reaction properties of the plasma efficiently; thus, the PI parameters for the VM model operation were introduced according to the volume, sheath, and surface reaction characteristics of the SiH<sub>4</sub> based plasma.

Main bulk reactions in SiH<sub>4</sub> plasma are dissociation and dissociative ionization of SiH<sub>4</sub> molecule. Because of the stability of SiH<sub>4</sub> molecular structure as shown in Fig. 4.2, required energy to remove one hydrogen atom is high as about 8 eV compared to the other kinds of large molecules, and removal of one more hydrogen atom from already one hydrogen removed molecule requires more energy [105]. As a result, ionization cross section of SiH<sub>4</sub> series species are sensitively changed with the number of bonded hydrogen atom. Their reaction threshold energies are distributed at 7 – 13 eV range, which is similar to the inelastic process reaction threshold energies of O<sub>2</sub> and H<sub>2</sub>O molecules as shown in Fig. 4.3 [40-41]. Therefore, in the electron impact collisional inelastic process dominated plasmas, competition of SiH<sub>4</sub> and O<sub>2</sub> or H<sub>2</sub>O inelastic collisional reaction rates is occurred commonly; thus, the gas mixing ratio of SiH<sub>4</sub> based deposition plasma is an important parameter to the property of the volume reaction.

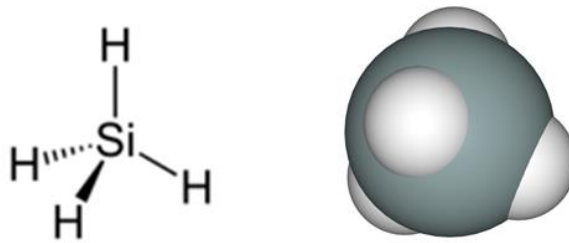


**Figure 4.2** The structure of SiH<sub>4</sub> molecule widely used for the PECVD processes

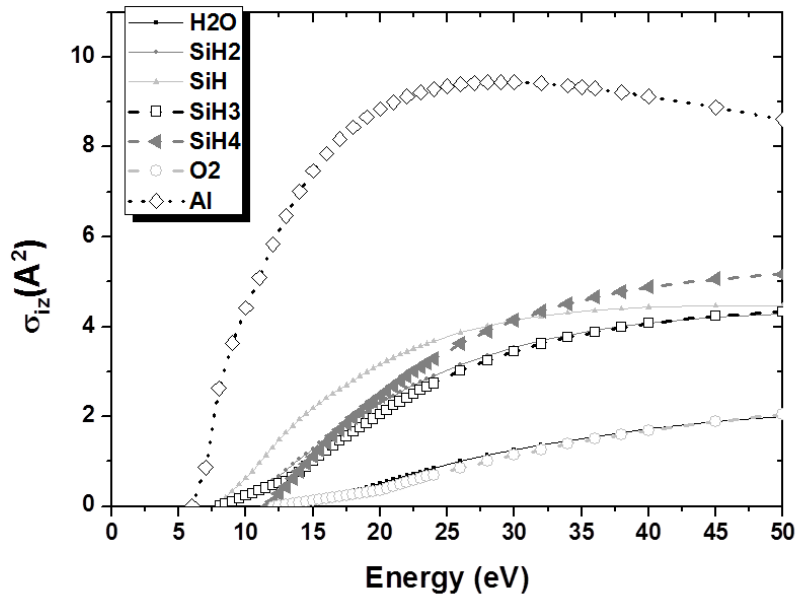
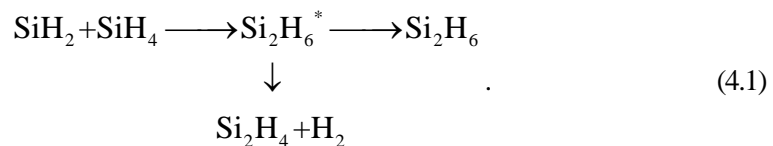


**Figure 4.3** Electron impact collisional ionization cross section of H<sub>2</sub>O, O<sub>2</sub>, Al, SiH<sub>4</sub> and fragments of SiH<sub>4</sub>.

For operating gas mixing ratio fixed cases as described in section 4.2, main reaction roots of SiH<sub>4</sub> molecule is determined by the thermal equilibrium state of the plasma. Most frequently generated species from the inelastic collisional reaction of SiH<sub>4</sub> molecule are SiH<sub>3</sub> and SiH<sub>2</sub> radicals and ions. These species very differently act to a-Si film deposition reaction.

SiH3 species has one reactive bonding arm because of one remained outermost electron of silicon atom to form the shared electron pair. This species can be incorporated into the film without remaining bonding arm or dangling bond generation [96]. Bonding of SiH3 radical onto the Si base substrate generates high quality thin film. Therefore, sufficient generation and transport onto the target surface of SiH3 radical or ion are required to a-Si thin film deposition. The other dominated species, SiH2 has two reactive bonding arms. This species has high sticking coefficient of near 1 onto the Si base surface; thus, directly incorporated to the film. However, as shown in Fig. 4.4, bonding of SiH2 onto the Si layer remains one- or two-unshared electron to the final layer. These irregular bonding generate dangling bonds and hinder the quality of deposited film. Moreover, chemical stability of SiH2 incorporated film can be very low and deposited film can be lost during the process. Eq. 4.1 is dominated reaction of SiH2 in SiH4 plasma bulk [96-97]:



Because of the abundance of SiH4 molecules in the deposition plasma with low degree of ionization, SiH2 radicals in the space and surface of the substrate collide with SiH4 molecules frequently [97]. Generated metastable species, Si2H6\*, is weak to the stimulations and dissociated into the Si2H4 and H2 gases or stabilized into Si2H6 molecule though Si2H6 is saturated molecule. Generated species from Si2H6\* are not incorporated into the film because of low sticking coefficients of Si2H4 and H2, and the volatility of Si2H6. Finally, SiH2 deposited film experiences adsorption, and unstably deposited film is lost.

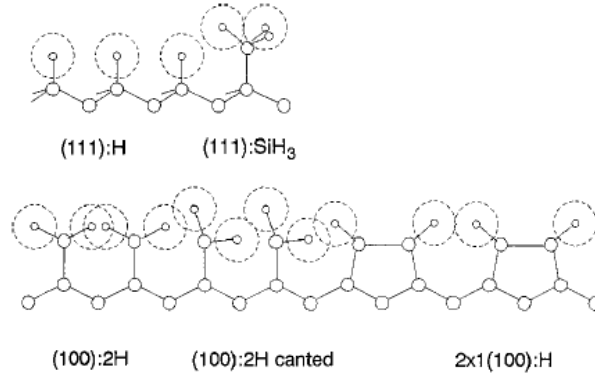


**Figure 4.4** Hydrogen terminations of the Si surface; Si(111):H, Si(111):SiH<sub>3</sub>, Si(100)2x1:H, and Si(100)1x1:2H [96].

Therefore, the deposition reactions by SiH<sub>3</sub> radical and ions are preferred than those by SiH<sub>2</sub> species. However, the sticking coefficient of SiH<sub>3</sub> onto the Si substrate is just 0.15 while that of SiH<sub>2</sub> is about 1. Generated SiH<sub>2</sub> species in the plasma volume reacts with the substrate surface with 7-time higher probability. This implies that the generation rate ratio of SiH<sub>2</sub> to SiH<sub>3</sub> governs the deposition reaction properties. To obtain the high quality of thin film with high deposition rate, enhancement of SiH<sub>3</sub> generation and suppression of SiH<sub>2</sub> generation is essentially required.

Fortunately, SiH<sub>3</sub> and SiH<sub>2</sub> have different generation threshold energy from SiH<sub>4</sub> feeding gas. The primary decomposition of monosilane is as follows;  $e + \text{SiH}_4 \rightarrow n \text{H} + \text{SiH}_{4-n}$  ( $n=1,2, \text{ and } 3$ ) depending on the electron energy. The generation of SiH<sub>3</sub> has the lowest threshold energy, 8.75 eV, and those for SiH<sub>2</sub> and SiH are 9.47 and 10.33 eV, respectively [106]. Collision with higher energy electrons above 10.36 eV generates Si, SiH<sub>2</sub><sup>\*</sup>, Si<sup>\*</sup>, etc [106]. This decomposition reaction nature of silane makes the description of a-Si thin film deposition rate as a function of EEDF become possible. Abundance of  $8.75 < \varepsilon < 9.47$  eV

electrons enhances the deposition reaction by the SiH<sub>3</sub> generation enhancement. Contrary, increase of the electrons have energies above 9.47 eV suppresses the deposition reaction. Therefore, the shape of EEDF tail also becomes core component governing the deposition reaction in the case of a-Si thin film PECVD process. b-factor again becomes the first PI parameter which includes the information about the volume reaction property, and applied to the PI-VM for a-Si PECVD monitoring.

As described in Fig.4.3, oxygen shares the inelastic collision energy range with SiH<sub>4</sub>. Because the initial facing material of the plasma on the glass is SiO<sub>x</sub>, molecular and atomic oxygen are introduced into the plasma volume. Moreover, heating of the deposition target substrate causes inflow of H<sub>2</sub>O and O<sub>2</sub> adsorbed from the glass surface. Therefore, reactions of the oxygen atom and oxygen including molecules with the high energy electrons are not negligible. Inflow of oxygen including species acts as disturbing species for the decomposition reaction of SiH<sub>4</sub> by the inelastic collision with the high energy electrons; thus, the abundance of these oxygen series should be considered into the PI-VM for a-Si PECVD. To include the information about the abundance of oxygen series, light emission intensities of O I, O<sub>2</sub>\* measured by the OES are applied to the PI-VM.

Generated species in the plasma volume are transferred onto the glass surface by the diffusion or acceleration in the sheath, and react with the substrate. Models explain the surface growth mechanism of Si:H film are classified into three categories : (a) surface diffusion model, (b) etching model, and (c) chemical annealing model [107-108].

#### **(a) surface diffusion model [107]**

The surface diffusion model is proposed to explain the correlation between the substrate temperature and deposition rate [108]. The surface diffusion coefficient (length) on the hydrogen-covered surface is enhanced by elevating the substrate temperature, leading to an

enhancement of crystalline volume fraction. The surface diffusion, however, is disturbed not only by ions impinging to the growth surface but also by the presence of surface dangling bonds appearing thermally above 400 °C, giving rise to a deterioration of crystallinity in the resulting films. Fig. 4.5 shows schematics of the surface diffusion model. Dissociated hydrogen atoms from the silane molecule cover the substrate surface, and produce local heating through hydrogen-recombination reactions on the growth surface of the film. These processes occurring on the surface enhance the surface diffusion length of film precursors (SiH<sub>3</sub>). As a consequence, film precursors adsorbed on the surface can find energetically favorable (stable) sites, leading to a formation of atomically flat surface. The adsorbed SiH<sub>3</sub> radical reacts with the hydrogenated Si surface by abstraction or addition, which creates and removes surface dangling bonds [96]. These reactions determine the dangling bond density in a bulk a-Si:H, by assuming that the surface dangling bonds are buried unchanged by growth to become bulk defects. In these processes, the performance to the growth of the film is determined by the diffusion length of the SiH<sub>3</sub> radical. Until the most stable site is found on the growth surface, SiH<sub>3</sub> radical diffuses on the surface. To find the stable site faster, enough diffusion length should be provided and the kinetic energy of the radical to diffuse on the surface is determined by the temperature of the substrate surface as [97]

$$D_s = \exp\left(-E_s / kT_{surf}\right) \quad (4.2)$$

where  $D_s$  is the surface diffusion coefficient,  $E_s$  is the bonding energy between the radical and surface, and the  $T_{surf}$  is the temperature of the substrate temperature. This implies that the surface reaction rate to deposit the a-Si:H thin film in silane based plasma is a function of surface temperature, and surface temperature monitored results in the deposition system would be applied to the PI-VM model as one of the important EES parameter.

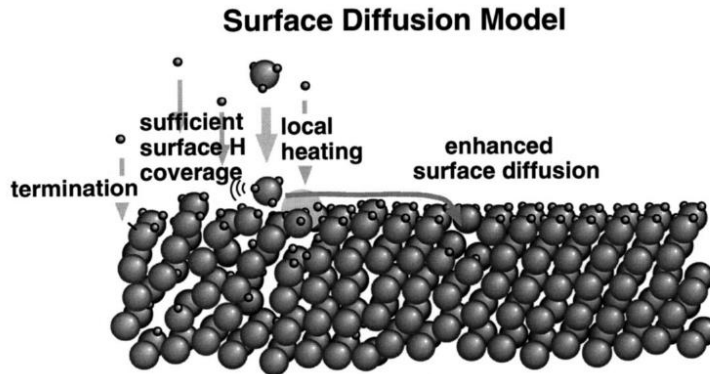


**Figure 4.5** Schematics of the surface diffusion model for a-Si deposition [107]

**(b) Etching model [107]**

An etching model was proposed based on the experimental fact that film growth rate is reduced by an increase of hydrogen dilution [109]. A schematic concept of the etching model is shown in Fig. 4.6. An atomic hydrogen provided on the film-growing surface breaks Si-Si bonds, preferentially the weak bond, involved in the amorphous network structure, leading to a removal of a Si atom bonded more weakly to another Si. This site is replaced by a new film precursor, forming a rigid and strong Si-Si bond again. An important concept of this model is the removal of Si (etching) from the surface by atomic hydrogen (presumably by forming SiH<sub>4</sub>) and the replacement with another Si forming rigid crystalline structure. These processes are governed by the supply of hydrogen atom and precursor radicals which are generated in the volume of the plasma. Means, the surface reaction is not independent term; thus, this term should be coupled with the volume reaction term to establish the PI-VM model.

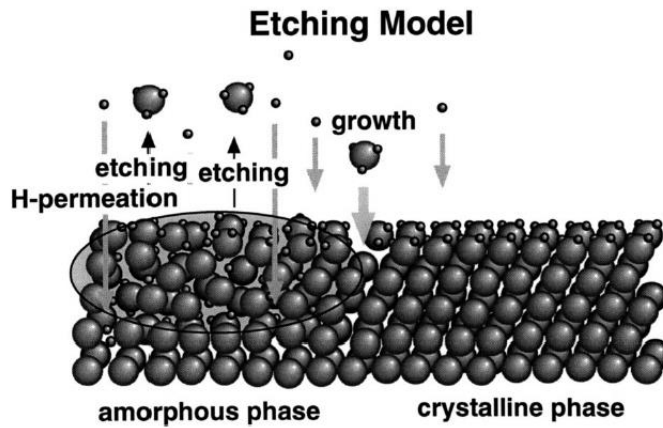


**Figure 4.6** Schematics of the etching model for a-Si deposition [107]

**(c) chemical annealing model [107]**

A model similar to the etching model was proposed for explaining the experimental fact that crystal formation is observed during the hydrogen plasma treatment in a layer-by-layer growth by an alternating sequence of amorphous film growth and hydrogen plasma treatment [110]. Several monolayers of amorphous silicon are deposited and these layers are exposed to hydrogen atoms produced in the hydrogen-abundant plasma. These processes are repeated alternately for several ten times to fabricate the proper thickness for the evaluation of film structure. The absence of a remarkable reduction of film thickness during the hydrogen plasma treatment is hard to explain by the etching model and a new model is proposed as shown schematically in Fig.4.7. During the hydrogen plasma treatment, many hydrogen atoms are permeating in the sub-surface region (called as growth zone), giving rise to a crystallization of amorphous network through the formation of a flexible network with a sufficient amount of atomic hydrogen in the sub-surface region without any removal (etching) process of Si atoms. This is named as the chemical annealing process. These processes imply that the supply and permeation of hydrogen are crucial components to deposit the thin film.

The supply of hydrogen atom is governed by the volume reaction rates in the plasma as explained in etching model, and the permeation of hydrogen atom is determined by the permeation length of the hydrogen like as a surface diffusion. Therefore, chemical annealing model gives a confirmation about the importance of surface temperature and dependency to the volume reaction rates to the development of PI-VM for deposition process. This is the reason that b-factor is also an important core PI parameter in a-Si deposition process PI-VM model.

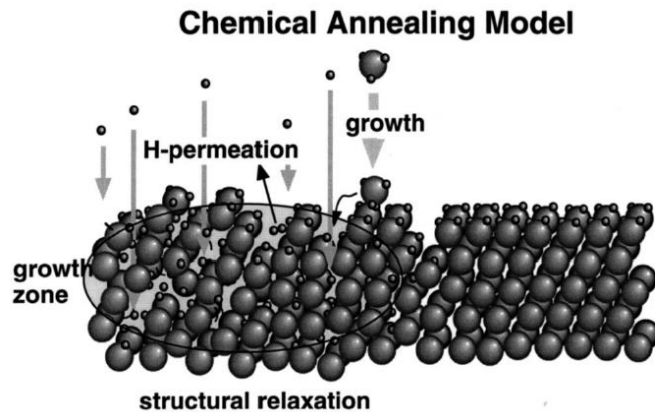


**Figure 4.7** Schematics of the chemical annealing model for a-Si deposition [107]

#### 4.2.2 Film quality determination mechanism and q-factor

As described in chapter 4.2.1, existence of dangling bond is dominant cause of the film quality degeneration. Perfect suppression of SiH<sub>2</sub> generation in the plasma volume and sticking onto the substrate surface is impossible, and dangling bond on the growth surface is unavoidably appeared. Consequently, efficient removal of dangling bond on the growth

surface enhances the quality of deposited film.

Most efficient removal of dangling bond is breaking of existing dangling bond by ion bombarding [111]. To break the dangling bond on the growth surface, enough energy of bombarding ion exceeding the bonding energy between the Si atoms is needed. The dangling bonding energy between Si atoms required to be broken is about 2 eV, and the ion bombarding energy accelerated through the floating sheath without the additional bias power is a few eV. Therefore, the dangling bond removal rate is sensitively changed with the variation of the ion bombarding energy [112].

As described in chapter 3.2.2, ion bombarding energy accelerated through the sheath is a function of the electronegativity and the EEDF of the plasma. SiH<sub>4</sub> based plasma in the range of corona equilibrium model applicable  $n_e$  and  $T_{e,eff}$  has electronegativity of  $\alpha_0 = n_-/n_+ = 0.2 \sim 0.3$  [25, 113]. For these electronegative plasmas applied to the a-Si deposition processes, addition of 5% molar fraction of F<sub>2</sub> causes 30% increase of the electronegativity, and 2 – 3 eV of the  $T_{e,eff}$  can be varied quite drastically [25]. This causes about 50% of ion bombarding energy drop, and the dangling bond removal rate on the growth surface can be noticeably fluctuated.

Because the dangling bond removal rate is sensitive to the variation of the electronegativity of the SiH<sub>4</sub> based deposition plasma, the cause of the electronegativity variation should be considered to establish the appropriate PI for a-Si deposition process VM. As Yan experimented, addition of fluorine into the SiH<sub>4</sub> plasma changes the electronegativity drastically even small amount of the electronegative gas added cases. Although fluorine series gas is not included in the a-Si deposition plasma, channel of the fluorine atom inflow into the processing plasma exists. To maintain the process device condition in the allowed range, cleaning process is carried out periodically. Most of chamber pollution is caused by the undesired deposition of the materials by the deposition plasma on the chamber inner wall; thus,

cleaning process is performed as the reversed reaction, film etching process. NF<sub>3</sub> and CF<sub>4</sub> are most widely used cleaning gases on the cleaning discharge step of the deposition processes, and NF<sub>3</sub> gas is applied as a cleaning gas in this dissertation for every 6 glasses. NF<sub>3</sub> molecule has low dissociation energy and F radical and ions are generated abundantly, thus cleaning efficiency of the deposited contaminant is higher than the other F series gases. F radicals are adsorbed on the inner wall of the chamber, and are not removed perfectly during the exhaustion before the deposition step. Residual fluorine particles can be outgassed during the deposition step, and perturb the electronegativity of the processing plasma. Sensitive variation of the electronegativity of deposition plasma leads the noticeable variation of ion bombarding energy by the residual cleaning gases.

According to Zhou *et al.*, [114] initially deposited thin layer of about 10 Å (named as initial seed layer) determines the overall quality of deposited film. If the initial seed layer has many dangling bonds, next layer has also unstable structure by the asymmetric next bonds. This implies that the sufficient ion bombarding energy is important during the initial seed layer deposition to remove the dangling bonds to obtain high quality of the deposited film. Deposition time of the initial seed layer is a few seconds in general; thus, residual cleaning fluorine gases adsorbed in the previous step influence to the initial deposition time and the electronegativity of the initial deposition time perturbed noticeably. Therefore, inclusion of the information about the fluorine concentration in the process chamber is important to the deposition process monitoring. To adopt this property of the a-Si thin film deposition process into the PI-VM, q-factor introduced in chapter 3.2.2 is applied again.

## 4.3 Evaluation of PI-VM model to the a-Si PECVD

### 4.3.1 Organization of $r_{\text{depo}}$ -factor

To combine the monitored PI parameters according to the reaction mechanism described in the chapter 4.1 and 4.2,  $r_{\text{depo}}$ -factor which represents the deposition reaction rates in the plasma is introduced with the similar framework with  $r_{\text{etch}}$ -factor. Eq. 3.42 is chosen as the main framework of the a-Si PECVD PI-VM, also. PI parameters of  $b$  and  $q$  are adopted as core parameters again, but the third PI parameter of  $r_{\text{etch}}$ -factor which represents the pattern-passivation property in the etching process is not included in the  $r_{\text{depo}}$ -factor.

Overall reactions occurred in the deposition plasma reactor can be classified into the “deposition contributing reactions” and “deposition disturbing reactions”. Dissociation of  $\text{SiH}_4$  to generate  $\text{SiH}_3$  radical and ion is the deposition contributing reaction. On the other hand, the inelastic collisional reaction of oxygen and dissociative attachment reaction of fluorine series gas which perturbs the electronegativity of the plasma are dissociation disturbing reactions. These volume reactions are governed by the EEDF of the plasma volume which are represented as the PI parameter,  $b$ . Ion bombarding energy to remove the dangling bond of the growth surface, represented as the PI parameter  $q$ , is coupled with the deposition contributing volume reaction rate. Finally, the surface temperature which determines the surface diffusion coefficient and sticking coefficient is coupled with both deposition contributing and disturbing terms. Following equation shows the structure of the deposition rate predicting  $r_{\text{depo}}$ -factor.

$$\left. \frac{\partial N(\vec{r}, t)}{\partial t} \right|_{C_{ij}} = \sum_{i,j} (\pm) \int f(\vec{v}, \vec{r}, t) |\vec{v}| \sigma_{ij}(v) N_j N_i d^3v \quad (4.3)$$

$$= +C_1 \sum_{\text{SiH}_4} \int f(\vec{v}, \vec{r}, t) |\vec{v}| \sigma_{\text{SiH}_4}(v) N_{\text{SiH}_4} N_e d^3v \quad (4.4)$$

$$-C_2 \sum_{\text{O}_2, \text{F}} \int f(\vec{v}, \vec{r}, t) |\vec{v}| \sigma_{\text{O}_2, \text{F}}(v) N_{\text{O}_2, \text{F}} N_e d^3v \quad (4.5)$$

where  $C_1$  and  $C_2$  are the function of the surface temperature like as used in the Eqs. 3.43 - 3.46. Their weightings are determined by the regression for 150 glasses of training set. Equation 4.3 is defined as  $r_{\text{depo}}$ -factor which represents the overall deposition rate of PI-VM model.

### 4.3.2 Performance of PI-VM by using $r_{\text{depo}}$ -factor

The  $r_{\text{depo}}$ -factor is normalized to follow the statistically standard distribution, and re-distributed according to the distribution property of the actual deposition rates. From this data process, PI-VM result is obtained as shown in Fig. 4.8. Correlation coefficient between measured deposition rate and predicted deposition rate was 93.4 %, and as expressed in Fig. 4.8, deposition prediction for the validation set of 350 glasses was reasonable. And as shown in Table 4.1, error of the deposition rate prediction was 0.291 % which satisfies the accuracy requirement of the industry (error < 0.4 %). To confirm the enhancement of VM performance by the application of PI, PCR based VM results are also compared in Table 4.1.

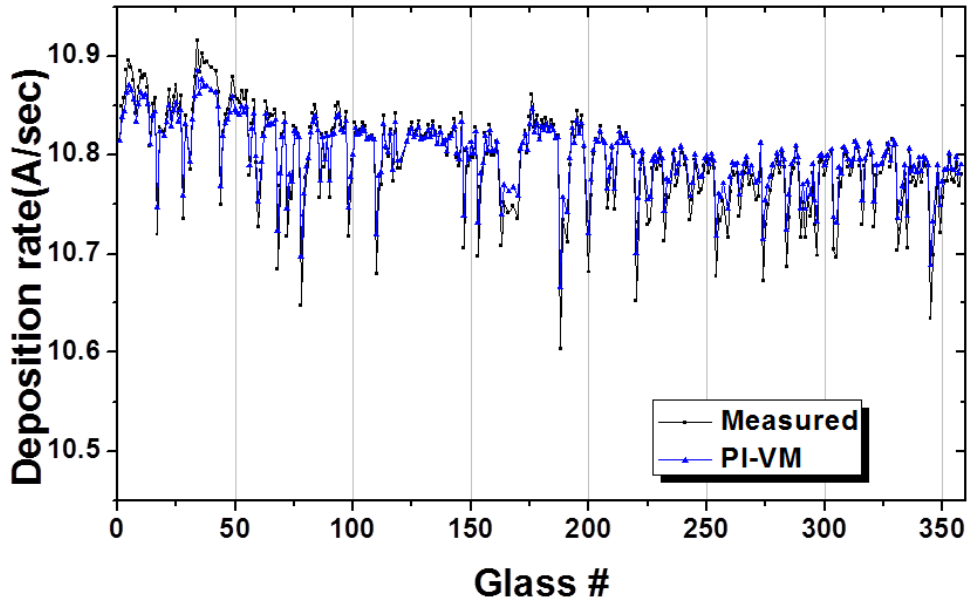


Figure 4.8 The comparison of the PI-VM results and the measured deposition rate for a-Si PECVD process.

Table 4.1 Error of the a-Si PECVD rate prediction by using the VM methodologies of PI-VM,  $PCR_0$ , and  $PCR_{b,q}$ .

VM methodology	Error of the prediction
PI-VM ( $r_{depo}$ -factor)	0.291 %
$PCR_0$	1.01 % (> 0.4 % , under requirement)
$PCR_{b,q}$	0.701 % (> 0.4 % , under requirement)

## **Chapter 5 . Characteristics of PI-VM for Plasma-assisted Etch-Deposition Processes**

Developed PI-VM is the plasma-assisted process monitoring algorithm based on the efficient application of the sensing variables to have physical information in terms of the PI parameters. Processing methodologies of the sensing variables to extract the main PI parameter  $b$ , and the sub PI parameters  $q$  and passivation species, according to the reaction mechanism in the process plasma was important step to develop the PI-VM model, which can determine the performance of VM. Therefore, the evaluation of the sensing variables which consisting the PI parameters can gives us the unrevealed information about the relationship between the state variables, manipulated variables and the performance variables, as the results of the processes. In this chapter, classification of the sensing variables to analysis the role of the PI parameter consisting components to the PCs is performed, and characterization of the PI-VM is performed based on this analysis. According to this result, the characteristics of PI-VM are evaluated by the application to the cause analysis of the chamber to chamber (C2C) matching problem.

### **5.1 Characterization of the PI-VM consisting variables**

#### **5.1.1 Classification of the monitoring sensing variables**

The state variables obtained from the OES and EES data to monitor the state of process

and extract the PI parameters can be classified into 3 groups according to their role to the state monitoring.

The first group is ‘plasma parameters’. Introduced PI parameters and OES signals represent the thermal equilibrium state and sheath property influenced by the volume reactions of the plasma, and the abundance of specific species or the excited state of corresponding particles, respectively. These sensing variables contain the information about the property of the plasma, thus classified as plasma parameters. These plasma parameters are composed by the PI parameter or PI parameter composing variables.

The second group is ‘operating parameters’. Sensing variables from EES data providing the information about the state of operating powers are classified into this group. Such as applied power, reflected power, power matching condition, etc. are classified into the operating parameters. The operating parameters govern the physical property of the plasmas as the characteristics of the discharge source, thus contains the information about absorbed power by the plasma for heating and breeding.

The third group of the sensing variables is ‘device parameters’. Sensing variables from EES data representing the other process device properties are classified into this 3<sup>rd</sup> group. Classified parameters are electrode surface temperature, MFC (Mass Flow Controller) condition, pressure gauge, etc. These device parameters give information about the detailed management state and spec of the processing devices.

According to this classification of the sensing variables, the characteristics of the PCs introduced in the section 3.3 are revalued.

### 5.1.2 Characterization of the PCs

The PCs composed by the sensing variables based on the PCA were characterized by the contribution analysis of the classified sensing variable groups. Monitoring parameters are classified into the plasma parameter, operating parameter, and device parameter are described in section 5.1.1, and their contributions to the each of the PCs are estimated by the summation of cumulated variances of the same group parameters. By this calculation, fractions of the cumulated variances for plasma, operating, and device parameters are obtained as shown in Fig. 5.1 for C4F8-oxide etching process. As described previously in section 3.3, the 1<sup>st</sup> PC represents the chemical reaction property, the 2<sup>nd</sup> PC represents the physical reaction property, and the 3<sup>rd</sup> PC represents the sheath-surface reaction property of the electronegative plasma.

The weighting of the PCs for VM is obtained by the linear regression to predict the performance variables as described method in section 3.3, and the results were 0.588, 0.316, and 0.097 for the 1<sup>st</sup> PC, the 2<sup>nd</sup> PC, and the 3<sup>rd</sup> PC, respectively. Without the consideration about the PI parameters  $b$  and  $q$ , the weightings were different as 0.1231, 1.3470, and 0.7204. The weighting on the 1<sup>st</sup> PC was too low because the information about the chemical reactions in the plasma volume represented by the PI parameter  $b$  is not included in the 1<sup>st</sup> PC, thus the efficiency of the PC for the VM performance had gone off. After the containing the plasma information into the PCs, the weighting of the chemical reaction is increased drastically, and the weighting of the other reaction properties are relatively decreased.

According to the analyzed result in Fig. 5.1, the contribution of the plasma parameters to the chemical reaction property represented as the 1<sup>st</sup> PC is absolutely large as 98.4%. As mentioned in section 3.2.1, chemical reaction rate of the etching process is determined by the main PI parameter, dominantly. The validity of the  $b$ -factor as a chemical reaction rate representing parameter in the plasma volume can be checked again from this statistical

variance analysis.

The physical reaction property of the plasma represented as the 2<sup>nd</sup> PC was influenced by the operating parameters dominantly. According to this result, absorbed power condition was important to determine the physical property of the process plasma, and plasma parameters contributed considerably to the physical reaction property, also.

The sheath-surface reaction property of the process plasma which is represented as the 3<sup>rd</sup> PC was dominantly influenced by the plasma parameters and operating parameters. This result shows the dependency of the sheath-bulk reaction properties to the reaction properties in the plasma volume, as described by the dependency of the q-factor on the b-factor. In addition, device parameters also contribute to the 3<sup>rd</sup> PC considerably as 13.4 %. The importance of the device parameters was not noticeable to the 1<sup>st</sup> and 2<sup>nd</sup> PCs, but the contribution to the sheath-surface reaction properties is not negligible level. This explains the importance of the substrate temperature and correlated surface diffusion and sticking phenomena to the surface reaction rate of the plasma. And the pressure gauge and MFC conditions which can change the detailed pressure or gas mixing ratio can affect to the sheath property of the process plasmas.

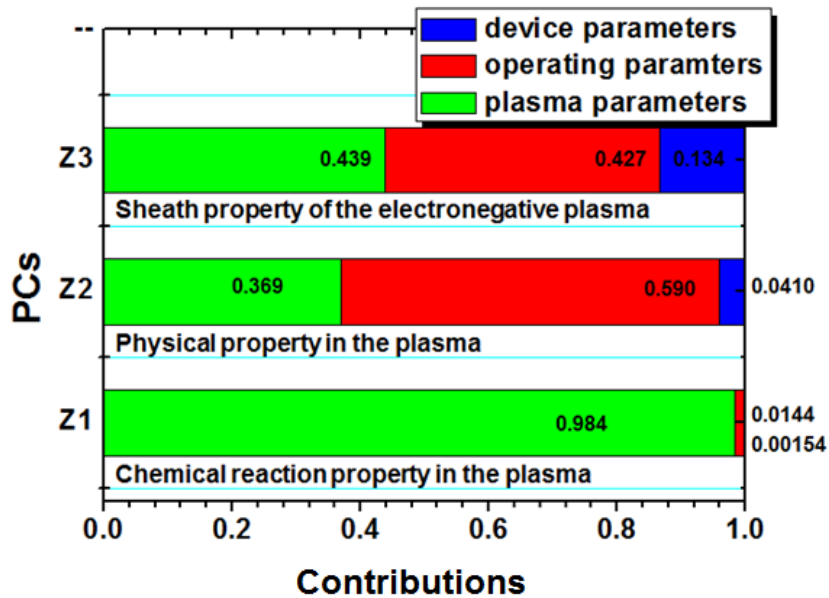


**Figure 5.1** Evaluation of the PCs based on the classification of the sensing variables into the plasma parameters, operating parameters, and device parameters for C4F8-oxide etch process analyzed in this thesis.

Same analysis on the PCs based on the classification of the sensing variables is performed for a-Si PECVD processes as shown in Fig. 5.2. Contribution orders of the classified parameters to the each of PCs are similar with the case of oxide etch, but the overall contributions of the device parameters are increased. This result shows that the deposition process is more sensitive to the detailed characteristics of device correlated with the surface temperature or pressure than the etching process while the contribution of the overall reaction mechanisms in the plasma volume, sheath, and surface to the process results has substantial similarities.

These results imply that the plasma volume reaction rates in bulk plasma determines the overall process rates. However, the detailed results of the process are sensitive to the

characteristics of the process device which determines the sheath-surface reaction property of the process plasma. This suggests that to determine the dominated property of the process plasma, operating condition describing recipe is important. On the other hand, to control the detail of the process, characterization of the process device can be a key for the process control model. And this is a strong point of the PI-VM which gives the information about the correlation between operating parameter and process results based on the analysis of the sensing variables. This analysis can be performed because the PI-VM contains the information about the process plasma based on the reaction mechanisms in the plasma, and makes the understanding of the dependency of the process results on the characteristics of the process device become possible as a generalized VM model for the plasma-assisted etch and deposition process.

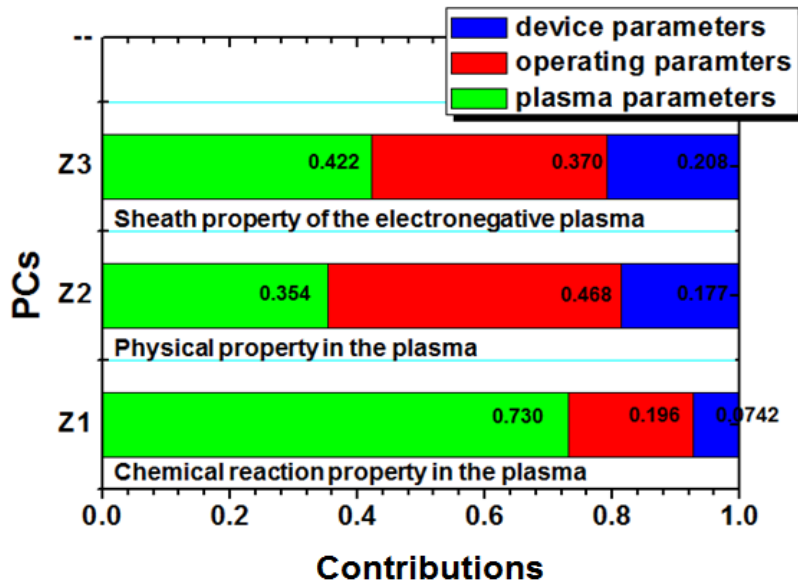


**Figure 5.2** Evaluation of the PCs based on the classification of the sensing variables into the plasma parameters, operating parameters, and device parameters for a-Si PECVD process analyzed in this thesis.

## **5.2 Application of the PI-VM for chamber to chamber (C2C) matching problem**

Analysis on the characteristics of the PI-VM performed in the previous section implies that the applicability of the PI-VM model to the cause analysis of the process result deviation, as a basis of the fault detection and classification (FDC) algorithm. According to this result, this characteristic of the PI-VM model is evaluated by the application to the monitoring of the chamber to chamber (C2C) matching problem.

Fukusawa *et al.* monitored the effects of wall contamination on the SiN etch rates by monitoring the sensor signals derived from the plasma-wall interactions [115]. They observed unexpected irregular variations in the process results, which they called ‘fluctuations’, because they were random and small in scale compared to the total etching or deposition process rates. They found that small variations in the process gas mixing ratios or partial pressures due to the out-gassing of wall contaminants could introduce fluctuations, suggesting that the wall conditioning was very important to the process conditions. These results suggested that subtle changes in the partial pressures of the plasma gases should be monitored to maintain process conditions.

The vacuum pump itself presents an important source of subtle changes in the gas mixture conditions. At the base pressure, the gas composition consists mainly of oxygen and nitrogen. These gases are pumped off differently due to mass differences. As the turbine rotation speed decreases and the blades of the turbo molecular pump erode, a different oxygen and nitrogen mixing ratio may form in the process gas. The effects of the pump age on the process are very difficult to characterize because deviations in pump-to-pump performances are subtle and changes in the gas mixing ratio may be observed from a comparison of the process results. Sensitive methods are required for monitoring the fluctuations in a process as a result

of pump age effects.

In this section, it is examined the effect of variations in the gas mixing ratio as a result of vacuum pump aging on the etching process, and the main PI parameter  $b$  is monitored using the optical emission spectroscopy. A Cr etching process under an Ar/O<sub>2</sub>/Cl<sub>2</sub> mixture plasma was selected as the target process because it provided sensitivity to the oxygen and nitrogen mixing ratio. Ichiki *et al.* reported that an 1-% molar fraction of O<sub>2</sub> gas can increase the chromium etch rate under an Ar/O<sub>2</sub>/Cl<sub>2</sub> plasma by a factor of 20 [116]. This report is coincident with the analysis in the section 2.3.2 which describes the variation of thermal properties of the plasma due to changes in the gas mixing ratio. Identical operational conditions were applied in the two process devices equipped with either old or new versions of the vacuum pump. Because the differences in the nitrogen partial pressure influenced the rates of oxygen and chlorine radical generation, which are primary factors that affect the Cr etching reaction rate, the radical production rates were discussed. The subtle differences in the O<sub>2</sub>/N<sub>2</sub> ratio, which was determined by the pump performance, resulted in significant differences in the Cr etch rate under the Cl<sub>2</sub> plasma.

Chromium etching processes were performed in two capacitively-coupled plasma (CCP) etchers equipped with pumps of different ages. The manufacturer and specifications of the turbo molecular pumps (TMPs) installed in the etchers were identical, as were the main vacuum pumps, which were operated at 36000 rpm. The process conditions in both etchers were identical, 3 mTorr of the Cl<sub>2</sub>, O<sub>2</sub>, and Ar gas mixture, and the gas flow rates were set to 180 sccm for Cl<sub>2</sub>, 30 sccm for O<sub>2</sub>, and 10 sccm for Ar. The base pressures of the systems were less than 0.01 mTorr, so a maximum of 0.3 % partial pressure of air species could have been present in the process gases. An RF power of 13.56 MHz was delivered at 300 W to the two identical CCP sources. The effects of subtle differences in the base pressure were monitored. The pumping performances were evaluated by monitoring the variations in the

partial pressures of nitrogen and oxygen, as measured using a residual gas analyzer (RGA: Hiden Analytical Inc.) during the 100 sec argon purging - exhaustion time. The dependence of the RGA intensities on the compensated sensor conditions was removed by monitoring variations in the partial pressure via the intensity ratios of the nitrogen and oxygen signals to the argon signal, as shown in Fig. 5.3. The argon flow rate during the argon purging step was assumed to be the set value; however, the residual gas remained uncontrolled due to differences in the pumping performance, as shown in Fig. 5.3. Hereafter, the etcher prepared with the new pump was designated  $\text{etcher}_{\text{new}}$  and the etcher with the old pump was designated  $\text{etcher}_{\text{old}}$ . The rate at which residual nitrogen was exhausted from  $\text{etcher}_{\text{old}}$  exceeded the rate at which it was exhausted from  $\text{etcher}_{\text{new}}$  up to 50 sec, and the saturated RGA intensity ratios of two etchers after 50 sec of pumping were almost identical, as shown in Fig. 5.3(a). Note that the etching process proceeded for 60 sec after purging, so this pump performance could influence the etching process. The residual oxygen exhaustion rates in  $\text{etcher}_{\text{old}}$  and  $\text{etcher}_{\text{new}}$  were nearly identical, as shown in Fig. 5.3 (b). Previous studies reported that the worn-down blades of an old TMP can increase the channel dimensions of the pump [117-119], and the compression ratio  $K$  can be estimated according to

$$K \sim \exp(\sqrt{Mug}), \quad (5.1)$$

where  $M$  is the molecular weight of the gas pumped,  $u$  is the circumferential speed of the rotor discs, and  $g$  is a factor that depends on the pump geometry. Note that  $K$  is very sensitive to the molecular weight  $M$  [118]. The air evacuation step mainly involved removing oxygen, with a molecular weight of 32, and nitrogen, with a molecular weight of 28. The compression factor of oxygen is twice that of nitrogen, suggesting that nitrogen was more

dominant in the residual gas than oxygen and contributed more significantly to variations in the geometric dimension or performance degradation of the pump. Differences in the partial pressures of nitrogen in the residual gases of the two etchers during the exhaustion time are shown in Fig. 5.3. Note that the chromium etching process involved repeated 100 sec argon purging periods and 1 min etching periods.

The effects of minute differences in the N<sub>2</sub> exhaustion rate on the plasma properties during the processes were monitored as the PI parameter, *b*. The self-excited electron resonance spectroscopy (SEERS, measured using a HerculesAPC™ from ASI GmbH) was also employed to monitor the electron density [120]. A residual gas analyzer was employed to monitor the changes in the species densities produced in the plasma.

The target was prepared as the chromium film was deposited onto Si wafers ~100 nm thick, and each wafer was etched over 1 minute. The operating conditions were fixed to the initial values applied during the etching process, and 21 wafers were etched per etcher over a 3-day period (7 wafers / day). The etching results were analyzed using scanning electron microscopy (SEM) to measure the etch rates.

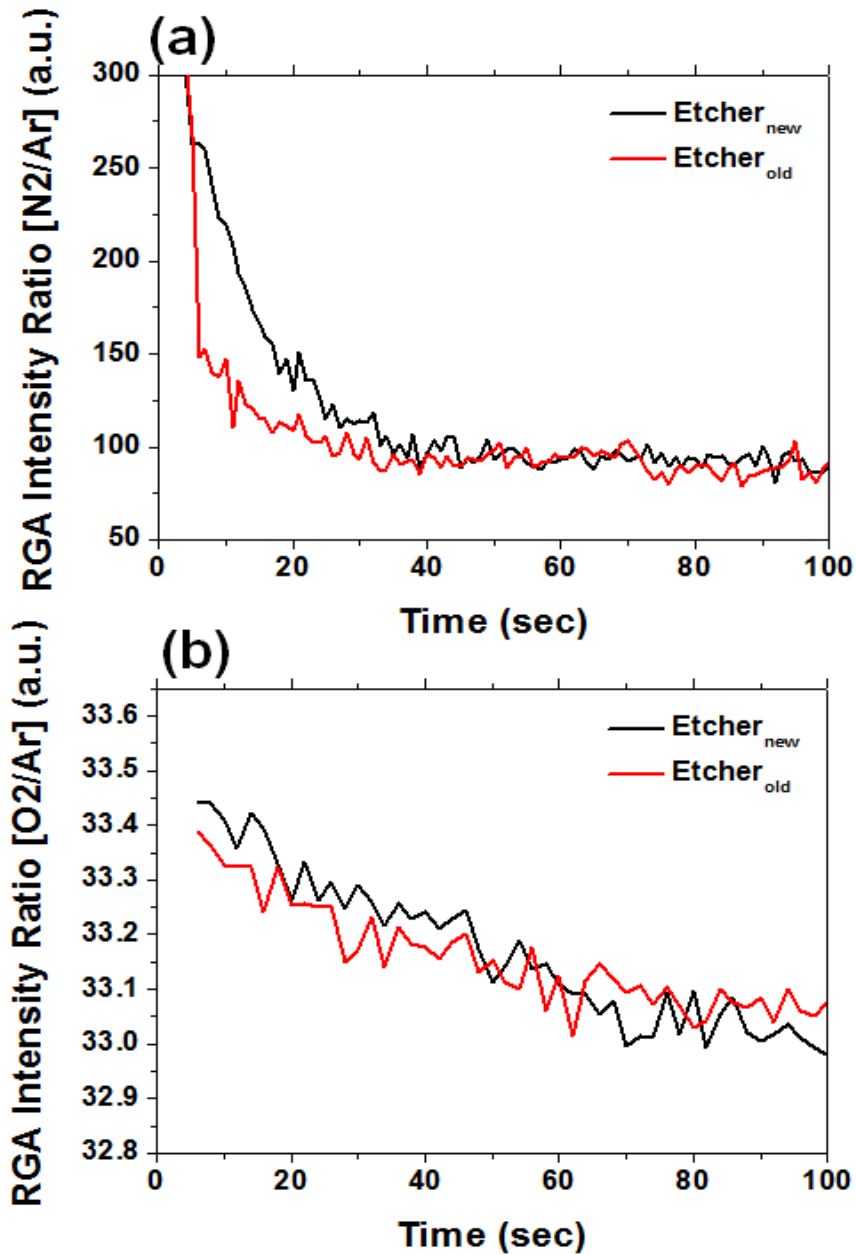


**Figure 5.3** RGA intensity ratio of the residual (a) nitrogen and (b) oxygen gas, normalized by the argon intensity, present in the two etchers measured during the argon purging-exhaustion step. The chromium etching process analyzed in this experiment was performed under repeated 100 sec exhaustion and 1 min etching cycles.

The Cr etch rate was assumed to depend closely on the fluxes of atomic chlorine and oxygen radicals onto the chromium metal film as a volume reaction contributing species. The concentrations of radicals in the bulk etching plasma could be estimated from an analysis of the generation rate constant, which was governed by the EEDF of the process plasma as described in the section 3.2. The effects of small variations in the gas composition of the etching processes were evaluated by using the b-factor of the EEDF. The EEDF analysis provided the effective temperature of the electrons [17] and the reactive chlorine and oxygen radical generation rates according to the Eq. 3.39 which composes the  $N_j$  in the PI-VM. The radical generation rates could be used to predict the variations in the chromium etch rate as a PI-VM, and quantify the effects of the gas mixing ratio variations on the etch rates. The predicted variations in the radical generation rates and the measured etch rates were verified by comparing the oxygen, nitrogen, and reaction product data derived from the RGA data. The electron density measured by SEERS [120] was nearly identical in the two etchers,  $n_e = (5 \pm 0.2) \times 10^{16} \text{ m}^{-3}$ , and this value was used in the analysis. The electron temperature obtained from the argon spectrum was  $T_{e,eff} = (4 \pm 0.1) \text{ eV}$ , and the b-factor obtained from the two etchers are shown in Fig. 5.4.

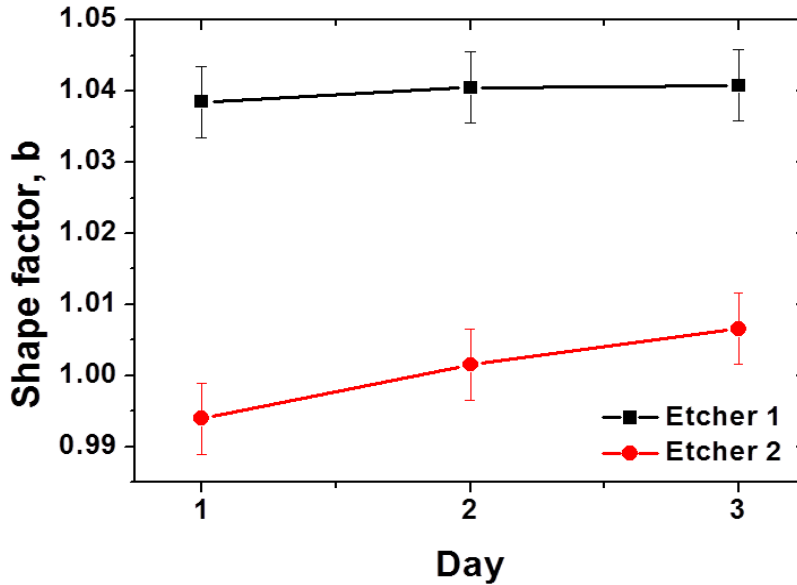


**Figure 5.4** b-factors of the two etchers during the etching process, measured using the OES signals. Twenty-one wafers were etched in each etcher during the 3-day test period (7 wafers/day). Note that the error bars of the b-factors indicate the standard deviations from the one-day b-factors during the etching process, determined from 7 wafers collected from each of the etchers.

b-factors presented in Fig. 5.4 indicated that the EEDF tail of the etcher<sub>new</sub> was relatively curtailed compared to that of etcher<sub>old</sub> during the etching process. Fig. 5.5 shows the log scale EEDFs obtained from the etching plasmas, based on the monitored  $T_{e,eff}$  and  $b$ . The tail of the distribution, which defined the high-energy region above the threshold of the Ar I light emission spectra (13 eV) in this dissertation [29], was depleted in etcher<sub>new</sub> whereas the lower energy regions, less than 13 eV, remained constant. These results suggest that a greater number of inelastic collisions occurred in the plasma of etcher<sub>new</sub> than in that of etcher<sub>old</sub> due to the exhaustion property differences between the TMPs, as illustrated in Figure 5.3. The differences in the nitrogen exhaustion performances may have changed the inelastic collision

in the plasma volume and the distribution of the high-energy electron so as to curtail the EEDF. Note that the molecular nitrogen had a 10 eV threshold energy for dissociation and a 15.6 eV energy for ionization [41]. As shown in Fig. 5.5, the information about the difference of exhaustion properties between the residual nitrogen in etcher<sub>new</sub> and that in etcher<sub>old</sub> may have been involved in the depletion of the EEDF tail. The partial pressures of the atomic nitrogen dissociated as a result of inelastic collisions with the high-energy electrons are compared in Fig. 5.6. Note that the RGA intensity ratio of the nitrogen atoms to the argon atoms was 8% higher in etcher<sub>new</sub> than in etcher<sub>old</sub>. These results suggested that the differences between the N<sub>2</sub> exhaustion performances of the TMPs due to the aging effects caused subtle changes in the residual gas partial pressure, resulting in gas mixing ratio fluctuation due to changes in the thermal equilibrium state of the chromium etching plasma.

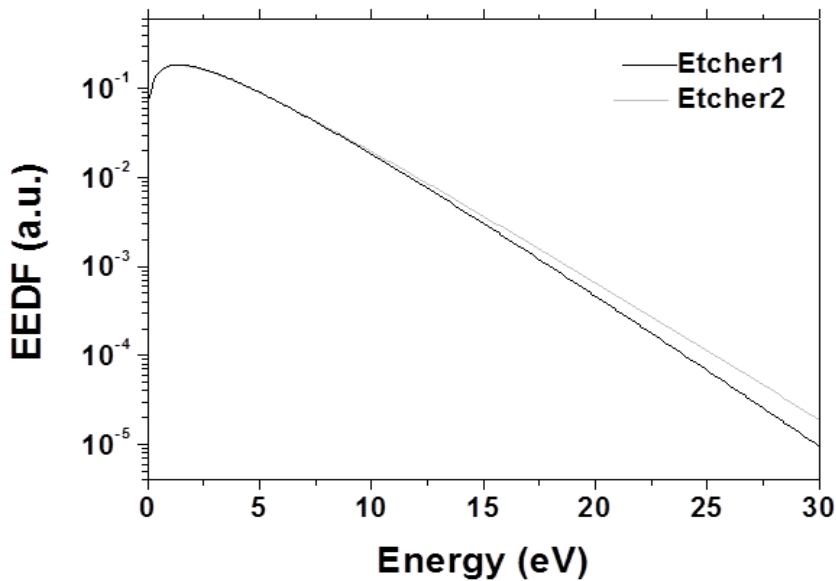


**Figure 5.5** EEDFs of the two etchers during the etching process, obtained from  $(b, T_{e,eff})$ , measured by using the OES signals. The values of  $(b, T_{e,eff})$  from the EEDFs plotted here were averaged over the values obtained during the 3 days from each etcher.

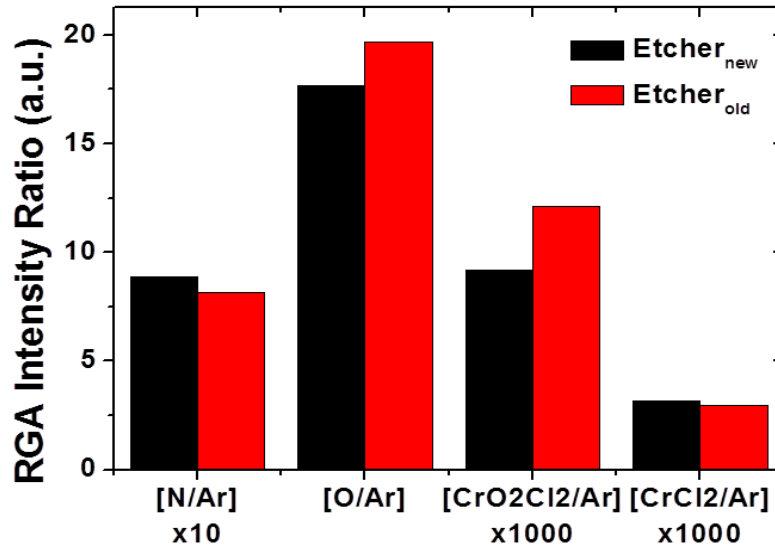
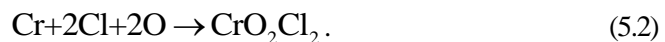


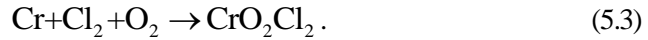
Figure 5.6 RGA intensity ratio of the dissociated nitrogen, oxygen radicals, CrO<sub>2</sub>Cl<sub>2</sub> species, and CrCl<sub>2</sub> species, normalized by the argon intensity in the two etchers, as measured during the etching process. The plotted intensity ratios were obtained from the average of the signals obtained over 3 days from each etcher.

The difference between the main PI parameter  $b$  of the two chromium etchers could be used to predict the variations in the reactive species generation rates. The contributions of the  $b$ -factor to the radical generation processes were estimated by assuming that the dominant etching chromium mechanism followed the reaction sequence shown in Eq. 5.2. According to the model of Nakata *et al.*, the overall chromium layer etching reaction by Cl<sub>2</sub> and O<sub>2</sub> - containing plasma was [16]



Wu *et al.* suggested that the first etch reactions were elementary reactions, yielding the

following overall etching reaction [122-123],



Eq. 5.3 indicated that the reactants and product were stable gases, and all volatile products could be pumped out of the chamber. Molecular oxygen and chlorine have very low adhesion to chromium metal surfaces, especially at low pressures (such as 3 mTorr, in this study). The low adhesion suggested a very low surface reaction rate, consistent with the presence of stable gas molecules. Eq. 5.2 was used in this dissertation and indicated that both the Cl and O radicals were required to generate the  $\text{CrO}_2\text{Cl}_2$  product. The  $\text{CrO}_2\text{Cl}_2$  constituted a volatile material in the chromium etching plasma with a boiling temperature of 117 °C under one atmosphere. The boiling point dropped to -18.4°C at 1 Torr. Because the surface temperature of the chromium film on the wafer exceeded the boiling temperature during the process [121,124], the etching product was very actively volatilized, and the byproduct could potentially alter the EEDF.

In the absence of a sufficient supply of the oxygen radicals to the chromium surface,  $\text{CrCl}_n$  ( $n=1 - 3$ ) compounds formed easily and remained on the surface because their melting points were high, around 1152 °C for  $\text{CrCl}_3$  [122-124]. By contrast, in the absence of the chlorine radical flux,  $\text{Cr}_2\text{O}_3$  and  $\text{CrO}$  compounds were generated, and their melting points exceeded 1000 °C [123]. These compounds were not volatile, and their presence reduced the etching reactions on the chromium surface. This mechanism suggested that the appropriate supply of both O and Cl radicals to the chromium surface was essential for sustaining the high etch rates.

The surface reactions of the Cr etching process are influenced by the radical densities, which are governed by the reactions that generate reactive radicals in the plasma volume as well as the radical flux into the plasma-chromium interface. The differences in the b-factor, as

shown in Fig. 5.4, resulted from differences in the N2 inelastic collision reaction rates based on the exhaustion properties. The differences between the EEDF areas in the two etchers at the tail were very small,  $10^{-4}$ , compared to the total area, 1; however, this difference corresponded to a 10% variation in the high-energy tail ( $> 13$  eV), which had an area of  $\sim 10^{-3}$ . Thus, the fraction of high-energy electrons varied by tens of % and caused a respectable variation in the reactive radical generation rate according to the Eq. 3.42 which is the main body of the PI-VM.

The variations in the O and Cl radical generation rates due to the gas mixing ratio variations could be calculated according to Eq. 3.43 as a case of Cl2/O2 based plasma reactions, which are the chemical etch contributing terms in the PI-VM model using the b-factor. The threshold energies needed to generate oxygen radicals and atomic oxygen ions were 8 eV and 12.2 eV, respectively [41]. The etcher<sub>new</sub> oxygen radical generation rate constant,  $R_O/n_e = 1.298 \times 10^{-7} \text{ cm}^3/\text{s}$ , was estimated using Eq. 3.43 with  $b = 1.04$  for  $f(\epsilon)$ . The rate constant for etcher<sub>old</sub>, with  $b = 1.00$ , was  $R_O/n_e = 1.479 \times 10^{-7} \text{ cm}^3/\text{s}$ . Note that the oxygen radical generation rate as the chemical etch contributing term into the PI-VM decreased by 14% for the new TMP-equipped etcher. On the other hand, the threshold energies needed to generate chlorine radicals via dissociation and dissociative attachment were 3 eV and 0.05 eV, respectively [41]. The chlorine radical generation rate constants for etcher<sub>new</sub> and etcher<sub>old</sub> were calculated according to  $R_{Cl}/n_e = 6.851 \times 10^{-7} \text{ cm}^3/\text{s}$  and  $7.111 \times 10^{-7} \text{ cm}^3/\text{s}$ ; thus, they showed a 4% difference. The high threshold energies of the oxygen radicals rendered  $R_O/n_e$  more sensitive to the PI parameter  $b$  than  $R_{Cl}/n_e$ . As a result, the oxygen radical flux in etcher<sub>new</sub> onto the target chromium decreased by 14% whereas the chlorine radical flux was only 4% less than that of etcher<sub>old</sub>. These effects produced fewer oxygen radicals and generated less  $\text{CrO}_2\text{Cl}_2$  in etcher<sub>new</sub> than in etcher<sub>old</sub>. The rates at which the non-volatile  $\text{CrCl}_2$  or  $\text{CrCl}_3$  were generated by the chlorine radicals increased in etcher<sub>new</sub>, and these non-volatile products occupied 2 or 3 sites of the Cr surface [125]. The effective etching target surface area in etcher<sub>new</sub> was smaller than that

in etcher<sub>old</sub>; thus, this difference in the surface reaction property of two etchers is accounted into the  $C_j$  of the Eq. 3.43, and resulted in the about 30 % difference of overall  $r_{\text{etch}}$ -factor described in the Eq. 3.42.

The measured RGA intensity ratios of the O radical,  $\text{CrO}_2\text{Cl}_2$ , and  $\text{CrCl}_2$  products in the two etchers during the etching processes are shown in Figure 5.6. The relative partial pressures of the three-species were compared in the etchers, based on the mass spectral intensities of each product, normalized by the intensity of Ar, which remained constant. The partial pressure of O radicals was 11.2% higher in etcher<sub>old</sub> than in etcher<sub>new</sub>. This result reflected the calculated oxygen dissociation rate differences according to Eq. 5.2. The partial pressure of  $\text{CrO}_2\text{Cl}_2$  in etcher<sub>old</sub>, which corresponded to the etch rate, was 131.5 % the value in etcher<sub>new</sub>, whereas the partial pressure of the species remaining on the surface,  $\text{CrCl}_2$ , was 94 % of the value measured in etcher<sub>new</sub>, as expected based on the rate constant analysis.

The etching results were obtained from triplicate experiments conducted on different days. Note that the error bars of the etch rates indicate the standard deviations from the one day etch rates collected from 7 of the wafers etched in each of the etchers. The average etch rates were  $6.8 \pm 0.2$  nm/min for etcher<sub>new</sub> and  $9.9 \pm 1.3$  nm/min for etcher<sub>old</sub>, respectively, indicating that the etch rates varied by approximately 30%. These deviations agreed well with the PI-VM results and differences in the  $\text{CrO}_2\text{Cl}_2$  partial pressures in the two etchers, which were measured based on the RGA. The variations in the residual N<sub>2</sub> exhaustion performance due to the TMP aging effects resulted in a 30% variation in the Cr etch rates and corresponded to the b-factor variation in the O radical generation rates.

The age of a vacuum pump generally does not influence the etching process, and any such effects would be difficult to detect prior to the pump breaking down; however, the age of the pump can introduce important of deviations in etching process results. The different performances of pumps of different age can induce subtle variations in the N<sub>2</sub>/O<sub>2</sub> residual gas

composition in the etch reactors, and the Cr etching plasma properties, as indicated by the PI parameter  $b$  and PI-VM results, can differ. The vacuum pump age produced 30% variations in the Cr etch rate in this experiment, and the effects of the curtailed EEDF tail as a result of inelastic collisions with different amounts of residual nitrogen gas were quantitatively analyzed in terms of the PI-VM consisting chemical reaction and surface terms.

This dissertation revealed that PI-VM based plasma process device analysis could be applied to the detection of minute changes in the discharge conditions, and the cause analysis of the chamber-to-chamber (C2C) matching problems that frequently occurred in industry. In this case, vacuum pump aging effect is analyzed as a cause of C2C problem, and the type of process fault can be classified. This characteristic of PI-VM which includes information about the reaction mechanism efficiently by the adoption of PI parameters is expected to provide the basis of FDC and APC, and would contribute to the advances of the plasma-assisted processes.

## Chapter 6 . Conclusion

Through the application of plasma information (PI) parameters as the core variables to virtual metrology (VM) for plasma-assisted processes, enhancement of VM performance can be possible compared to the VM models based on the existing statistical technique. According to the reaction mechanisms in the process reactor, information about the plasma property should be considered efficiently to develop the VM. The dominant contribution of PI parameters to PI-VM performance was validated from cumulated variance analysis; the strong correlation between the process results and condition of the process device, which determines the properties of the plasma, is understood.

On account of the specificity of the reactions in the plasma reactor, three types of reactions in the plasma volume, sheath, and surface contribute to the process results with different mechanisms. To efficiently include the information about these reactions into the VM model, PI parameters  $b$  and  $q$ , as well as passivation species signals, are introduced as the variables. Each PI parameter represents the reaction rate governing the physical parameters of the EEDF shape, ion bombarding energy, and surface passivating species flux in the volume, sheath, and substrate surface in the plasma, respectively. Adoption of the PI parameters to the VM development enables the algorithm to efficiently contain good information for the performance variable prediction. In addition, it implies that the cause of the process result deviation is the variation of the process plasma properties according to the process device condition. This PI-VM property enables the fault detection and classification (FDC) of the process results by backtracking of the PI-VM reaction mechanisms. This suggests that the

adoption of PI parameters can become an efficient method of including information about the process plasma reaction mechanism, as well as of the performance variables of the process, into the algorithms for advanced process control (APC). Moreover, PI-VM can be applied as a basic framework of a process control-based methodology for plasma-assisted processes.

## Bibliography

1. G. E. Moore, *Electronics* **38** (1965) 114.
2. H. Abe, M. Yoneda, and N. Fujiwara, *Jpn. J. Appl. Phys.*, **47** (2008) 1435-1455.
3. S. Samukawa, M. Hori, S. Rauf, K. Tachibana, P. Bruggeman, G. Kroesen, J. C. Whitehead, A. B. Murphy, A. F. Gutsol, S. Starikovskaia, U. Kortshagen, J. -P. Boeuf, T. J. Sommerer, M. J. Kushner, U. Czarnetzki, and N. Mason, *J. Phys. D: Appl. Phys.* **45** (2012) 253001.
4. S. -H. Lee, J. -H. Cho, S. -R. Huh, and G.-H. Kim, *J. Phys. D : Appl. Phys.* **47** (2014) 015205.
5. W. -K. Loh, J. -Y. Yun, *Cluster Comput* **17** (2014) 643-651.
6. C. J. Spanos, H. -F. Guo, A. Miller, and J. Levine-Parrill, *IEEE Trans. Semiconductor Manufacturing* **5** (1992) 4.
7. F. T. Cheng, H. -C. Huang, and C. -A. Kao, *IEEE Trans. Automation Science and Engineering* **9** (2012) 1.
8. H. D. Lee, M. H. Lee, H. W. Cho, C. Han, and K. S. Chang, *Hwahak Konghak* **35** (1997) 5.
9. S. J. van Albada, P. A. Robinson, *Journal of Neuroscience Methods* **161** (2007) 205–211.
10. A. T-C. Koh, N. F. THornhill, and V. J. Law, *Electronics Letters* **35** (1999) 1383-1385.
11. D. A. White, D. Boning, S. W. Butler, and G. G. Barna, *IEEE Trans. Semiconductor Manufacturing* **10** (1997) 52-61.

12. B. Schölkopf, A. Smola, K. -R. Müller, [Lecture Notes in Computer Science 1327](#) (1997) 583-588.
13. R. Shadmehr, D. Angell, P. B. Chou, G. S. Oehrlein, and R. S. Joffe, *J. Electrochem. Soc.* **139** (1992) 3.
14. T.-H. Lin, *IEEE Trans. Semiconductor Manufacturing* **22** (2009) 1.
15. M. A. Lienermann and A. J. Lichtenberg, *Principles of Plasma Discharges and Materials Processing*, 2nd ed. (John Wiley & Sons., New York, 2005).
16. T. I. Gombosi, *Gaskinetic theory* (Cambridge University Press, New York, 1994).
17. S. Park, J. -M. Choe, H. -J Roh, and G. -H. Kim, *J. Kor. Phys. Soc.* **64** (2014) 1819-1827.
18. U Fantz, *Plasma Sources Sci. Technol.* **15** (2006) S137–S147.
19. V. A. Godyak, R. B. Piejak, and B. M. Alexandrovich, *J. Appl. Phys.* **73** (a), (2003) 15.
20. V. A. Godyak, *IEEE Trans. Plasma Science* **34** (2006) 3.
21. V. A. Godyak and R. B. Piejak, *Appl. Phys. Lett.* 63 (1993) 23.
22. A. Kono, *J. Phys. D: Appl. Phys.* **32** (1999) 1357–1363.
23. K. -U. Riemann, *J. Phys. D: Appl. Phys.* **24** (1991) 492-518.
24. M. A. Lieberman, C. Charles, and R. W. Boswell, *J. Phys. D: Appl. Phys.* **39** (2006) 3294–3304.
25. M. Yan, A. Bogaerts, W. J. Goedheer, and R. Gijbels, *Plasma Sources Sci. Technol.* **9** (2000) 583–591.
26. I. T. Martin, and E. R. Fisher, *J. Vac. Sci. Technol. A* **22** (2004) 2168.
27. X. Li, X. Hua, L. Ling, and G. S. Oehrlein, *J. Vac. Sci. Technol. A* **20** (2002) 6.
28. V. Krastev, I. Reid, C. Galassi, G. Hughes, E. McGlynn, *J. Materials Science : Materials in Electronics* **16** (2005) 541-547.

29. V. A. Godyak, R. B. Piejak, and B. M. Alexandrovich, *Plasma Sources Sci. Technol.* **4** (1995) 332436.
30. V. A. Godyak, *Plasma Sources Sci. Technol.* **20** (2011) 025004.
31. V. A. Godyak, R. B. Piejak, and B. M. Aexanrovich, *Plasma Sources Sci. Technol.* **1** (1992) 36.
32. V. A. Godyak, R. B. Piejak, and B. M. Alexandrovich, *Plasma Sources Sci. Technol.* **A 20** (2002) 555.
33. J. B. Boffard, R. O. Jung, C. C. Lin, L. E. Aneskavichand, A. E. Wendt, *Plasma Sources Sci. Technol.* **20** (2011) 055006.
34. F. M. Dias, and T. K. Popov, *J. Phys.: Conference Series* **44** (2006) 202.
35. J. T. Gudmundsson, *Plasma Sources Sci. Technol.* **10** (2001) 76.
36. F. A. Haas, *Plasma Sources Sci. Technol.* **7** (1998) 471.
37. K. Behringer, and U. Fantz, *Contrib. Plasma Phys.* **39** (1999) 5.
38. J. P. Santos, F. Parente, and Y. K. Kim, *J. Phys. B : At.Mol. Opt. Phys.* **36** (2003) 4211.
39. Y. K. Kim, and M. Eugene Rudd, *Phys. Rev.* **A 50** (1994) 5.
40. NIST database, <http://physics.nist.gov/PhysRefData/>.
41. KISTI plasma property database, <http://plasma.kisti.re.kr/>.
42. X. M. Zhu, and Y. K. Pu, *Phys. Plasmas* **13** (2006) 063507.
43. X. M. Zhu, Y. K. Pu, Y. Celik, S. Siepa, E. Schungel, D. Luggenholscher, and U. Czarnetzki, *Plasma Sources Sci. Technol.* **21** (2012) 024003.
44. J. B. Boffard, R. O. Jung, C. C. Lin, L. E. Aneskavich, and A. E. Wendt, *J. Phys. D: Appl. Phys.* **45** (2012) 045201.
45. M. A. Lieberman, and S. Ashidaz, *Plasma Sources Sci. Technol.* **5** (1996) 145–158.
46. S. Rauf, and M. J. Kushner *J. Appl. Phys.* **82** (1997) 6.

47. J. Hopwood, *Plasma Sources Sci. Technol.* **3** (1994) 460.
48. D. -W. Hu, and Y. -K. Pu, *J. Phys. D: Appl. Phys.* **42** (2009) 115203
49. J. -M. Choe, G. -H. Kim, and D. -G. Kim, *J. Kor. Phys. Soc.* **55** (2009) 5.
50. M. J. Druyvesteyn, *J. Phys.* **64** (1930) 781.
51. J. T. Gudmundsson, A. M. Marakhtanov, K. K. Patel, V. P. Gopinath, and M. A. Liebermann, *J. Phys. D: Appl. Phys.* **33** (2000) 1323.
52. M. Ishimaru, T. Ohba, T. Ohmori, T. Yagisawa, T. Kitajima and T. Makabe, *Appl. Phys. Lett.* **92** (2008) 071501.
53. Y. M. Aliev, I. D. Kaganovich, and H. Schluter, *Phys. Plasma* **4** (1997) 7.
54. Y. M. Aliev, I. D. Kaganovich, and H. Schluter, *Electron Kinetics and Application of Glow Discharges* (Plenum Press, New York, 2005).
55. T. Kimura, and K. Ohe, *J. Appl. Phys.* 89 (2001) 8.
56. D. P. Lymberopoulos, and D. J. Economou, *J. Appl. Phys.* **73** (1993) 3668.
57. T. Sato, and T. Makabe, *J. Phys. D : Appl. Phys.* **41** (2008) 035211.
58. Y. Hayashi, S. Hirao, Y. Zhang, T. Gans, D. O'Connell, Z. Lj. Petrovic, and T. Makabe, *J. Phys. D : Appl. Phys.* **42** (2009) 145026.
59. D. D. Monahan, and M. M. Turner, *Plasma Sources Sci. Technol.* **17** (2008) 045003.
60. J. T. Gudmundsson, T. Kimura, and M. A. Liebermann, *Plasma Sources Sci. Technol.* **8** (1999) 22-30.
61. J. T. Gudmundsson, and E. G. Thorsteinsson, *Plasma Sources Sci. Technol.* **16** (2007) 399-412.
62. D. P. Lymberopoulos, and D. J. Economou, *J. Appl. Phys.* **73** (1993) 3668.
63. X. Yuan, and L. L. Raja, *IEEE Trans. Plasma Sci.* **31** (2003) 4.
64. D. Lee, J. M. Park, S. H. Hong, and Y. Kim, *IEEE Trans. Plasma Sci.* **33** (2005) 2.

65. K. H. Baek, T. F. Edgar, K. Song, G. Choi, H. K. Cho, C. Han, *Comp. Chem. Eng.* **61** (2014) 20-29.
66. S. Jeong, *Development of Operating Power Dependent Etch Process Control in Triple Frequency Driven Capacitively Coupled Plasma Source* (M.S. Thesis, Seoul National University, Seoul, 2014).
67. H. M. Anderson, J. A. Merson, and R. W. Light, *IEEE Trans. Plasma Sci.* **PS-14** (1986) 2.
68. C. P. D'Emic, K. K. Chan, and J. Blum, *J. Vac. Sci. Technol. B* **10** (1992) 1105.
69. L. E. Kline, *IEEE Trans. Plasma Sci.* **PS-14** (1986) 2.
70. K. R. Ryan, and I. C. Plumb, *Plasma Chem. Plasma Proc.* **10** (1990) 2.
71. O. Joubert, G. S. Oehrlein, M. Surendra, *J. Vac. Sci. Technol. A* **12** (1994) 3.
72. I. W. Rangelow, *J. Vac. Sci. Technol. A* **21** (2003) 4.
73. D. Zhang, and M. J. Kushner, *J. Vac. Sci. Technol. A* **19** (2001) 2.
74. S. Rauf, and M. J. Kushner, *J. Appl. Phys.* **82** (1997) 2805.
75. A. V. Vasenkov, X. Li, G. S. Oehrlein, and M. J. Kushner, *J. Vac. Sci. Technol. A* **22** (2004) 511.
76. H. H. Doh, J. H. Kim, S. H. Lee, and K. W. Whang, *J. Vac. Sci. Technol. A* **14** (1996) 2827.
77. X. Li, X. Hua, L. Ling, and G. S. Oehrlein, M. Barela, and H. M. Anderson, *J. Vac. Sci. Technol. A* **20** (2002) 6.
78. P. Ho, J. E. Johannes, R. J. Buss, and E. Meeks, *J. Vac. Sci. Technol. A* **19** (2001) 2344.
79. G. I. Font, W. L. Morgan, and G. Mennenga, *J. Appl. Phys.* **91** (2002) 3530.
80. H. Amemiya, *J. Phys. Soc. Jap.* **67** (1998) 6.

81. D. Bohm, *The Characteristics of Electrical Discharge in Magnetic Fields*, ed. A. Guthrie and R. K. Wakerling (Mc-Graw Hill, New York, London, 1949).
82. J. T. Gudmundsson, *Plasma Sources Sci. Technol.* **10** (2001) 76-81.
83. J. E. Allen, *Plasma Sources Sci. Technol.* **13** (2004) 48-49.
84. N. St. J. Braithwaitet, and J. E. Allen, *J. Phys. D: Appl. Phys.* **21** (1988) 1733-1737.
85. T. E. Sheridan, P. Chabert, and R. W. Boswell, *Plasma Sources Sci. Technol.* **8** (1999) 457-462.
86. A. Kono, *J. Phys. D: Appl. Phys.* **32** (1999) 1357-1363.
87. J. I. F. Palop, J. Ballesteros, M. A. Hernández, and R. M. Crespo, *J. Appl. Phys.* **91** (2002) 2587. 88. J. I. F. Palop, J. Ballesteros, M. A. Hernández, R. M. Crespo, and S. B. del Pino, *J. Phys. D: Appl. Phys.* **38** (2005) 868-871.
88. J. -L. Brisset, D. Moussa, A. Doubla, E. Hnatiuc, B. Hnatiuc, G. K. Youbi, J. -M. Herry, M. Naitali, and M. -N. B. Fontaine, *Ind. Eng. Chem. Res.* **47** (2008) 16.
89. F. Perrot, M. W. C. Dharma-wardana, *Phys. Rev.* **30** (1984) 5.
90. G. Hummer, L. R. Pratt, A. E. Garcia, *J. Phys. Chem.* **100** (1996) 1206-1215.
91. X. Chen, and P. Han, *J. Phys. D: Appl. Phys.* **32** (1999) 1711-1718.
92. R. L. Dewarl, M. J. Hole, M. McGann, R. Mills, and S. R. Hudson, *Entropy* **10** (2008) 621-634.
93. C. G. Chakrabarti, and K. De, *Internat. J. Math. & Math. Sci.* **23** (2000) 4.
94. H. -P. Hsueh, R. T. McGrath, B. Ji, B. S. Felker, J. G. Langan, and E. J. Karwacki, *J. Vac. Sci. Technol. B* **19** (2001) 4.
95. J. Robertson, *J. Appl. Phys.* **87** (2000) 5.
96. M. J. Kushner, *J. Appl. Phys.* **63** (1988) 8.
97. M. J. Kushner, *J. Appl. Phys.* **62** (1987) 2803.

98. T. Tatsumi, H. Hayashi, S. Morishita, S. Noda, M. Okigawa, N. Itabashi, Y. Hikosaka, M. Inoue, *Jpn. J. Appl. Phys.* **37** (1998) 2394-2399.
99. A. Matsuda, *Thin Sol. Films* **92** (1982) 171-187.
100. A. Matsuda, *Jpn. J. Appl. Phys.* **25** (1986) 12.
101. M. P. Hong, J. H. Seo, W.J. Lee, S. G. Rho, W. S. Hong, T. Y. Choi, H. I. Jeon, S. I. Kim, B. S. Kim, Y. U. Lee, J. H. Oh, J. H. Cho, and K. Chung, *SID Symposium Digest of Technical Papers* **36** (2005) 14–17.
102. D. L. Smith, A. S. Alimonda, C. -C. Chen, S. E. Ready, and B. Wacker, *J. Electrochem. Soc.* **137** (1990) 2.
103. U. K. Das, P. Chaudhuri, *Chem. Phys. Lett.* **298** (1998) 211–216.
104. P. P. Potzinger, and F. W. Lampe, *J. Phys. Chem.* **73** (1969) 11.
105. M. Kondo, and A. Matsuda, *Curr. Opin. Solid State Mater. Sci.* **6** (2002) 445-453.
106. A. Matsuda, *J. Non-Cryst. Solids* **338** (2004) 1-12.
107. A. Matsuda, *J. Non-Cryst. Solids* **59&60** (1983) 767-774.
108. A. Matsuda, C. C. Tsai, G. B. Anderson, R. Thompson, B. Wacker, *J. Non-Cryst. Solids* **114** (1989) 151.
109. A. Matsuda, K. Nakamura, K. Yoshida, S. Takeoka, I. Shimizu, *Jpn. J. Appl. Phys.* **34** (1995) 442.
110. S. H. Kim, S. W. Na, N. E. Lee, Y. W. Nam, and Y. H. Kim, *Surface Coatings Technol.* **200** (2005) 2072-2079.
111. O. Olubuyide, D. T. Danielson, L. C. Kimerling, and J. L. Hoyt, *Thin Sol. Films* **508** (2006) 14-19.
112. M. Heintze, R. Zedlitz, and G. H. Bauer, *J. Phys. D : Appl. Phys.* **26** (1993) 1781-1786.

113. J. -H. Zhou, K. Ikuta, T. Yasuda, T. Umeda, S. Yamasaki, K. Tanaka, *J. Non-Cryst. Solids* **227-230** (1998) 857-860.
114. M. Fukasawa, A. Kawashima, N. Kuboi, H. Takagi, Y. Tanaka, H. Sakayori, K. Oshima, K. Nagahta, and T. Tatsumi *Jpn. J. Appl. Phys.* **48** (2009) 08HC01.
115. T. Ichiki, S. Takayangi, and Y. Horiike, *J. Electrochem. Soc.* **147** (2000) 11.
116. P. Duval, A. Raynaud, and C. Saulgeot, *J. Vac. Sci. Technol. A* **6** (1988) 3.
117. J. Henning, *Vacuum* **21** (1971) 11.
118. T. A. Heppell, *Vacuum* **37** (1987) 8.
119. K. H. Baek, Y. Jung, G. J. Min, C. Kang, H. K. Cho, and J. T. Moon, *J. Vac. Sci. Technol. B* **23** (2005) 1.
120. H. Nakata, K. Nishioka, and H. Abe, *J. Vac. Sci. Technol.* **17** (1980) 6.
121. B. Wu, *J. Vac. Sci. Technol. B* **22** (2004) 3.
122. B Wu, *J. Vac. Sci. Technol. B* **24** (2006) 1.
123. K. -H. Kwon, S. -Y. Kang, S. -H. Park, H. -K. Sung, D. -K. Kim, and J. -H. Moon, *J. Matt. Sci. Lett.*, **18** (1999) 1197.
124. H. Abe, M. Yoneda, and N. Fujiwara, *Jpn. J. Appl. Phys.* **47** (2008) 3.

## 초 록

반도체 및 디스플레이 제조 공정에 활용되는 플라즈마 공정의 관리 및 수율 향상을 위해서는 가상 계측(VM)을 통한 공정 모니터링이 필수적이다. 식각률 및 박막 증착률 등의 예측에 활용되는 가상 계측 모델은 일반적으로 계측 변수와 결과 변수 간의 관계 분석을 위한 통계적 방법을 기반으로 한다. 주성분 분석법(PCA)은 가상 계측 모델 개발에 흔히 이용되는 통계 방법론이다. 주성분 분석법은 계측 변수와 결과 변수의 상관도를 분석하고 이에 따라 공정 결과의 예측에 활용 가능하도록 계측 변수들을 조합하여 상호 독립적인 주성분들(PCs)을 구성하는 방법이다. 그러나 주성분 분석법에 활용되는 계측 인자들은 장치 계측 시스템(EES)과 I-V 신호, 임피던스 신호, 광신호의 원형 등의 센서 데이터들로서, 실제 공정 반응기 내의 플라즈마 반응에 관한 정보를 효율적으로 담고 있지 못하다. 소위 말하는 공정의 상태에 대한 정보를 효율적으로 담고 있는 ‘좋은’ 인자를 획득하여 가상 계측 모델에 적용하는 것은 모델의 정확도 확보 측면에서 중요하다. 따라서 공정 플라즈마에 대한 정보를 충분히 담고 있지 못한 경우 통계 기반 방법론에 기반한 가상 계측 모델의 성능은 초미세 공정을 진행 중인 산업계의 정확도 요구 조건을 충족하기 어렵다.

플라즈마 공정 장치 내에는 플라즈마의 주 공간과 쉬스(sheath), 반응체 표면에서 일어나는 서로 다른 메커니즘을 갖는 3 종류의 반응이 존재한다. 플라즈마의 주 공간에서는 전자의 비탄성 충돌 반응을 통해 활성종이나 이온종의 생성이 주로 일어난다. 이러한 반응의 반응률은 저밀도, 저온 인 공정 플라즈마 내에서는 주로 전자 에너지 분포 함수(EEDF)로 표현 가능한 플라즈마의 열평형 상태에 의하여 결정된다. 쉬스 영역에서는 공간에서 생성된 높은 반응성을 가진 입

자들과 에너지의 전달이 일어난다. 이온종은 쉬스의 전기장에 의하여 가속되며 반응체 표면으로 가속을 통해 얻은 에너지를 전달한다. 쉬스 전기장의 세기는 해당 플라즈마의 전기 음성도와 전자 에너지 분포에 의해 결정이 된다. 반응체 표면에서는 쉬스를 통해 전달된 입자들의 흡착 및 가장 안정적인 격자 위치를 향한 표면 확산이 발생하며 이를 통해 플라즈마를 통해 전달된 물질과 고체 표면의 반응이 일어난다. 이러한 표면 반응률은 반응체 물질의 활성화 에너지와 고체의 표면 온도에 의하여 결정된다. 이와 같은 공정 플라즈마 내에서 발생하는 3 종류 반응은 최종 공정 반응률을 결정하게 된다. 따라서, 플라즈마 공정의 경우 이와 같은 반응들에 대한 정보를 효율적으로 포함한 변수를 활용해야 고성능 가상 계측 방법의 개발이 가능하다.

본 연구에서는 ‘좋은’ 정보를 담은 가상 계측 방법론의 핵심 인자를 얻기 위해 플라즈마의 공간, 쉬스, 표면 반응 특성을 나타내는 플라즈마 정보(PI) 인자들의 개발이 수행되었다. 공간 반응을 모니터링 하기 위한 변수로는 전자 에너지 분포 함수의 모양 인자  $b$ 가, 전기 음성도를 갖는 대부분의 공정 플라즈마의 쉬스 특성을 모니터링 하기 위한 변수로는 이온 에너지를 나타내는  $q$  인자가, 그리고 반응체 표면 반응 특성을 모니터링 하기 위한 변수로는 피막 반응 형성 기여종의 신호가 플라즈마 정보 인자로 제시 되었다. 이와 같은 플라즈마 정보 인자들은 종점 계측(EPD) 등을 통해 기 장착되어 활용도가 높고 장치 바깥에 위치하여 플라즈마에 영향을 주지 않아 실용적인 센서인 광진단계(OES)를 통해 측정되었다.

개발된 플라즈마 정보 인자들은 플라즈마의 공간, 쉬스, 표면 반응률 결정 메커니즘에 준하여 총 반응률에 준하는  $r$  인자를 구성하도록 조합되어 가상 계측 모델로써 적용되었다. 이와 같이 개발된 플라즈마 정보 기반 가상 계측 모델은 PI-VM으로 명명하였다. PI-VM은  $C_4F_8$  기반의 산화 실리콘 식각 반응률 예측과 a-Si 박막 증착 반응률 예측에 대하여 90 % 이상의 상관 계수를 확보함으로

써 해당 공정에 대하여 기존의 통계 기반 방법론을 통해 얻을 수 있었던 정확도 ( $R^2 \sim 50\%$ ) 대비 크게 향상된 성능을 보였다. 이는 산업체의 요구 조건을 만족하는 정확도이다.

주성분들의 누적 분산 분석을 통해 기존의 통계 기반 가상 계측 방법론 대비 PI-VM의 성능 향상은 플라즈마 정보 인자의 포함 효과가 지배적임을 검증할 수 있었다. 또한 이와 같은 분석을 통하여 플라즈마 공정 결과의 이격 발생과 이를 유발하는 플라즈마의 특성 변동 및 공정 장치의 특성 변동 간의 상관성에 대한 평가가 가능하였다. 따라서 공정 이격 및 실패 발생 시 원인 분석 알고리즘의 기반기술로써 PI-VM이 활용 가능함을 보였다. 이는 공정 실패 진단(FDC) 및 공정 제어(APC) 알고리즘 등의 플라즈마 공정 진단 기술 개발은 플라즈마 정보 인자가 기반 인자로서 활용됨으로써 가능할 것임을 보이는 결과이다.

**주요어** : 플라즈마 정보 기반 가상 계측 방법론 (PI-VM), 전자 에너지 분포 함수 (EEDF), b-인자, q-인자, 식각, 증착

**학번** : 2008-21137